INSTRUMENTAL ASPECTS OF HIGH-FIELD FORCE-DETECTED ELECTRON SPIN RESONANCE

Paul Alexander Sawchuk Cruickshank

A Thesis Submitted for the Degree of PhD
at the
University of St Andrews

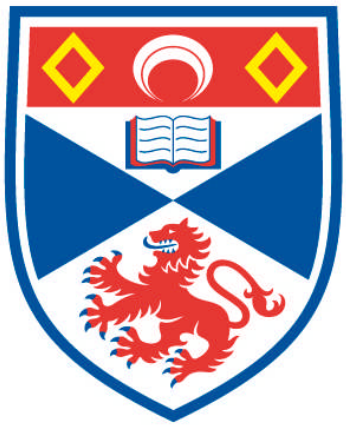

2003

Instrumental Aspects of High-Field Force-Detected Electron Spin Resonance

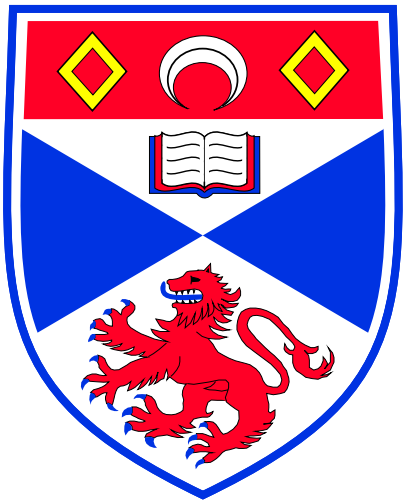

A thesis presented by
Paul Alexander Sawchuk Cruickshank
to the
University of St Andrews
in application for the degree of
Doctor of Philosophy

October 2003

Declarations

I, Paul Alexander Sawchuk Cruickshank, hereby certify that this thesis, which is approximately 35,000 words in length, has been written by me, that it is the record of work carried out by me, and that it has not been submitted in any previous application for a higher degree.

date _____ *signature of candidate* _____

I was admitted as a research student in September 1999 and as a candidate for the degree of Doctor of Philosophy in September 2000; the higher study for which this is a record was carried out in the University of St Andrews between 1999 and 2003.

date _____ *signature of candidate* _____

I hereby certify that the candidate has fulfilled the conditions of the Resolution and Regulations appropriate for the degree of Doctor of Philosophy in the University of St Andrews and that the candidate is qualified to submit this thesis in application for that degree.

date _____ *signature of supervisor* _____

In submitting this thesis to the University of St Andrews I understand that I am giving permission for it to be made available for use in accordance with the regulations of the University Library for the time being in force, subject to any copyright vested in the work not being affected thereby. I also understand that the title and abstract will be published, and that a copy of the work may be made and supplied to any *bona fide* library or research worker.

date _____ *signature of candidate* _____

Acknowledgements

Firstly I would like to thank my supervisor Graham Smith for his invaluable, helpful, enthusiastic and (very!) patient guidance over the last four years. It may be his fault that I haven't seen natural light for that time, but it'd have been much worse without his help.

I'd also like to thank Duncan Robertson for all his help with all aspects of mm-wave physics and Peter Riedi for teaching me the heady delights of magnetic resonance. Dav Macfarlane and Greg Johnson helped me navigate the treacherous waters of programming and Nigel Poolton provided endless advice on experiments. Reg Gavine and Bob Mitchell helped to make the cryogenic requirements a lot less frightening than they could have been.

A special mention must be made of everyone in the departmental mechanical workshop, without whom this work would not be possible, especially George Radley, Paul Aitken and Dave Stevens.

Thanks also to many people for general encouragement, especially Pete, Kat, Melanie (I really should find out what a semicolon is...), Naiara, Hassane, Anjali, Catherine and Jude.

Finally, I would like to thank my parents for just about every variety of support possible. This thesis is theirs. It'll come in handy for propping doors open.....

Abstract

Magnetic resonance force microscopy (MRFM) is a new measurement technique combining scanning probe microscopy (SPM) and MR spectroscopy, offering the potential of high resolution chemical specific imaging. MRFM is based on the principle of force detection of magnetic resonance (FDMR) in which the magnetisation of a sample in a magnetic field is coupled to an atomic force microscopy cantilever via a field gradient. Magnetic resonance is used to modulate the sample magnetisation at the cantilever resonant frequency and the resulting oscillating force on the cantilever leads to oscillations which may be detected optically. The high sensitivity of force detection offers the potential for single electron spin sensitivity.

This thesis describes instrumental aspects of ESR based FDMR experiments and presents the first results at high fields (3.3T). High fields are advantageous for sensitivity and spectral resolution. However, they pose significant technical challenges.

FDMR measurements on the organic conductor (fluoranthene)2PF6 were carried out in experiments based around an existing quasi-optical high field ESR spectrometer. Further measurements on (FA)2PF6 and DPPH are presented together with progress towards the construction of a high field MRFM system, based on a commercial SPM instrument. Experiments were performed with both magnet-on-cantilever and sample-on-cantilever configurations with the former the favoured method for potential imaging applications. Signal detection uses a novel fibre-optic interferometer. Cantilever magnets of low conductivity ferrite appear to be more promising for high Q measurements than the metallic magnets favoured by most other groups.

Experiment sensitivities are estimated at around 4.4×10^8 polarised electron spins, comparable to conventional commercial ESR spectrometers. Experimental consistency was difficult, especially regarding the positioning of probe and sample, an area in which refinement is essential for repeatable and sensitive experiments. The potential for imaging is attractive and the prospect of single spin detection is discussed.

Contents

Chapter 1

Introduction to magnetic resonance force microscopy

Magnetic resonance force microscopy (MRFM) is a new measurement technique which combines magnetic resonance spectroscopy with high resolution scanning probe microscopy (SPM) techniques and offers the prospect of combining the chemical specificity of the former with the resolution of the latter. MRFM is based on the principle of force detected magnetic resonance (FDMR) which involves measuring the force due to the interaction of a magnetic field gradient with the magnetisation of a sample in a magnetic field using micro-cantilevers. Magnetic resonance is used to manipulate the sample magnetisation at the cantilever resonant frequency and detection of the resulting cantilever motion allows magnetic resonance to be measured, in principle with unparallelled sensitivity on a very local scale.

The last decade has seen FDMR and MRFM experiments based on nuclear magnetic resonance (NMR), electron spin resonance (ESR) and ferromagnetic resonance (FMR). Each "flavour" of FDMR/MRFM has its own applications but all are attractive as they offer the prospect of imaging the magnetic resonance of a system on a scale far smaller than that available through conventional magnetic resonance imaging (MRI). MRFM benefits from the widespread use of various SPM techniques and uses a great deal of SPM technology. In particular, it has much in common with atomic force microscopy (AFM), which measures the force on a micro-cantilever as it is scanned close to or just touching a surface and can yield atomic resolution images.

This thesis presents work done towards the construction of a high field magnetic res-

onance force microscope based on electron spin resonance at fields of 3 to 10 Tesla, corresponding to resonant frequencies of 90 to 270GHz. The goal is technically ambitious compared to similar experiments at lower frequencies but a high field approach to ESR based FDMR/MRFM is desirable for reasons relating to sensitivity and spectral resolution as will be discussed. This chapter will provide an account of the development of magnetic resonance force microscopy and a review of the field to date before a brief overview of the rest of the thesis. Although MRFM is a relatively young field, some of the core ideas behind the technique have changed significantly since its inception. The review will discuss developments in both NMR and ESR based MRFM, although there will be more emphasis on the ESR based work, in keeping with the themes of the thesis. Detection of electron spins by scanning tunnelling microscopy (STM) will also be mentioned as another possible method of single-spin sensitivity measurement.

1.1 Early history and development of MRFM

MRFM was first proposed in 1991 by Sidles [1] as a potential method for detecting a single proton spin without using inductive methods. His initial suggestion involved directly coupling the motion of a *mechanical* oscillator to the Larmor precession of a nuclear spin in a magnetic field and the proposed system is shown in figure 1.1. The nucleus of interest would be contained in an oscillating substrate and a magnetic source mounted on the mechanical oscillator would provide the necessary coupling between it and the proton in the substrate. The idea was that when there was resonance between the oscillator frequency, the substrate frequency and the proton precession frequency, energy would be transferred to the mechanical oscillator, whose motion could be measured, thus enabling detection of the spin. Sidles and colleagues followed his initial suggestion by discussing the feasability of single spin detection [2], analysing the system as a Stern-Gerlach experiment [3] and, along with Rugar at IBM, comparing theoretical sensitivities with those of induction detected magnetic resonance [4].

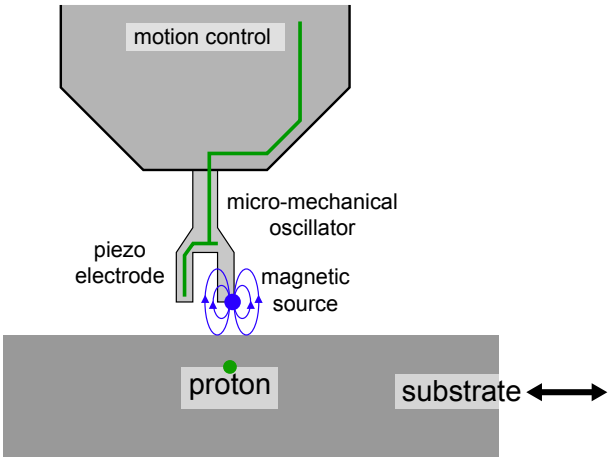

Figure 1.1: Sidles' original proposal for the detection of NMR via coupling to a micromechanical oscillator, from [1].

1.1.1 First FDMR experiments

Although Sidles' initial suggestion involved coupling the spin directly with the oscillator, the experimental implementation adopted attempts to modulate the bulk magnetisation of the sample to generate a measurable force on the mechanical oscillator. This means that although the individual spins will precess at the Larmor frequency, the signals actually detected will be at the mechanical resonance frequency of the oscillator, which will be of the order of kilohertz, rather than MHz, or GHz.

1.1.1.1 Electron spin resonance based experiments

The first FDMR results were reported by Rugar and colleagues [5] in 1992. They measured ESR signals from a very small (< 30ng) sample of diphenylpicrylhydrazil (DPPH). DPPH is commonly used for making test and reference measurements in ESR. The experimental setup was quite different from that outlined in figure 1.1 and can be seen in figure 1.2. The first difference is that in Rugar's experiment, the sample of interest is mounted on the cantilever, with the magnetic source positioned near to it, rather than the other way round as in Sidles' proposal [1]. The cantilever

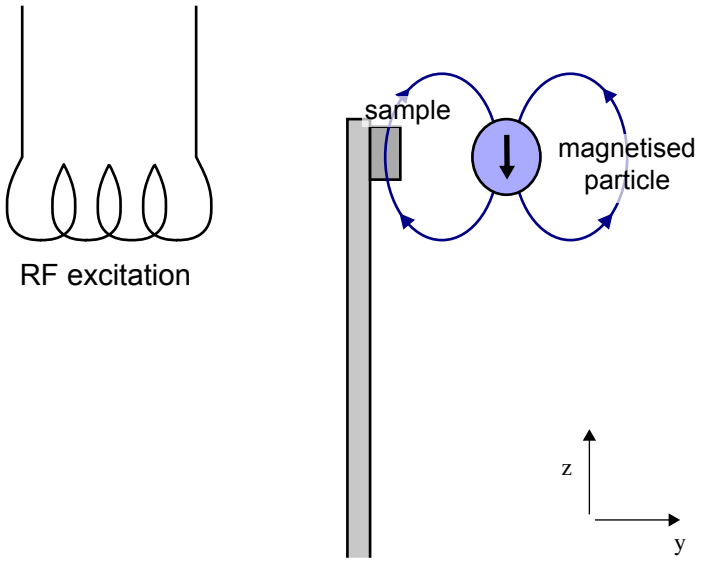

Figure 1.2: Experimental configuration used in the first ESR based FDMR experiments. From [5].

frequency is much lower than the spins' precession frequency. The field from the magnetic particle was supplemented using an electromagnet, enabling scanning and field modulation. To generate the cantilever-magnet interaction, the polarising magnetic field, parallel to the cantilever long dimension, was modulated, leading to a modulation in the sample magnetisation. (See the discussion in section 2.4.1.) As the dependence of the sample magnetisation on the polarising field is non-linear near resonance, this produced a magnetisation component at the second harmonic of the modulation frequency. The frequency was chosen so that its second harmonic would equal the mechanical resonant frequency of the cantilever, in order to minimise unwanted cantilever excitation. The cantilever motion was detected using a fibre optic interferometer. The magnetic fields used and the corresponding resonance frequency for the electron spins were low compared to those seen in conventional ESR: the external magnetic fields used were the order of millitesla, and the RF frequency was 220MHz for one experiment and 800MHz for another. The experiments were carried out in vacuum at room temperature. The vacuum raises the quality factor ("Q") of the cantilever by reducing the damping due to the finite viscosity of air.

1.1.1.2 Nuclear magnetic resonance based experiments

The first announcement of experimental force detected *NMR* was also by Rugar and co-workers [6], in 1994. The sample used was ammonium nitrate (NH_4NO_3), and the experimental configuration was similar to that employed above for the ESR experiments. The polarising field was much stronger (around 2.3T) and was produced by a superconducting magnet and an iron particle, achieving a field gradient at the sample of around 600Tm^{-1}. The modulation scheme used cyclic adiabatic inversion, which leads to an oscillating component in the sample's magnetisation, which in turn is detected via an interaction with the cantilever. A sensitivity of 1.6×10^{13} protons was obtained at room temperature, and a single-dimension imaging experiment had a spatial resolution of 2.6 microns. As with Rugar's first ESR based experiment described above, this was performed in vacuum at room temperature.

1.2 Subsequent progress in MRFM

Following the first experiments in force detected magnetic resonance outlined above, there was significant progress in both the NMR and ESR based versions, as well as the use of the technique with *ferromagnetic resonance* (FMR), which was reported by Zhang et al. in 1996 [7].

Until 1997, all the MRFM experiments so far reported used a similar geometry to that shown in figure 1.2. One of the most significant principles is that the sample of interest was mounted on the cantilever and magnetic gradient source (and also field in some cases) placed nearby. This, however, imposed limitations on the size and shape of the sample [8], so it was apparent that mounting the gradient source on the cantilever would be a desirable amendment. In 1997, Zhang and Hammel [8, 9] reported an experiment in which they measured the properties of AFM cantilevers on which had been mounted small particles of the permanent magnet NdFeB, when subjected to fields between ± 0.03T. They found that the interaction between the moment of the NdFeB particle and the external field led to the cantilever frequency being dependent on the external field. Because of this, it is desirable to minimise the probe magnetic moment when it is mounted on the cantilever.

Wago and colleagues successfully implemented a "tip-on-cantilever" MRFM system [10]

and used it to look at both ESR (again, in a sample of DPPH) and FMR (on a plate of yttrium iron garnet (YIG)) at an RF frequency of 12GHz (corresponding to magnetic fields of around 0.4T) at temperatures between 5 and 10 K. They published reconstructed three dimensional images of the spin density in the DPPH sample. This imaging capability is one of the most attractive features of MRFM and the progress in MRFM imaging is discussed in section 1.2.1. The different experimental geometries are briefly discussed in section 1.2.2.1.

1.2.1 Imaging experiments

The first images from MRFM were produced by Zugar and Rugar [11, 12] soon after the technique was first demonstrated. They used a similar experimental arrangement to that shown in 1.2, but with the probe field direction now primarily perpendicular to the long axis of the cantilever. There was no application of an external polarising field as described in [5]. Instead the magnetic probe provided both the polarising field, and the necessary field gradient for the force detection. The images were obtained by using a piezoelectric translation stage to scan the position of the magnet, which in this case was a 1mm long conical permanent NdFeB magnet with a diameter of 0.5 mm. The RF fields were of frequency 800–1610 MHz, and the tip field was modulated by means of a coil, positioned concentric with the NdFeB tip. The sample magnetisation was modulated at a frequency half that of the cantilever magnetic resonance, ie $\omega_c/2$ as also described in [5].

The field gradient produced by the magnetic tip meant that as the field varied with distance from the probe, different parts of the sample would come into resonance as the tip was scanned. The implications of this phenomenon are discussed more fully in chapter 3. In the scheme employed by Zuger and Rugar, the resulting surface of constant magnetic field produced by the tip, $B_t(x, y, z) = B_0$ took the form of a paraboloid near the tip. This yielded ring-like features in the force maps obtained from the scanning experiments, which were used to quantify the tip field. This knowledge was then used to reconstruct the spin density information to give images. The resolution was estimated to be about 1μm in the z direction and 5.3μm in the x and y directions. The estimated spin sensitivity achieved was estimated to be about 2×10^9, again working in vacuum to give a cantilever quality factor of $Q = 2000$.

In 1995, Hammel and co-workers published an account of an experiment in which

spins below the sample surface were imaged in one and two dimensions [13]. They achieved a vertical resolution of about 1μm and a sensitivity of 3×10^{11} electron spins, with a sample consisting of grains of DPPH on both sides of the cantilever.

Nuclear MRFM imaging in three dimensions was announced in 1996 by Zuger and co-workers [14]. Using deconvolution techniques they obtained a map of the real-space spin density of ^{1}H in a sample of ammonium nitrate after scanning the probe laterally and varying the frequency of the applied RF field. With a field gradient of $22G/\mu$m, an axial resolution of 3μm was obtained.

In 1997, Schaff and Veeman reported one dimensional NMR images of a multilayer structure of sodium chloride (NaCl) sandwiched between two layers of ammonium sulphate ($(NH_4)_2SO_4$). Their experiment gave them information on the spin distribution through the layer system. The experiments were also significant in that they were carried out at normal temperature and pressure.

1.2.2 Experimental considerations

As well as an understanding of the physical principles involved, the development of a technique such as MRFM requires considerable effort in the design and assembly of the necessary experimental apparatus. This section will outline some of the experimental considerations applicable to many MRFM experiments in general. The details specific to the work for this thesis will be described in chapters 7 and 8. The most widespread changes in the experiments were the move from a sample-on-cantilever approach to the tip-on-cantilever mentioned above and the introduction of scanning experiments enabling imaging to be performed. Different modulation schemes will also be briefly examined.

1.2.2.1 Experiment geometry

As mentioned earlier, there are two main experimental geometries that can be used to implement MRFM and these are “sample-on-cantilever” and “tip-on-cantilever” respectively, which are shown in figure 1.3. The tip-on-cantilever approach is perhaps more flexible as it allows many experiments to be performed using the same cantilever. This would be important if one wanted to study several systems with a consistent tip field. It is this approach that was adopted for the majority of the work described

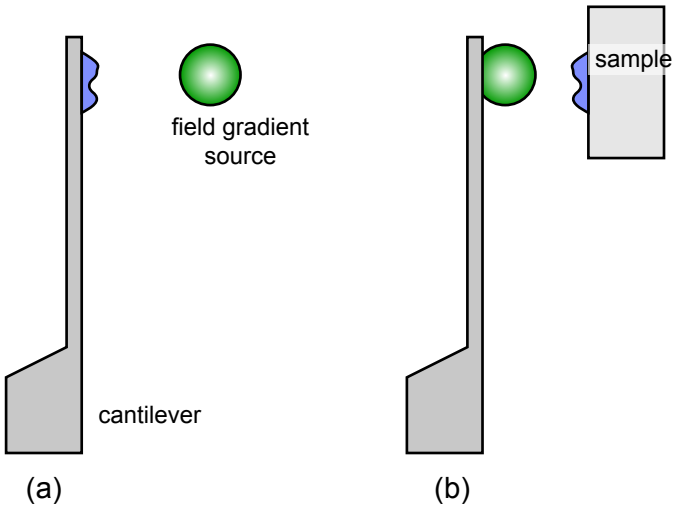

Figure 1.3: Possible geometries for an MRFM experiment. (a) Sample on cantilever, magnetic gradient source nearby. (b) Gradient source on cantilever, sample scanned nearby.

herein. (See chapters 7 and 8.) The main advantage of the sample-on-cantilever approach is that with no permanent magnet on the cantilever, its resonant frequency will not have the same dependence on the applied magnetic field due to torque on the tip. It will also be less susceptible to field gradients that will inevitably be present, so it would be possible to modulate the magnetic field without leading to large cantilever excitation off ESR resonance.

1.2.2.2 Scanning techniques

The approach taken to these scanning experiments owes much to atomic force microscopy (AFM) which has made the use of scanning probes a relatively common "bench-top" activity. Such systems typically use piezo ceramic materials such as PZT, $(\mathrm{Pb}(\mathrm{Zr},\mathrm{Ti})\mathrm{O}_3)$ which respond to the application of electric fields by changing length in either the direction perpendicular to the applied field, or the direction parallel to it. Piezo-electric scanners typically may employ elements for movement in each of the desired axes, or sets of stacked disks [15]. An alternative to this is to use a tube with four electrodes around the outside, which can provide movement in all

three directions [16], although transverse movement at constant z results in a slightly curved, rather than flat, surface. For distances greater than a few microns, "slip stick" systems may be employed, as, for example, in [17]. The details of the scanning system employed for our experiments will be described in chapter 8.

1.2.2.3 RF excitation

Because MRFM can be performed with a range of resonance techniques, there will be a large variation in the frequency of the RF fields used. The first ESR FDMR experiments, and subsequent NMR FDMR used fairly low (in microwave terms) RF frequencies and the RF necessary to perform the experiments was generated by small coils placed very close to the sample [5]. This approach was also taken for later experiments in which the RF frequencies were low, less than 1GHz [12, 14]. Some other experiments [18, 10] used a higher frequency at around 12GHz, which requires a more sophisticated way of transmitting signals. These experiments used samples positioned on top of microwave resonators based on microstripline. Semi-rigid coaxial cables are available for frequencies up to around 40GHz and even higher, but hollow metal waveguides of some sort are generally preferred at these higher frequencies.

1.2.2.4 Modulation methods

As with conventional ESR systems (see section 2.7), the experiments are designed so that modulation of one of the control variables leads to modulation of the measured quantity, allowing the use of phase sensitive detection to greatly increase the signal to noise ratio. There is, however, a choice of quantities to modulate and a choice of frequencies to use. Rugar's first experiment [5] used modulation of the external magnetic field after finding that amplitude modulation of the RF field resulted in large spurious excitation of the cantilever. An alternative procedure, known as *anharmonic* modulation has been used in order to minimise spurious coherent noise [19]. Two quantities are modulated at different frequencies, ω_1 and ω_2 chosen such that ω_1 and ω_2 sum to the cantilever resonant frequency, ω_c, but neither ω_1 or ω_2 is an integer fraction of ω_c. The magnetisation modulation that resulted from this contained a component at ω_c as well as harmonics of both ω_1 and ω_2. In this particular case, the modulated quantities were the RF field amplitude, B_1 and the polarising field, B_z. While reducing spurious excitation, anharmonic modulation does, however, add

complexity to the experiment, and it is preferable to modulate a single quantity if possible. This is particularly important when cantilever Qs are very high and therefore modulation frequency is critical.

A related modulation scheme exploited parametric mode coupling in the cantilever [20]. This involved modulating an external field to "pump" the cantilever at a frequency that was either the sum or difference of modal resonant frequencies of the cantilever. The pump field was detected by driving one mode and detecting the excitation of the other, even though the pump frequency itself was not at a cantilever resonant frequency.

A further modulation technique is a mechanical scheme as described by Marohn and colleagues [21], utilised with a sample-on-cantilever MRFM geometry. In this variation of anharmonic modulation, the position of the magnetic field gradient source (a piece of the permanent magnet material SmCo) was modulated with respect to the cantilever at frequency ω_m. With a cantilever resonant frequency of ω_c, the RF field was amplitude modulated at frequency ω_1 such that $\omega_1 + \omega_m = \omega_c$. This system of magnetisation modulation would have an advantage in situations where the cantilever resonant frequency is a function of the magnetic field.

1.3 Recent developments in MRFM

More groups have started to investigate FDMR/MRFM, although efforts are more focused on NMR applications than on ESR based ones. Imaging in at least one dimension has become quite common and a compact system for cryogenic use has been reported [22]. A group in Pisa has made 23GHz ESR measurements on DPPH using force detection and electromagnetic detection *simultaneously* [23], using a sample-on-cantilever scheme. The ability to record these data simultaneously is very useful for comparing results, and can be used to help quantify the effect of the applied field gradient by comparing the line-widths. This experiment was also interesting for its use of a whispering gallery mode resonator to yield large microwave fields. There have been other refinements, such as the use of digital RF generation [24].

A development that has resulted in an interest in MRFM beyond spectroscopy was the suggestion that it could be used as a basis for quantum computing. Berman and colleagues first outlined the idea of MRFM quantum computing [25], then a proposal

for such a system based on tellurium in silicon [26], involving an approach to detecting single spins earlier outlined by Berman and Tsifrinovich [27]. A recent publication by Ladd and et al. [28] proposed a possible quantum computer implementation based entirely on silicon which would use MRFM to measure the quantum states involved and require no electrical contacts or impurity dopants. Stipe and co-workers published an article concerning electron spin relaxation in the presence of the high field gradients used in MRFM (in this case $> 10^5 \mathrm{Tm}^{-1}$), which would be relevant in a quantum computing system where ferromagnetic materials were employed [29]. They also obtained very good sensitivity, detecting signals from the order of 100 spins in a resonant slice only 20nm thick. Another group have suggested a method of Fourier transform imaging based on MRFM [30]. Instrumental developments include the announcement of a superconducting microwave resonator for very low temperature experiments [31] and a method for measuring the temperature at the end of a cantilever based on the measurement of the susceptibility of oxygen in frozen air [32]. Resolution has also improved with an NMR based MRFM resolving between regions in a GaAs sample 500nm apart, sensitive to a sample volume of $50\mu\mathrm{m}^3$ [33].

1.4 Electron spin detection using scanning tunnelling microscopy

Scanning tunnelling microscopy has also been used to detect electron spins and itself offers the prospect of chemical specific imaging. Although the experimental details differ greatly from MRFM, the applications of the two techniques overlap. ESR-STM works on the principle that if STM is performed with the sample in a DC magnetic field, then the probability of an electron tunnelling may be affected by the Larmor precession of nearby spin centres at the sample surface [34]. The coupling may arise, for example, from dipolar or exchange interactions. The effect of this would be to add a modulation to the tunnelling current in the STM at the Larmor frequency. This high frequency modulation could be detected and thus provide information about the paramagnetic centres at the surface of the sample. Manassen and co-workers first did this with an oxidised silicon surface [34] and later with iron atoms in silicon [35]. More recently Durkan and Welland [36] reported similar experiments yielding STM-ESR spectra from a radical, BDPA, with results both from single molecules and clusters of molecules demonstrating the linear increase of the microwave frequency with magnetic

field. This was achieved by amplifying the high frequency part of the STM signal and observing it with a spectrum analyser. The technique has not yet been the subject of development as much as MRFM but could also provide another avenue for the practical implementation of quantum computing [37].

1.5 Motivation and overview

The preceding review demonstrates that there is now significant effort being made in MRFM related experiments involving NMR, ESR and FMR. ESR based FDMR is easier to detect due to the much larger magnetic moment of the electron.

The work herein is notable for being undertaken at much higher fields than other work so far on ESR based FDMR. High fields increase the spectral resolution and sensitivity of conventional ESR measurements and will also do so for FDMR as discussed in chapters 2 and 3. In a comprehensive review published in 1995, Sidles and colleagues showed with a simple argument that the force between a magnetic moment equivalent to that of a single electron and a gradient source consisting of a 300Å diameter saturated iron sphere 50Å away would be 7.8×10^{-16}N. This size of force is detectable using commercial AFM cantilevers, and is orders of magnitude greater than the detection limits of some experimental cantilevers. This shows that single-spin sensitivity should be within experimental reach and such an exciting prospect is an excellent motivation for MRFM. All contributions to sensitivity should be exploited and this is only one advantage of using high fields. The shorter wavelength of the resonant illuminating radiation means that it will be easier to integrate resonators with scanning probe techniques and the gain in resolution is attractive for MRFM spectroscopy. Higher fields also simplify some of the physics and some experimental consequences, as outlined in sections 3.1 and 7.3.1.1. We employ both magnet on cantilever and sample on cantilever experiments, each of which have their advantages, and use the cantilever perpendicular to the polarising magnetic field, rather than parallel as demonstrated in [5].

The following chapter describes the basic theory behind electron spin resonance spectroscopy and the motivations for its pursuit at high fields. In chapter 3 the theory behind force detected magnetic resonance is described, including an introduction to the mechanics of the cantilevers used and the fundamentals of the detection methods.

Some of these ideas are then illustrated in chapter 4 where the expected line-shapes from simple experiments are modelled, as well as the spatial response of a scanning experiment to point-like samples.

The main emphasis of the thesis is on instrumentation and chapter 5 describes the fibre-optic interferometry used in the project. Chapter 6 presents work with the cantilevers. Preliminary force detected ESR experiments and results are discussed in chapter 7 and the main goal of the project, the implementation of a high field magnetic resonance force microscope is detailed in chapter 8. Chapter 9 features a final discussion of the work and draws conclusions and presents an outline of future work.

Chapter 2

Introduction to conventional ESR spectroscopy

Electron spin resonance (ESR), also known as *electron paramagnetic resonance* (EPR) spectroscopy is a widely used and powerful technique which looks at the interaction of electrons in the sample of interest with a microwave or radio-frequency (RF) field whilst in a magnetic field. The information gathered can tell us about the local environment of the electrons: one can identify unknown ions, lattice defects, the lattice site and symmetry of a paramagnetic species, as well as information about the nuclei in the immediate vicinity of the absorbing spin [38].

ESR was first observed by Zavoisky in 1944 at 133MHz and two years later he made measurements at around 3GHz [39]. Since then it has become widely used in areas from solid state physics through organic chemistry to the study of proteins. This chapter will present an introductory description of the theory behind ESR systems and go on to discuss experimental systems with a view to their involvement in an MRFM system.

2.1 Magnetic moments

The magnetic moment of an electron spin, $\boldsymbol{\mu}_S$, is given by [38]:

$$\boldsymbol{\mu}_S = -g_S \beta \mathbf{S} \tag{2.1}$$

while that associated with orbital angular momentum, $\boldsymbol{\mu}_L$, is given by:

$$\boldsymbol{\mu}_L = -g_L\beta\mathbf{L} \tag{2.2}$$

where β in both cases is the *Bohr magneton*, defined by:

$$\beta = \frac{e\hbar}{2m_e} \tag{2.3}$$

where e is the magnitude of the electronic charge and m_e is the electronic mass, giving it a value (to 4 decimal places) of 9.2740×10^{-24} in Am^2 or JT^{-1}. $\mathbf{S}$ and $\mathbf{L}$ are the spin and orbital angular momentum respectively. The dimensionless g factors g_S and g_L relate the magnetic moments to the angular momenta and are equal to 2 and 1 respectively. In some systems, there is strong coupling between the spin and orbital angular momenta, and in this special case the total angular momentum $\mathbf{J}$ is obtained by vector addition:

$$\mathbf{J} = \mathbf{L} + \mathbf{S} \tag{2.4}$$

and the overall magnetic moment is $\boldsymbol{\mu}_J$. Due to the differing sizes of the magnetic moments due to spin and angular momentum, $\boldsymbol{\mu}_J$ *is not co-linear* with $\mathbf{J}$ but precesses about it.

By using the cosine rule, the effective g factor is given by the expression [40]

$$g = 1 + \frac{J(J+1) + S(S+1) - L(L+1)}{2J(J+1)} \tag{2.5}$$

Thus it can be easily be seen that for purely orbital angular momentum, g takes the value of 1, whereas for purely spin angular momentum, $g = 2$. In many systems where the atom is in a molecule or solid, averaging due to the random motion of the electron in its orbital reduces the effects of orbital motion and the g factor is close to its free value. This is called *quenching* [41]. For a completely free electron, $g = 2.0023$ but it can range both up and down depending on the system. Most ESR experiments are on systems close to $g = 2$.

In reality, the g factor is very often anisotropic and in the general case is a tensor with six (out of nine) independent components. For an arbitrary orientation of a crystal in a magnetic field, the situation is characterised by the g factor:

$$g = (g_{xx}^2 \cos^2\theta_x + g_{yy}^2 \cos^2\theta_y + g_{zz}^2 \cos^2\theta_z)^{\frac{1}{2}} \tag{2.6}$$

where $\theta_{x,y,z}$ are the angles between the respective axes and the field direction and $\cos\theta_{x,y,z}$ are the direction cosines of x, y and z. In spherical polar coordinates, the equation becomes:

$$g = (g_{xx}^2 \sin^2\theta\cos^2\phi + g_{yy}^2 \sin^2\theta\sin^2\phi + g_{zz}^2\cos^2\theta)^{\frac{1}{2}} \tag{2.7}$$

If the system is truly isotropic, then [42]:

$$g_{xx} = g_{yy} = g_{zz} \tag{2.8}$$

ESR measurements may be used to measure the values of the different components in the g tensor.

2.2 Interaction between a spin and a magnetic field

The interaction between a magnetic dipole $\boldsymbol{\mu}$ and a magnetic field of strength $\mathbf{B}_z$ applied along the z axis is just the scalar product of the two:

$$\text{Energy} = -\boldsymbol{\mu}.\mathbf{B}_z \tag{2.9}$$

Thus the separation between neighbouring energy levels is

$$\Delta E = |g\beta B_z| \tag{2.10}$$

in joules, when B_z is in tesla. The splitting is illustrated in figure 2.1. This forms the basis for a method of spectroscopy: a transition of spin between energy levels can be associated with the absorption or emission of energy in the form of radiation at the angular frequency given by $\omega = \Delta E/\hbar$.

This frequency, ω, is known as the *Larmor precessional frequency* and classically is the frequency at which the spin vector precesses about the direction of an applied magnetic field. Figure 2.2 shows the allowed orientations of a spin $\frac{1}{2}$ particle and its Larmor precession. This applies to both nuclear spins (i.e. NMR) and electron spins (ESR).

It may, at first thought, be assumed that in the presence of an external magnetic field, all the moments would simply align themselves with the field, thus occupying

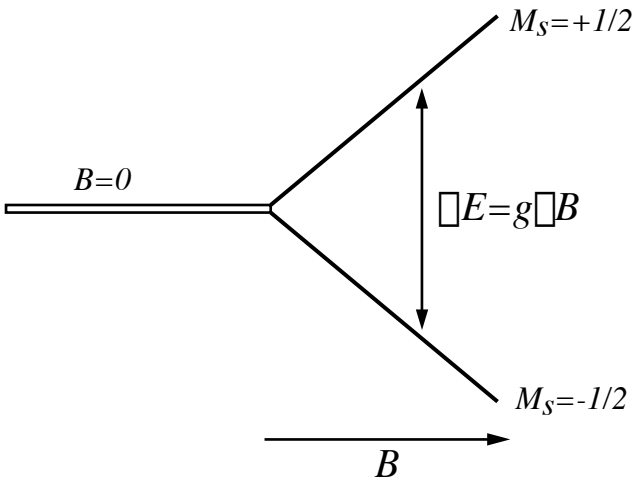

Figure 2.1: Energy levels for an electron spin ($S = \frac{1}{2}$) in an applied field of strength B. From [43].

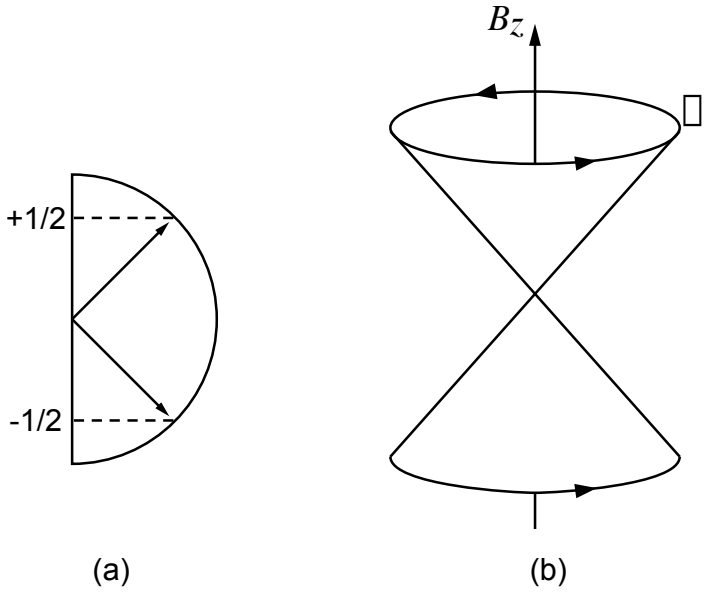

Figure 2.2: (a) The allowed spin orientations for a spin = $\frac{1}{2}$ particle, (b) the Larmor precession of such a particle, from [44]

the lowest energy state. Due to thermal effects, however, this does not happen. With an applied field, the energy levels are split. For a situation with two levels, such as our spin $\frac{1}{2}$ system, the separation of the levels will be ΔE. Statistical mechanics tells us that at a temperature, T, the ratio of the populations of the two levels will be:

$$\frac{N_{upper}}{N_{lower}} = \exp\left(-\frac{\Delta E}{k_B T}\right) \tag{2.11}$$

where k_B is Boltzmann's constant. It can be seen, therefore, that at room temperature and 0.3T (a typical field for ESR experiments), $\Delta E/k_B T$ will be of the order 10^{-3}, so the two populations will be nearly equal, with only slightly more spins in the lower energy state.

2.3 The spin Hamiltonian

The two level example looked at in section 2.1 is probably the simplest that can be described. For "real" situations where the electron may interact with other particles (such as nuclei or other electrons) we need to use the *spin Hamiltonian*, $\mathcal{H}$ of the system. This can be described as follows [38]:

$$\mathcal{H} = \mathcal{H}_{\text{elect}} + \mathcal{H}_{\text{cf}} + \mathcal{H}_{LS} + \mathcal{H}_{SS} + \mathcal{H}_{\text{Zee}} + \mathcal{H}_{\text{hfs}} + \mathcal{H}_{Q} + \mathcal{H}_{N} \tag{2.12}$$

where the contributing terms are, respectively, the *electronic energy*, the *crystal field energy*, the *spin-orbit interaction*, the *spin-spin* interaction, the *Zeeman energy*, the *hyperfine structure*, the *quadrupole energy* and the *nuclear spin energy.*

$\mathcal{H}_{elect}$ is the electronic energy of the paramagnetic ion in the free state and $\mathcal{H}_{cf}$ is the interaction of the free ion's electronic structure with the crystalline electric field. This term helps to determine the g factor. The other terms in the spin Hamiltonian can be expressed as:

$$\mathcal{H}_{LS} = \lambda \mathbf{L}.\mathbf{S} \tag{2.13}$$

$$\mathcal{H}_{SS} = D\left[S_z^2 - \frac{1}{3}S(S+1)\right] \tag{2.14}$$

$$\mathcal{H}_{Zee} = \beta \mathbf{H}.(\mathbf{L} + 2\mathbf{S}) = \beta(g_x H_x S_x + g_y H_y S_y + g_z H_z S_z) \tag{2.15}$$

$$\mathcal{H}_{hfs} = (A_x S_x I_x + A_y S_y I_y + A_z S_z I_z) \tag{2.16}$$

$$\mathcal{H}_Q = \left\{ \frac{3eQ}{4I(2I-1)} \right\} \left(\frac{\partial^2 V}{\partial z^2} \right) \left[I_z^2 - \frac{1}{3} I(I+1) \right] \tag{2.17}$$

$$\mathcal{H}_N = \gamma \beta_N \mathbf{H}.\mathbf{I} \tag{2.18}$$

In equations 2.13 to 2.18, the previously undefined terms are as follows: λ is the spin-orbit coupling constant. S_z and L_z are the z components (where $\hat{\mathbf{z}}$ is parallel to $\mathbf{H}$) of the spin and orbital angular momenta respectively. D is the zero field splitting constant. A_z is the zz component of the hyperfine coupling constant A. I_z is the z component of the *nuclear* spin, $\mathbf{I}$. Q is the electric quadrupole moment. V is the crystalline electric field potential. β_N is the nuclear magneton. γ is the *gyromagnetic ratio* given by:

$$\gamma = \frac{g\beta}{\hbar} = \frac{ge}{2m_e} \tag{2.19}$$

Essentially, ESR measures the Zeeman term of the Hamiltonian and studies the ways in which it affects and is affected by the other terms of the hamiltonian.

2.4 Relaxation

If the spinning particles were frictionless gyroscopes, then unless a radiation field was present at the correct frequency to provide the necessary energy, they would not be able to orient themselves to provide the correct statistical distribution when a magnetic field was applied [44]. This is because there is no mechanism by which the excess energy could be removed, resulting in the system having a *high spin temperature*. Such particles do, however, re-orient themselves in an external magnetic field without such a radiation field present, so there must be a mechanism by which energy can be lost to the particle's surroundings or to other particles. This mechanism is referred to as a *relaxation process*.

We can define a *spin temperature*, T_s by replacing T in equation 2.11 by T_s. Consider the situation when the spin system is illuminated by an EM pulse with a frequency such that $h\nu = \Delta E$ (see figure 2.1). The absorption by the spins results in the system gaining energy from the illuminating field, raising the ratio $N_{\text{upper}}/N_{\text{lower}}$. The system can be thought of as being "hotter" than its surroundings, as T_s is now greater than T. The spin system interacts with its surroundings and loses energy to them, with T_s once again approaching T. This energy is lost in an exponential decay [42]:

$$\delta E = \delta E_0 e^{-\left(\frac{t-t_0}{\tau_1}\right)} \tag{2.20}$$

where δE_0 is the energy gain at time t_0 and τ_1 is a parameter characterising the energy flow from the local system to its surroundings, known as the *spin-lattice relaxation time*. (The finishing state (i.e. $t \to \infty$) is that T_s is once again equal to T.) The mechanisms of spin-lattice relaxation are discussed in 2.4.2. There is also a characteristic time for energy exchange *within* the system. This is the spin-spin, or transverse, relaxation time and is introduced in section 2.4.1.

2.4.1 The Bloch model of spin relaxation

The Bloch equations [42] provide a useful model for spin relaxation. Without an external magnetic field, any bulk magnetisation $\mathbf{M}$ will be fixed and will have components M_x, M_y and M_z, where x, y and z denote an arbitrary set of cartesian axes. When the system is subject to a steady homogeneous field, $\mathbf{B}$, in *the absence of relaxation* it is in equilibrium. $\mathbf{M}$, however, is not fixed in space, and has the equation of motion:

$$\frac{d\mathbf{M}}{dt} = \gamma \mathbf{M} \wedge \mathbf{B} \tag{2.21}$$

If we set up our axes such that $\mathbf{B}$ is along $\underline{\mathbf{z}}$, then we get:

$$\frac{dM_x}{dt} = \gamma B M_y \tag{2.22}$$

$$\frac{dM_y}{dt} = -\gamma B M_z \tag{2.23}$$

$$\frac{dM_z}{dt} = 0 \tag{2.24}$$

the solutions to which are:

$$M_x = M_\perp^\circ \cos \omega_B t \tag{2.25}$$

$$M_y = M_\perp^\circ \sin \omega_B t \tag{2.26}$$

$$M_z = M_0 \tag{2.27}$$

The above equations show that $\mathbf{M}$ precesses around $\mathbf{B}$ at the *Larmor* frequency, $\omega_B = -\gamma B$, provided that $M_\perp^\circ$ is non-zero. If there is a sudden change in the magnitude or direction of $\mathbf{B}$, then M_x, M_y and M_z, referenced to the new field direction, relax to equilibrium at different rates. Assuming that M_x and M_y relax at the same rate, this may be characterised by the time τ_2, the *transverse relaxation time*, taking its name from the transverse direction of M_x and M_y with respect to M_z. (More will be said about both τ_1 and τ_2 in subsections 2.4.2 and 2.4.3.) We now have:

$$\frac{dM_x}{dt} = \gamma B M_y - \frac{M_x}{\tau_2} \tag{2.28}$$

$$\frac{dM_y}{dt} = -\gamma B M_x - \frac{M_y}{\tau_2} \tag{2.29}$$

$$\frac{dM_z}{dt} = \frac{M_0 - M_z}{\tau_1} \tag{2.30}$$

The solutions to the above equations feature the decay of M_x and M_y to zero. Note that in the absence of relaxation (i.e. $\tau_1 = \tau_2 = \infty$), the above equations reduce to the first form given.

We now introduce an oscillating magnetic field, $\mathbf{B_1}$, with positive angular frequency ω, in a direction perpendicular to $\mathbf{B}$, i.e. $\mathbf{B_1}$ rotates in the x-y plane about z. Thus the x and y components of the field (as observed from the laboratory frame of reference) vary sinusoidally out of phase with each other, while there is no z component of $\mathbf{B_1}$. If we now take this into account, we may obtain new expressions for the magnetisation. The resulting equations of motion are known as the *Bloch Equations* and are:

$$\frac{dM_x}{dt} = \gamma(BM_y - B_1 \sin \omega t M_z) - \frac{M_x}{\tau_2} \tag{2.31}$$

$$\frac{dM_y}{dt} = \gamma(B_1 \cos \omega t M_z - BM_x) - \frac{M_y}{\tau_2} \tag{2.32}$$

$$\frac{dM_z}{dt} = \gamma(B_1 \sin \omega t M_x - B_1 \cos \omega t M_y) - \frac{M_z - M_z^\circ}{\tau_1} \tag{2.33}$$

assuming that γ is the same for the directions of both $\mathbf{B}$ and $\mathbf{B_1}$.

$\mathbf{M}$ precesses about $\mathbf{B}$, so we transform to a frame of reference that rotates about $\hat{\mathbf{z}}$ with frequency ω, taking the new axis $\hat{\mathbf{X}}$ to be parallel to $\mathbf{B_1}$. The new $\hat{\mathbf{Z}}$ axis is the same as the laboratory $\hat{\mathbf{z}}$ axis and of course $\hat{\mathbf{Y}}$ is perpendicular to both $\hat{\mathbf{X}}$ and $\hat{\mathbf{Z}}$. This results in another set of differential equations which, when solved, give us the steady state (i.e. $d\mathbf{M}/dt = 0$ in the rotating frame) values for M_X, M_Y and M_Z (which is unchanged by the transformation, and thus just equal to M_z) as [42]:

$$M_X = -M_0 \frac{\gamma B_1 (\omega_B - \omega)\tau_2^2}{1 + (\omega_B - \omega)^2\tau_2^2 + \gamma^2 B_1^2 \tau_1 \tau_2} \tag{2.34}$$

$$M_Y = M_0 \frac{\gamma B_1 \tau_2}{1 + (\omega_B - \omega)^2\tau_2^2 + \gamma^2 B_1^2 \tau_1 \tau_2} \tag{2.35}$$

$$M_z = M_0 \frac{1 + (\omega_B - \omega)^2\tau_2^2}{1 + (\omega_B - \omega)^2\tau_2^2 + \gamma^2 B_1^2 \tau_1 \tau_2} \tag{2.36}$$

It should be noted that M_X is in phase with $\mathbf{B_1}$, whereas M_Y is $\pi/2$ out of phase. It can be seen that at resonance (i.e. $\omega = \omega_B$), as B_1 increases indefinitely, $\mathbf{M}$ vanishes. This is known as *saturation*. It is this effect that is exploited by our implementation of MRFM, as will be explained in section 3.1.1. The expressions may be treated to transform back into the laboratory reference frame. However, we are primarily interested in M_z which is unaffected by the change of frames, whereas conventional ESR looks at M_X and M_Y. M_X and M_Y are related to the complex susceptibility, $\chi = \chi' + i\chi''$:

$$\chi' = +\kappa\mu_0 \frac{M_X}{B_1} \tag{2.37}$$

$$\chi'' = -\kappa\mu_0 \frac{M_Y}{B_1} \tag{2.38}$$

where κ is the relative permeability of the material. The line width which may be obtained from the expressions for the magnetisation is discussed in chapter 3, as is the form of M_0 for an $S = 1/2$ system.

2.4.2 Spin-lattice (longitudinal) relaxation

Spin-lattice relaxation is the process whereby energy passes from the spin system to the crystal lattice, and is characterised by the time τ_1. The process can be thought of as a two step process [45]: energy passes from the spin system to the lattice, then

from the lattice to a heat bath or reservoir that the sample is in contact with. The rate of energy transfer between the spins and the bath will depend on the coupling of the spins to the lattice and the coupling of the lattice to the bath. If the characteristic times of these processes are τ_1 and τ_{ph}, then the overall characteristic time τ is given by [45]:

$$\frac{1}{\tau} \sim \frac{1}{\tau_1} + \frac{1}{\tau_{ph}} \tag{2.39}$$

It can be seen that τ will be mostly set by the smaller of τ_1 and τ_{ph}. It will be assumed that τ_1 is much larger than τ_{ph}, thus energy can pass from the lattice to the thermal reservoir faster than it passes from the spins to the lattice.

2.4.2.1 The direct process

There are several processes whereby spin-lattice relaxation takes place. The most straightforward is known as the *direct process* [39] in which a single phonon is emitted or absorbed by the system and takes place at low temperatures. This phonon will have $\hbar\omega = \Delta E$, where ω is the phonon frequency and ΔE is the separation between the two levels of the transition.

2.4.2.2 The Raman process

At temperatures much larger than $\hbar\omega/k_B$, the phonon density peaks at frequencies much higher than ω [39]. It is more efficient for the system to absorb a phonon of high frequency, $\omega_{\nu_1} \approx \omega_{max}$, where ω_{max} is the phonon frequency at which the phonon density peaks, then subsequently emit a phonon with frequency $\omega_{\nu_2} = \omega_{\nu_1} \pm \omega$. This can be though of as a transition to a virtual energy level, followed by a transition back to a ground state level with a different spin state. This is known as a *Raman process*.

2.4.2.3 The Orbach process

The two photon process becomes more efficient if there is an actual energy level with the needed energy difference. The thermal energies dealt with are low, so this actual level must be a low lying excited state [39]. This type of two photon process is known as the *Orbach process*.

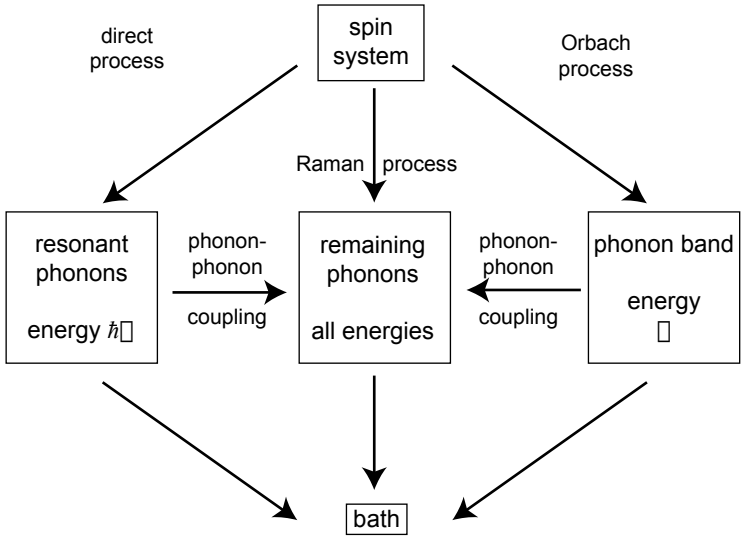

Figure 2.3: Paths for spin-lattice relaxation, taken from [39]. The arrows indicate the direction of energy transfer, assuming the phonon bath to be "colder" than the spin system.

Figure 2.3 shows an overview of the various paths for spin-lattice relaxation.

2.4.3 Spin-spin (transverse) relaxation

In the previous sub-section we discussed the passage of energy from the spin-system to its environment. This energy exchange is not required for *spin-spin* or *transverse* relaxation, but obviously there has to be some form of interaction with the surroundings. A two-spin flip-flop process may be energy conserving, with one spin gaining the energy that the other loses. This is spin-spin relaxation [39]. Thus, the spin system loses some of its coherence. The spin-spin relaxation process is usually characterised by the relaxation time τ_2, but as it is more complicated than the spin-lattice relaxation processes, it is not fully describable in this way [46].

2.5 Resolution and sensitivity

In order to extract the greatest amount of information using ESR, it is advantageous to maximise the performance of the system. This section will briefly look at the issues affecting the *sensitivity* (signal to noise) and the *resolution* (smallest meaningful field difference) of the system.

Assuming a signal to noise ratio of one, the minimum detectable number, N_{min} of paramagnetic centres in an ESR cavity, is reasonably given by [42]:

$$N_{min} = \frac{3V_c k_b T_s \Gamma}{2\pi g^2 \beta_e^2 S(S+1) B_r Q_u} \left(\frac{F k_b T_d b}{P_0} \right)^{\frac{1}{2}} \tag{2.40}$$

The previously undefined quantities used in equation 2.40 denote the following: V_c is the cavity volume, assuming that the TE_{102} mode is the one used. T_s is the sample temperature. Γ is the half-width at half-maximum of the absorption line, in milliTesla. B_r is the magnetic field, again in mT, at line centre. Q_u is the effective *unloaded* quality factor of the cavity. T_d is the temperature of the RF detector. b is the bandwidth in Hz of the detecting and amplifying part of the system. P_0 is the microwave power, watts, incident on the system. F is a noise factor resulting from causes other than the thermal noise. An ideal spectrometer would have $F = 1$ but a typical value for a real system could be 100 [42]. Equation 2.40 assumes that the lineshape is Lorentzian and that the RF power does not saturate the system. A typical value for N_{min} could be on the order of 10^{11} [42] for a 10GHz spectrometer at room temperature, and the minimum detectable concentration of spins is on the order of 10^{-9} M.

The resolution of an ESR system will depend on the instrumentation. The field will have a finite homogeneity and stability which limits the ability to know that a particular measurement is being made at a particular field. The resolution will also vary from sample to sample: two features in a spectrum may be separated by a certain amount, but the ability to resolve them will depend on the width of the individual features as well and this will depend on the sample properties.

2.6 Why use high field ESR?

High field electron spin resonance is generally more technically demanding, so one would reasonably ask what benefits it yields over lower field techniques. This section illustrates the gains over "normal" field ESR. The technical difficulties associated with higher fields are presented in section 2.7.1.

2.6.1 Sensitivity and HF ESR

It can be seen from equation 2.40 that the smallest detectable number of spins goes as $1/B$ so that moving from 9GHz to 90GHz offers an order of magnitude increase in sensitivity. There are also other increases in sensitivity. The smaller resonators employed at higher fields mean that the sample fills a larger portion of the cavity, resulting in improved signal to noise, also implicit in equation 2.40.

2.6.2 Resolution and HF ESR

Another of the main reasons for pursuing ESR at high fields is that there is an increase in the resolution with which the g factor of a system can be determined. The separation in field, ΔB, between two lines with g factors g_1 and g_2 can be expressed as:

$$\Delta B = \frac{h\nu}{\beta}\left(\frac{1}{g_1} - \frac{1}{g_2}\right) \tag{2.41}$$

which is easily inferred from equation 2.10. If the linewidths of the relevant transitions do not increase with field then they should be resolvable eventually. The value for the field when this will happen is given by [47]:

$$B_0 \frac{g_1 - g_2}{g_{iso}} > \Delta B_{1/2} \tag{2.42}$$

where B_0 is magnetic field, g_{iso} the isotropic g-factor and $\Delta B_{1/2}$ is the inhomogeneous linewidth. This expression is the *high field condition* and occurs at different fields B_0 for different systems. The extra resolution of high field ESR makes it useful for studying molecular structure as it is easier at high fields to see the individual lines and to interpret the spectra [48]. Site directed spin labeling is another area that benefits from the increased resolution. High field ESR has been applied to the study

of, among other things, free radicals, solid state defects and organic semiconductors.

2.7 ESR spectrometers

The earlier parts of this chapter establish that we can use spectroscopy to look at the electronic structure of suitable systems. We now proceed to look briefly at the instrumentation used in ESR experiments.

An ESR system has several core requirements: a magnet, a suitable RF source and means of detecting the RF signals obtained. A great deal of ESR is carried out with frequencies around 9GHz, in the part of the microwave region designated "X-band". In spectrometers of this type, the magnetic fields used are typically around 0.3T so large electromagnets, capable of providing fields of over 1T are suitable. The field scales with the RF frequency (as shown in section 2.2) so significantly higher frequencies, such as 94GHz (in W-band) require superconducting magnets.

Although a spectrometer's design will vary with the task it is intended for, there are enough similarities to show a "typical" system in figure 2.4. At resonance, the presence of the sample has a large effect on the cavity properties and hence on the amount of microwave power reflected back. The circulator is a device which directs microwave power from the oscillator down into the cavity, but directs the reflected power from the cavity to the detector and so isolates the oscillator from the cavity and detector. Most spectrometers actually detect a derivative signal as the magnetic field is modulated and the resulting variation in detector signal is detected with a phase sensitive detector. A resonant cavity is used to hold the sample in order to achieve the largest possible B_1 field amplitude, but non-resonant arrangements may also be employed, depending on the experiment.

2.7.1 High field systems

The most common difference between the implementation of high-field and low-field ESR systems is the magnet systems employed: fields above two Tesla or so require the use of a superconducting magnet. This may be either a single solenoid or a split coil. The required presence of the cryogens needed to keep the magnet cold (usually a helium reservoir surrounded by a nitrogen cooled radiation shield and a vacuum)

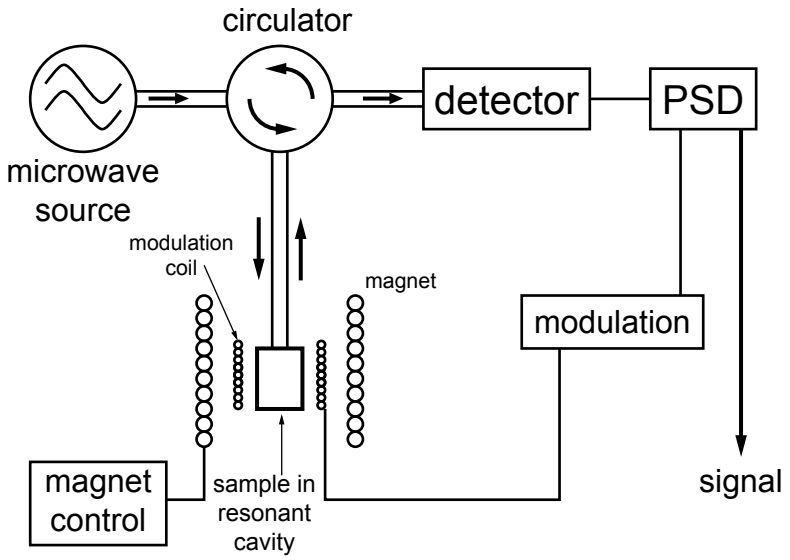

Figure 2.4: A simple schematic of a typical ESR spectrometer

means that such systems are often more physically awkward to work with. The bore of the magnet may not necessarily be at room temperature, which complicates the loading of samples and the setting up of measurements.

The approach to the experiment may also be different from the signal-processing point of view. At frequencies around 90GHz and above, the hollow single mode rectangular wave-guides used for propagating microwaves are fairly lossy (the order of a few dB per metre). It is still possible to use conventional overmoded waveguide at 90GHz and even higher frequencies in spectrometers, as in a high field system available from Bruker[1]. An alternative approach is to use a group of techniques known collectively as *quasi-optics* [49]. Quasi-optics combines microwave techniques with those from "conventional" optics, using elements such as lenses, mirrors, polarisers, wave-plates and Faraday rotators. Quasi-optical systems can be built with much larger bandwidths than all-waveguide systems and can offer lower loss with better performance than all-waveguide systems. This approach to ESR instrumentation was first used by Lynch et al. at Cornell [50], and has since been developed and improved by various groups world wide [51, 52]. The St Andrews spectrometer is a quasi-optical

[1]http://www.bruker.de

design built out of a series of metal half-cubes which support the various quasi-optical components. The spectrometer operates in the frequency range 80GHz to 200GHz and from temperatures of 2K to 300K.

Chapter 3

Principles of force detected magnetic resonance

Force detected magnetic resonance is a technique that combines spectroscopy, scanning probe microscopy and other disciplines. This chapter details the fundamental principles underlying FDMR and MRFM, building on the introduction to ESR outlined in chapter 2 to discuss the interaction between the field gradient source and the sample. We then look at the cantilevers used in force detection and the fibre optic interferometry to detect their motion before going on to look at the the noise processes that will limit our measurements.

3.1 The tip-sample interaction in MRFM

This section examines the process at the heart of an FDMR experiment: the interaction between the magnetic field gradient source and the sample being measured.

3.1.1 Sample magnetisation

Consider a situation in which we place a spin-containing sample in an external magnetic field. The external field, $\mathbf{B}$, parallel to the z axis and of magnitude B_z will result in the partial polarisation of the spins in the sample, giving rise to a sample magnetisation of magnitude M_0, parallel to $\mathbf{B}$. If the atoms under consideration have

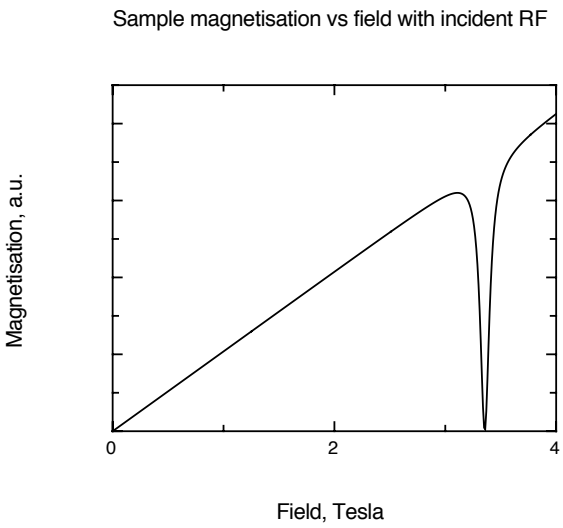

Figure 3.1: Sample magnetisation as a function of applied field with an applied RF field of frequency 94GHz, calculated using equation 3.2. A dip in magnetisation is visible around the resonant field condition at 3.36 Tesla, as described by equation 3.2 for the condition $B_1^2\tau_1\tau_2 \gg 1$. The dip in this case is very wide as a large value of B_1 was used deliberately to illustrate the point. The fact that the magnetisation actually drops right to zero indicates that *saturation* has occurred.

spin 1/2, the magnetisation can be expressed as [53]:

$$M_0 = \mu_S n \tanh\left[\frac{\mu_S B_z}{k_B T}\right] \tag{3.1}$$

where n is the number of spins per unit volume in the sample, and μ_S is the moment of a single spin, as defined in section 2.1. Magnetisation is magnetic moment per unit volume, so the magnetisation is measured in Am^{-1}. At room temperatures and at 3 Tesla, $k_B T$ is, at the order of 4×10^{-21}J, about 70 times greater than $\mu_S B_z$, however at liquid helium temperatures (the order of 4 Kelvin), and fields of a few Tesla, the two quantities become comparable. As described in section 2.4.1, when an RF field of angular frequency ω and amplitude B_1 is applied transverse to $\mathbf{B}$, the magnetisation

is changed as given by equation 2.36, which can be recast as [18]:

$$M_z = M_0 \left[1 - \frac{\gamma^2 B_1^2 \tau_1 \tau_2}{1 + (\gamma B_0 - \omega)^2 \tau_2^2 + \gamma^2 B_1^2 \tau_1 \tau_2} \right] \tag{3.2}$$

where τ_1 and τ_2 are the spin-lattice and spin-spin relaxation times respectively. When the resonance condition is met (i.e. when $\omega = \gamma B_0$), M_z becomes $M_0 - \delta M_z$, where

$$\delta M_z = \frac{M_0 \gamma^2 B_1^2 \tau_1 \tau_2}{1 + \gamma^2 B_1^2 \tau_1 \tau_2} \tag{3.3}$$

It can be seen that at, and close to, the resonance condition, the presence of the RF field will lead to a reduction in the sample magnetisation compared to that at external fields further from the resonance condition. This is shown in figure 3.1. The full width at half minimum of the dip is dependent on the illuminating microwave field amplitude and is given by

$$\Delta B = 2\sqrt{\frac{\gamma^2 B_1^2 \tau_1 \tau_2 + 1}{\gamma^2 \tau_2^2}} \tag{3.4}$$

and the minimum possible dip width (i.e. for $B_1 = 0$) is

$$\Delta B_{\min} = \frac{2}{\gamma \tau_2} \tag{3.5}$$

showing the line-width dependence on τ_2. The term $\gamma^2 B_1^2 \tau_1 \tau_2$ is the *saturation* term and may be ignored if much less than one. The applied RF is usually described by the RF *power*. The field strength, B_1, arising from this is given by the expression [47]

$$B_1 = C \frac{\mu_0 Q_L}{\omega_0 V_{cav}}^{\frac{1}{2}} P^{\frac{1}{2}} = K P^{\frac{1}{2}} \tag{3.6}$$

where B_1 is in tesla and P is in watts. C is a constant depending on the cavity mode, Q_L is the loaded Q factor of the cavity, ω_0 is the angular frequency and V_{cav} is the effective volume of the cavity.

3.1.2 The dipole-dipole interaction

Consider the situation where we have a magnetic dipole of moment **m** at the origin of the coordinate system as shown in figure 3.2. The field produced by the moment

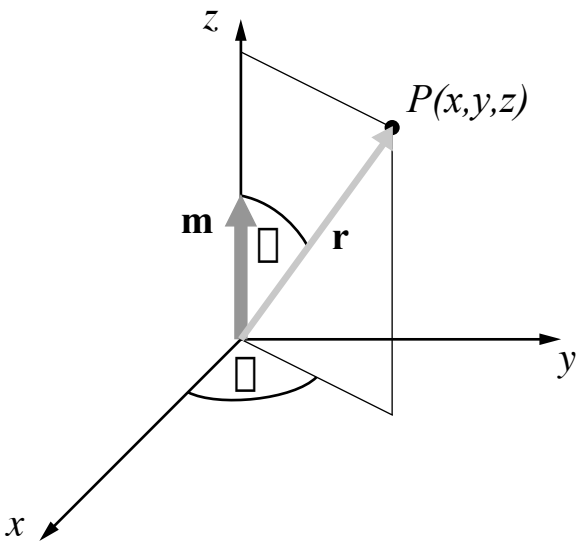

Figure 3.2: A magnetic dipole moment, **m**, at the center of a rectangular and a polar coordinate system sharing the same origin.

m is made up of the components [54]:

$$B_r = \frac{\mu_0}{4\pi}\frac{2m}{r^3}\cos\theta \tag{3.7}$$

$$B_\theta = \frac{\mu_0}{4\pi}\frac{m}{r^3}\sin\theta \tag{3.8}$$

$$B_\phi = 0 \tag{3.9}$$

resulting in a field

$$\mathbf{B}(\mathbf{r}) = \frac{\mu_0}{4\pi}\frac{m}{r^3}(2\cos\theta\hat{\mathbf{r}} + sin\theta\hat{\boldsymbol{\theta}}) \tag{3.10}$$

Note the distinction between **r** (the position vector for point P), r (the magnitude of the position vector) and $\hat{\mathbf{r}}$ (the unit vector in the direction of **r**). $\hat{\boldsymbol{\theta}}$ is the unit vector in the direction of increasing θ, perpendicular to $\hat{\mathbf{r}}$. We are concerned only with the z component of the field due to the dipole, so we can find that

$$B_z = \frac{\mu_0 m}{8\pi r^3}(3\cos 2\theta + 1) \tag{3.11}$$

which is a scalar quantity merely giving the magnitude of the z component. The gradient of this field is given by

$$\nabla B_z = \frac{-3\mu_0 m}{8\pi r^4}\left((3\cos 2\theta + 1)\hat{\mathbf{r}} + \sin 2\theta\hat{\boldsymbol{\theta}}\right) \tag{3.12}$$

The z component of this gradient is thus

$$\frac{\partial B_z}{\partial z} = \frac{\mu_0 m}{4\pi r^4}\left(\cos\theta(9 - 15\cos^2\theta)\right) \tag{3.13}$$

The component of the gradient along a direction perpendicular to $\hat{\mathbf{z}}$, which we can denote as $\hat{\boldsymbol{\rho}}$ is

$$\frac{\partial B_z}{\partial \rho} = \frac{\mu_0 m}{4\pi r^4}\left(\sin\theta(15\sin^2\theta - 12)\right) \tag{3.14}$$

We resolve the field and gradient into these two directions as our experiment will feature a magnet on a cantilever, with its moment in the z direction, perpendicular to the plane of the cantilever. Only the z gradient needs to be considered for the deflection of the cantilever, but the gradient in the lateral directions will have an influence on the attainable resolution, as discussed in section 3.1.4. If we have a second magnetic moment, $\mathbf{m_2}$, at position P and parallel to the z axis, then it will experience a total force given by

$$F_{m_2} = \frac{\mu_0 m m_2}{4\pi r^4}\left(\cos\theta(9 - 15\cos^2\theta)\hat{\mathbf{z}} + (\sin\theta(15\sin^2\theta - 12)\hat{\boldsymbol{\rho}}\right) \tag{3.15}$$

To relate this to our planned experiment, we can say that $\mathbf{m_1}$ is a magnetic particle placed on the free end of a cantilever. Then $\mathbf{m_2}$ is the magnetic moment of a volume element of our partially polarised spin containing sample nearby (the order of microns or less). There will thus be a force on the cantilever due to the interaction of the sample magnetisation with the field gradient created by the magnetic particle. (It is also appropriate to consider the situation as the interaction of the probe magnetic moment in the field created by the sample, as the result is the same.) The force on the cantilever can be modulated by modulating the sample magnetisation, via modulating the amplitude or frequency of the illuminating microwaves B_1 when the sample is near the resonant condition, as outlined in section 3.1.1. The probe magnet will obviously not be a point-like dipole but a finite size, as discussed in section 3.1.6.

In the above case, the z direction is clearly defined due to the high fields being used. Some early ESR MRFM imaging experiments [11] used only the field due to a gradient source to polarise the sample. This could lead to an ambiguity about

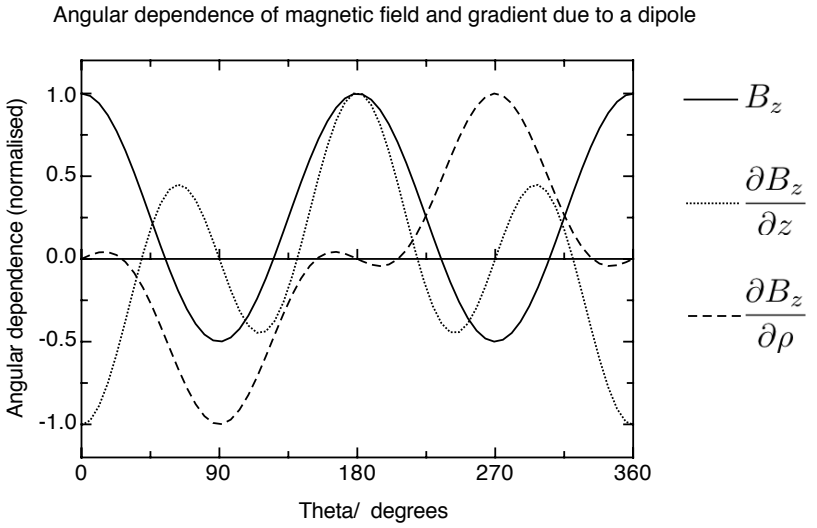

Figure 3.3: Normalised angular dependencies of the z component of the field due to a dipole, and its derivatives with respect to z and ρ.

which direction is defined as z, as the tip field direction will vary throughout the sample. With a large external field, the z direction is always clearly defined. If the magnetic tip is large compared to the sample, this is unlikely to be an issue but for magnet-on-cantilever FDMR with no external field, the tip-sample interaction would be considerably complicated.

3.1.3 Spatial selectivity in MFRM

In order for a spectroscopic technique to be applied to imaging, there needs to be a mechanism whereby the *position* of the spin is encoded in the signal. In magnetic resonance imaging (MRI), this is done by applying known spatial field gradients to the object under investigation and the position of the signal source is derived from knowledge of the applied uniform and varying fields [55]. A related approach is taken in MRFM in that a field gradient is used to deliver spatial discrimination, however the gradient used is that which provides the coupling between the probe and the sample, i.e. the gradient caused by the magnetic tip on the cantilever. An MRFM experiment typically uses a magnet to create a uniform external field. The field at a particular point of the sample is therefore the sum of this field and the field created by the probe magnetic particle, as described in section 3.1.2. If one considers the situation in which

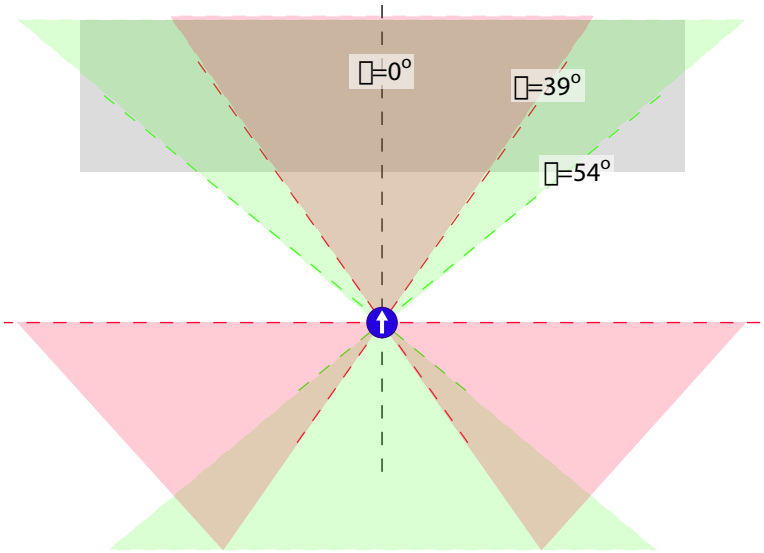

Figure 3.4: Interaction regions in an MRFM experiment. The pink regions show where the field gradient is negative and the green regions show where the tip field is positive. The pink and green lines show the boundaries between these regions (i.e. where the gradient and field respectively go to zero.)

the external field is swept, different portions of the sample experience different values of the tip field, so they will see the resonance condition for different values of the applied external field.

Figure 3.3 shows the angular dependencies of the field B_z and its derivatives with respect to z and ρ. The change in the field as a function of angle means that at some parts of the sample, the probe field will be parallel to the main applied field (i.e., the z axis). These parts of the sample will come into resonance at applied fields lower than the resonant field for that species. Similarly, other parts of the sample will see a tip field anti-parallel to the z axis, so will not come into resonance until the external field is higher than the resonant value. The gradient sign also changes as a function of angle, so some parts of the sample will give a signal in phase with the modulation of the B_1 field, and others will give an out of phase signal. Figure 3.4 shows a sample above our probe magnetic particle, and the different colours show the angles within which the field will be above or below the external value, and the sign of the gradient.

Equation 3.11 above gives the tip field as a function of position. We can rearrange this to give an expression to describe the surface over which the z component of the

tip field is constant, which is given by

$$r_c = c(3\cos^2\theta - 1)^{(1/3)} \tag{3.16}$$

where r_c is the distance to the surface of constant field at an angle θ and c is constant for a particular value of the field. Due to the azimuthal symmetry, this two dimensional description, shown in figure 3.5 may be extended to three merely by rotating about the $\theta = 0$ axis. Note that there are in fact two different surfaces of constant field: one for a given positive B_z comprising the lobes centred on the $\hat{\mathbf{z}}$ axis and one for the corresponding negative value of B_z, centred on the $\hat{\boldsymbol{\rho}}$ axis.. The distinction is an important one for experiments that employ an external field as well as that produced by the probe magnet. In an experiment without an external field, sample volume elements on both of these constant field surfaces will interact with the cantilever as the two fields will be the same, if opposite in direction. With an externally applied field also present, however, then the magnitudes of the fields at the two surfaces will not be the same. If the z component of the field at the surface due to the magnet alone is B_{surf} and the external field is B_{ext} and in the z direction, then the total magnitude of B_z will be $B_{\text{ext}} - B_{\text{surf}}$ on the lobes centred on the $\hat{\boldsymbol{\rho}}$ axis, and $B_{\text{ext}} + B_{\text{surf}}$ on the lobes centred on the $\hat{\boldsymbol{z}}$ axis. Thus, in an interaction of the sample with the cantilever with the external field below the resonant field, it will be spins along the blue surface that will contribute. If, on the other hand, the external field is set higher than the resonant value, then the interaction will involve spins along the pink surface. These ideas are illustrated visually in the modelling shown in chapter 4.

The distance of the surface of constant field from the centre of the magnetic tip will of course depend on the chosen value of this field. Since the sample sees both the field from the tip and the applied uniform field, the position of the sensitive slice can be moved by altering either the relative position of tip and sample, or by varying the external applied field.

3.1.4 Spatial resolution

As a possible imaging technique, obviously the spatial resolution achievable with MRFM will be an important quantity. This section briefly describes the main issues affecting the spatial resolution. Consider a case where we have our probe magnet near a sample, as shown in figure 3.5. The surface of constant field shown, for a

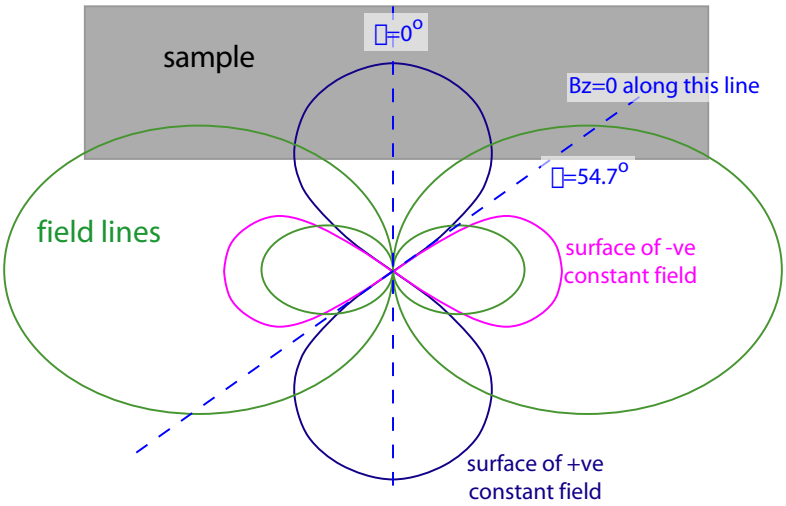

Figure 3.5: Blue line: Section through the surface of constant field (B_z) as a function of angle. The surface is symmetrical about the $\hat{\mathbf{z}}$ ($\theta = 0$) axis. The blue line is the surface of positive constant B_z and the pink line shows the surface of constant negative B_z, for a given vlue of B_z. The green lines show the shape of the field lines.

particular value of the external field, describes the location of the spins that will contribute to our signal. For a sample with a non-zero line-width (i.e., any real sample!) the interaction will in fact take place over a finite volume. The resolution in a given direction will of course be related to the line-width of the sample and the field gradient generated in that direction:

$$\Delta x_i = \Delta B / \frac{\partial B_z}{\partial x_i} \tag{3.17}$$

where x_i denotes the axis of interest. The symmetry about the z axis means that we only need to consider the resolution in two directions, along $\hat{\mathbf{z}}$ and $\hat{\boldsymbol{\rho}}$, the expressions for which have been presented in equations 3.13 and 3.14. At values of θ close to zero (ie, the portion of the sample right above the magnetic particle) the shape of the resonant slice of interaction is approaching flat. This means that the gradient in the z direction will be at a maximum, but that in the lateral directions will be at a minimum, in fact, zero. This can be seen in figure 3.3. A zero gradient in the $\hat{\boldsymbol{\rho}}$ direction would indicate an undefined resolution, but an effective resolution could be obtained from the curvature of the constant field surface.

3.1.5 Spatial information recovery

If one carried out an MRFM imaging experiment by simply recording the force on a magnetic tip while scanning a sample and applying appropriate fields (i.e., obtaining a "force map"), the result would not be a good representation of the spin distribution in the sample. This is because, as outlined above, the magnetic tip generally interacts with a distributed volume of the sample rather than a single point. To produce a meaningful image, the spin distribution would have to be extracted from the force map. If a force map was obtained with a constant field, then the profile of the surface of constant field would remain the same throughout the experiment. Assuming a sample containing just one cluster of spins, then the resulting force map would simply be a circle, with a signal recorded just when the surface of appropriate field intersected the position of the spins. In such a simple case, it would be easy to ascertain the lateral position of the spins. This is not the general case, however, as the force map obtained is the convolution of the distribution of spins in the sample with the spatial response of the probe. In reference [12] Zuger and Rugar use a technique called inverse filtering. For a sample with a spin density function $N(x, y, z)$ the magnetic force $F_z(x, y, z)$ for a magnetic tip located at (x, y, z) can be expressed by [12]

$$F_z(x, y, z) = \int\int\int N(x', y', z')h(x - x', y - y', z - z')\mathrm{d}x'\mathrm{d}y'\mathrm{d}z' \tag{3.18}$$

where $h(x, y, z)$ gives the force response for a point-like sample. If the field due to the probe magnet on the cantilever tip is known, then $h(x, y, z)$ can be calculated. If $F_z(x, y, z)$ is measured, then deconvolution can lead to the recovery of $N(x, y, z)$. This technique has been used to produce spatial images [12, 14]. Because the probe magnetic field will penetrate the surface of a sample, three dimensional imaging is possible.

3.1.6 Optimal scanning parameters

Now that we have established the behaviour of the $\hat{\mathbf{z}}$ field and gradient due to our probe magnet, we can move on to consider possible real experimental situations. In the above discussions, a point magnetic moment was assumed which obviously cannot be achieved in reality. However, the field and gradient created by a uniformly magnetised sphere are the same as those due to a point dipole of appropriate magnitude

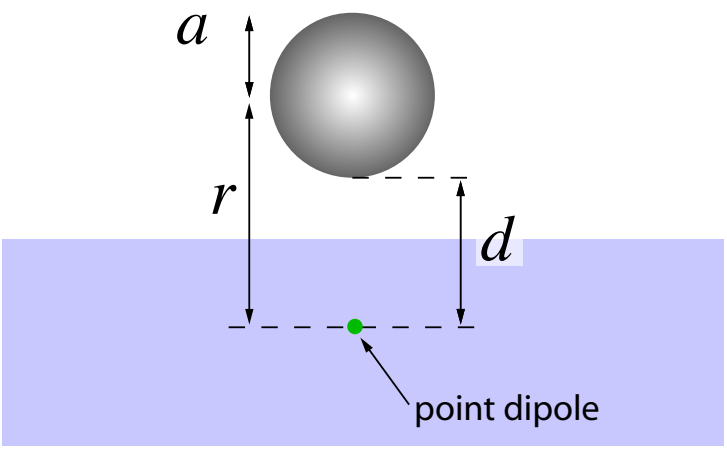

Figure 3.6: Simple example of a probe magnet radius a at a distance d from a point dipole.

located at the centre, so we can make some useful observations by considering the situation shown in figure 3.6 where we have a probe magnet consisting of a sphere of magnetisation $\mathbf{M}$, along the $\hat{\mathbf{z}}$ direction. The magnet radius is a and the distance between the sphere centre and a sample point dipole $\boldsymbol{\mu}$ is r. The magnet surface is therefore $r - a = d$ from the sample dipole. For a given saturation magnetisation, M_{sat}, of the probe magnet (in an external field of the order of 3T it is a reasonable assumption that the probe magnetisation will be saturated) then the probe moment will obviously be equal to $M_{\text{sat}}V$ where V is the volume of the probe magnet, $V = (4/3)\pi a^3$. From figure 3.3 it can be seen that the largest gradient due to the magnetic particle on the cantilever will occur either directly above or below, i.e. $\theta = 0°$ or $\theta = 180°$. For either of these, the magnitude of the gradient at the sample dipole due to the particle illustrated in figure 3.6 may be expressed as

$$\frac{\partial B_z}{\partial Z} = 2\mu_0 M \frac{a^3}{(a+d)^4} \tag{3.19}$$

There will be a trade-off between the larger moment of a bigger probe magnet and the larger distance its centre will be from the sample spin. It is easy to show from the above that for a given scan distance (i.e. for a given d) that the maximum sensitivity to a point dipole will be achieved when $a = 3d$. The sensitivity issue becomes less straightforward when the interaction is with a non-point-like dipole as discussed later in this chapter.

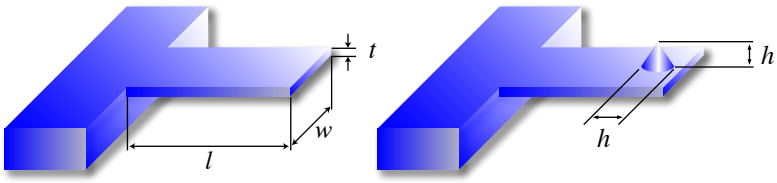

(a) Plain beam (b) Beam with conical tip

Figure 3.7: Simple clamped beam cantilever geometry showing dimensions. (a) No tip and (b) conical tip, after reference [56].

3.2 Cantilevers

Now that we have generated a force between the dipole moment of our sample and our probe moment, we need a way of detecting it, and for this we have chosen to use microfabricated cantilevers. These sensors are widely used in both AFM and a large number of related techniques. This section will provide an overview of cantilever properties and how they depend on geometry and ambient conditions.

3.2.1 Cantilever parameters

The parameters of a cantilever may be calculated from their known properties. In the simplest case, a cantilever may be considered to be a beam, clamped at one end, with length l, thickness t, width w and made from a material with density ρ and Young's modulus E, as shown in figure 3.7. Figure 3.7 (a) shows a plain clamped beam geometry. The resonant frequency of the lowest order flexural mode is given by [57]:

$$\omega_{r_1} = 3.516 \frac{t}{l^2} \sqrt{\frac{E}{12\rho}} \tag{3.20}$$

while the frequencies of some higher order modes are given by [58]:

$$\omega_{r_2} = 6.267\omega_{r_1} \tag{3.21}$$

$$\omega_{r_3} = 17.548\omega_{r_1} \tag{3.22}$$

$$\omega_{r_4} = 34.387\omega_{r_1} \tag{3.23}$$

It is important to note that the overtones *are not harmonics* of the lowest order mode. In the experimental work, it was the lowest order mode (ie ω_{r_1}) which was used, although the first overtone was occasionally observed in the preliminary characterisation measurements. The cantilever response to a given force is determined by its effective *force constant*. For the cantilever under our consideration, this can be expressed as [57]:

$$k = 1.03\frac{1}{4}\frac{Ewt^3}{l^3} \tag{3.24}$$

in units of Nm^{-1} . k may also be expressed as a function of the motional mass of the cantilever [57]:

$$k = m_{eff}\omega_0^2 \tag{3.25}$$

where m_{eff}, the motional mass, is given by

$$m_{eff} = \frac{\rho lwt}{4} \tag{3.26}$$

Real SPM cantilevers tend to have tips on them (see figure 3.7 (b)). This requires a modification to be made to the resonant frequency equations. If we assume that the tip is a cone with both height and base diameter equal to h, then the corrected resonant frequency is given by [56]:

$$\omega_{tip} = 1.734\sqrt{\frac{Ewt^2}{\rho(\pi h^3 l^3 + 2.832wtl^4)}} \tag{3.27}$$

For some of our experiments, the "tip" will take the form of a piece of magnetic material we have attached to the end of the cantilever. If we assume that the tip is spherical with radius r_{tip} and made of a material of density ρ_{tip}, then the resonant frequency can be adapted from a form in [56] to:

$$\omega_{tip} = 1.734\sqrt{\frac{Ewt^2}{16\rho_{tip}\pi R_{tip}^3 l^3 + 2.832\rho_{tip}wtl^4}} \tag{3.28}$$

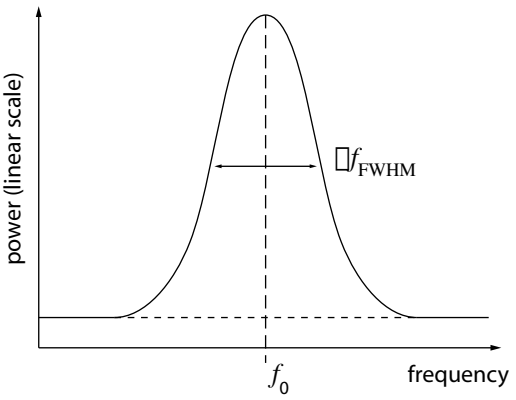

Figure 3.8: Vibration amplitude as a function of vibration frequency for an arbitrary oscillator to show how Q may be defined in terms of the width of the resonance at the points where the power is 3dB down on the peak value.

For example, a $450\mu m$ long silicon cantilever with a width of $50\mu m$ and a thickness of $2\mu m$ would be expected to have a resonant frequency of $f_0 = 13.6kHz$ with a $15\mu m$ tip lowering this frequency by about 400Hz. The force constant for such a cantilever would be around $0.19Nm^{-1}$. However, due to the strong dependence of resonant frequency on thickness, real cantilevers that nominally have the same dimensions may have significantly different resonant frequencies and force constants, for example, see section 6.1.

3.2.2 The quality factor and damping mechanisms

For our mechanical resonator, and indeed for almost any type of resonator, we can define the *quality* or Q factor, Q. This may be defined as 2π times the total energy stored in the resonator divided by the total losses from the resonator per cycle. Figure 3.8 shows how the Q may also be defined in terms of the bandwidth of the resonance:

$$Q = \frac{f_0}{\Delta f_{\mathrm{FWHM}}} \tag{3.29}$$

where Δf_{FWHM} is the full width of the resonance at the half maximum power. Thus, the higher the Q, the narrower the frequency response of the cantilever. A high Q factor is desirable as it simplifies the observation of small changes in resonant

frequency and enhances the response of the cantilever at resonance compared to the response off resonance.

It can be seen from the first definition given for Q factor that it will be limited by the various ways in that energy is lost from the cantilever. These mechanisms come from three sources, the effects of which can each be described with their own Q factor [59]:

A. The energy lost to the surrounding fluid (characterised by Q_f)
B. Energy coupled into a surrounding solid by the cantilever supports (characterised by Q_s)
C. Energy dissipated internally within the cantilever material (characterised by Q_i).

These various factors may be combined to relate to the overall Q factor by [60]:

$$\frac{1}{Q} = \frac{1}{Q_f} + \frac{1}{Q_s} + \frac{1}{Q_i} \tag{3.30}$$

It can thus be easily seen that the lowest of the three contributing Q factors will limit the overall Q. For vibration in an air-like fluid, Q_f is usually the limiting factor [60]:

$$Q_f < Q_s < Q_i \tag{3.31}$$

This project used commercial cantilevers over whose intrinsic properties we had no control, but the effect of damping by the air is very important. There are several distinct loss mechanisms and effects which will be briefly outlined here.

3.2.2.1 Molecular damping

This effect occurs at low pressures of between 1 and 100 Nm^{-2} [61]. The effect comes from collisions between individual molecules and the vibrating cantilever. The loss due to molecular damping is proportional to the gas pressure and damping effects will be exacerbated by close proximity to adjacent surfaces.

3.2.2.2 Viscous damping

For pressures above 100 Nm^{-2} the molecules can no longer be considered independent from each other, and the surrounding gas should be treated as a viscous fluid. This

results in two drag forces on the cantilever: a force proportional to the velocity of the cantilever surface, and another proportional to the cantilever acceleration. This first of these leads to energy loss from the resonator, and the second leads to a reduction in the resonant frequency [61]. A second effect due to viscosity comes from the creation of a boundary layer around the structure and the creation of a transverse wave due to the cantilever vibration. The size of these viscosity related effects will vary with pressure. At first the damping wil be mainly due to the drag forces and the energy loss by this mechanism will be pressure independent but a certain pressure, dependent on the cantilever shape, the boundary layer losses will dominate.

3.2.2.3 Squeezed film damping

This is an effect that occurs when the cantilever resonates very closely to a surface which is perpendicular to the direction of the cantilever motion, and results in losses due to a "pumping" effect as the air is squeezed from the gap between the surface and the cantilever, and then sucked back in [62]. As the frequency increases, however, a portion of the air will not have time to be sucked in and pushed out. This "trapped" air can act as a spring, leading to a (small) rise in the cantilever resonant frequency.

3.3 Introduction to force detection

Force detection methods work by measuring the ac or dc force acting on the detector, which is usually a very thin cantilever. A force can be gauged principally in two ways: by measuring the change in the dc deflection of the cantilever or by measuring changes in the vibrating (driven) cantilever's properties. In the most common force detection technique, AFM, 'contact mode' involves the former and 'non-contact' the latter. Both of these techniques may be implemented using the same method for detecting cantilever motion, of which there are a number of possibilities. This section looks briefly at two methods for detecting cantilever displacement with a more detailed discussion of fibre optic interferometry as the chosen technique for the work herein.

In the first AFM experiment, the cantilever deflection was measured by an STM tip [63], but the most commonly used methods are now optical. Many systems use laser beam deflection, which is shown in schematic form in figure 3.9. Light from a laser diode is reflected by the cantilever onto a detector, usually a quadrant photo-

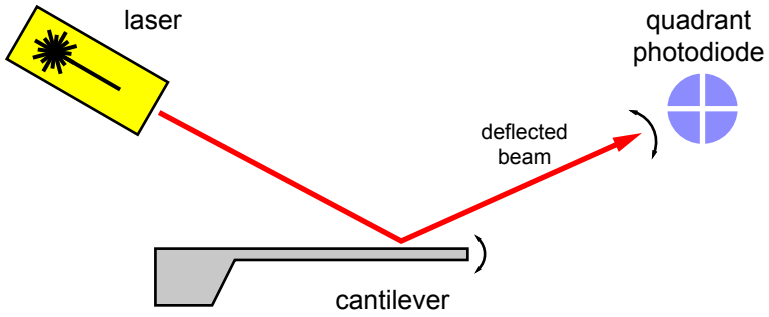

Figure 3.9: Optical lever detection system for measuring cantilever motion. Deflection of the cantilever results in a change in position of the reflected spot, which can be detected with, say, a quadrant photodiode.

diode. The signals from the four portions of the photo-diode are combined in such a way as to yield a signal proportional to the displacement of the laser spot, and thus relatable to the displacement of the reflecting element. This arrangement is popular as it requires a fairly simple optical system and is used in many commercial AFM systems. It has been used in MRFM experiments, see for example reference [23].

3.3.1 Fibre-optic interferometry

Another powerful method for detecting small amplitude displacements in SPM is optical interferometry, where light reflected from the force sensing element is combined with a reference signal and interference occurs. Such a system was used by Martin and colleagues for AFM measurements [64] and also applied to magnetic force microscopy experiments [65]. Their system involved using optics to propagate the laser beam to the cantilever. In 1988 Rugar outlined [66] an AFM system using a fibre-optic interferometer based on an earlier description by Drake and Leiner [67]. This system used a polarising beam splitter to direct the return signal onto a detector, requiring the control of the light polarisation. In 1989 Rugar and colleagues announced an improved system [68] using a fibre-optic directional coupler removing the need to worry about

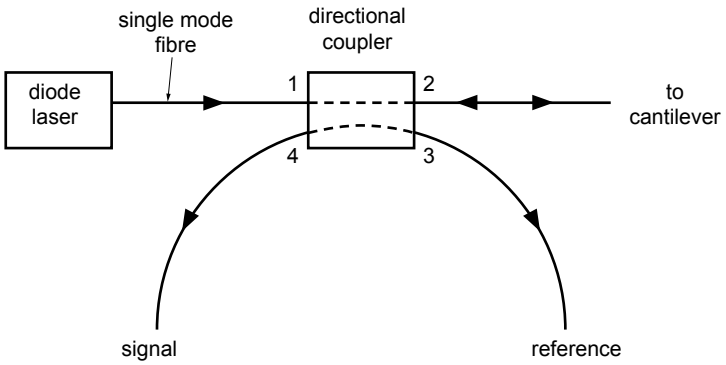

Figure 3.10: Single mode fibre-optic interferometer for AFM, adapted from [68].

polarisation. This design is shown in figure 3.10. The coupler is reasonably insensitive to polarisation. Light from the diode laser is split by the coupler and a portion travels down the sensing fibre. At the end, some is reflected back up from the air/glass interface, and a further portion is reflected back up from the cantilever.

This type of interferometer is based around the interference in an optical cavity formed by the cleaved fibre end and the reflecting surface of the cantilever which is illustrated in figure 3.11. If one monitors the intensity of the light reflected back up the fibre as the separation between the fibre end and cantilever is varied, a fringe pattern will be observed. Consider the situation where we have the fibre end reflection and cantilever reflection travelling back up the fibre. The component reflected from the fibre end will have the form $E_1 = A_1 \cos(kx - \omega t)$ and the component reflected from the cantilever is $E_2 = A_2 \cos(kx - \omega t + 4\pi d/\lambda)$ where $4\pi d/\lambda$ is the extra phase shift due to the double transit of the gap between fibre and cantilever. The intensity of the signal is the time average of the square of the total electric field, which is

$$I_{\text{sig}} = \frac{A_1^2}{2} + \frac{A_2^2}{2} + A_1 A_2 \cos \frac{4\pi d}{\lambda} \tag{3.32}$$

Thus, as a function of distance, the interferometer output is a sinusoid with a zero frequency offset. The values of the amplitudes A_1 and A_2 are going to depend on the incident light in the interferometer and the properties of the cantilever, but do not

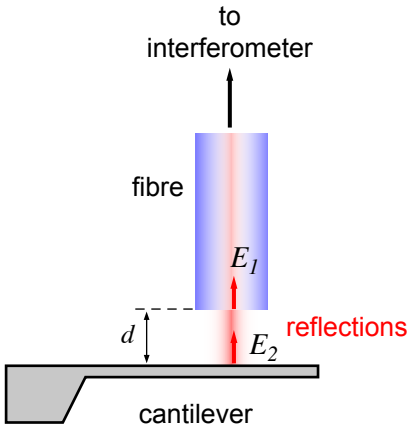

Figure 3.11: Glass → air interface and cantilever reflections for fibre-optic interferometric detection of cantilever motion.

need to be known as the interferometer sensitivity can be obtained from the maximum and minimum values of the output, as described in section 6.4. It is obvious that as the sensitivity to distance will be the derivative with respect to d, it will peak when the interferometer is midway between a fringe maximum and a minimum and that it will be zero at a maximum or minimum.

3.3.2 Finite coherence effects

Section 3.3.1 presumes that the source is single frequency, so, if we ignored the change in the coupling of the return field into the fibre, then the fringe pattern would go on forever. No real source, however, is single frequency and this means that the fringes will decay with increasing path difference (or, equivalently, time delay) between the two signals being combined in the interferometer. We can use Fourier methods to look at this decay.

A general expression for two beam interference cases is:

$$I_{sig} = I_1 + I_2 + 2\Re\langle E_1 E_2^* \rangle \tag{3.33}$$

with $\Re$ denoting the real part of the expression. A *correlation function* can be defined

as [69, 70]

$$\Gamma_{12}(\tau) = \langle E_1(t)E_2^*(t+\tau)\rangle \tag{3.34}$$

This function may be normalised in terms of the intensities:

$$\gamma_{12} = \frac{\Gamma_{12}(\tau)}{\sqrt{I_1 I_2}} \tag{3.35}$$

where γ_{12} is the complex *degree of coherence* of E_1 and E_2. The subscripts simply denote that we are referring to E_1 and E_2. For a point source where both fields come from the same point source, we would write instead Γ_{11}, the *autocorrelation function* and γ_{11}. In the case where the two intensities in the interferometer are the same, $|\gamma|$ yields the fringe visibility, which is 1 at zero time (or path) difference and drops off as τ increases (for a source with a finite spectral width).

γ can be related to the power spectrum of the source by the inverse fourier transform:

$$\gamma(\tau) = \int_0^\infty S(\nu)e^{i2\pi\nu\tau}d\nu \tag{3.36}$$

so if we know the spectrum of our source, we can calculate what the behaviour of the interference pattern should be. The application of these ideas is explored in chapter 5.

The above equation will tell us how the fringes die off for a particular source given its (arbitrary) power spectrum. The path difference at which the fringes are no longer visible is called the *coherence length*. For a source radiating uniformly over a bandwidth $\Delta\nu$ or $\Delta\lambda$ with nothing outside this range (a "top hat" function) the coherence length can be shown to be [71]:

$$\Delta_p = \frac{c}{\Delta\nu} = \frac{\lambda^2}{\Delta\lambda} \tag{3.37}$$

Although the spectrum of our source is much closer to being gaussian in profile, the above equation is still useful as a guide to coherence length without the necessity for carrying out the inverse fourier transform.

3.4 Noise and sensitivity

Fundamental to a discussion of the merits of any measurement system is the issue of sensitivity. This section examines the sources of noise in an MRFM experiment and how they limit the sensitivity of our detection. There are a number of noise sources that will contribute to the overall noise level, which will be looked at in turn.

3.4.1 Cantilever thermal noise

A significant, and in many cases limiting, source of noise is the thermal (Brownian) motion of the cantilever. This mechanical thermal noise is a straight forward analogue of Johnson noise in a resistor and is given by Nyquist's relation. For a mechanical resistance, R, the spectral density of the fluctuating noise force is [72]:

$$F = \sqrt{4k_B T R} \tag{3.38}$$

where k_B is Boltzmann's constant and T is the temperature. Being a spectral density, F has units of $\mathrm{NHz}^{-\frac{1}{2}}$. This may be related to the Q of the oscillator, since

$$Q = \frac{\omega_0 m_{eff}}{R} \tag{3.39}$$

where m_{eff} is the motional mass of the cantilever [57] and ω_0 is the resonant angular frequency of the cantilever. The force constant is related to m_{eff} by equation 3.25 and we may write [73]

$$F = \sqrt{\frac{4k_b T k}{\omega_0 Q}} \tag{3.40}$$

The thermal displacement noise at cantilever resonance is obtained by dividing by the force constant and multiplying by the Q, giving the mean square displacement for a measurement bandwidth b as [73]

$$\langle (\Delta x)^2 \rangle_{th} = \frac{4k_b T Q b}{k\omega_0} \tag{3.41}$$

3.4.2 Interferometer noise

The noise contribution calculated above is due just to the thermal motion of the cantilever. There will also arise noise in the interferometer system. For the purposes of the analysis, it is assumed that all the photons reflected by the cantilever are detected and that the fringe visibility is one. This would result in the interferometer output taking the form shown below [57]

$$P_{det} = P(1 - \cos\phi) \tag{3.42}$$

where ϕ, the phase of the interferometer is simply $4\pi d/\lambda$. We can relate fluctuations in P to fluctuations in d by [74]

$$\delta P = P \sin\phi \frac{4\pi}{\lambda} \delta d \tag{3.43}$$

Each photon reflected by the cantilever will transfer $2h/\lambda$ momentum to the cantilever, where λ is the wavelength of the light, so fluctuations in the photon pressure on the cantilever will lead to a fluctuating back action force on the cantilever. Together with the shot noise at the photodiode, this leads to a displacement noise that can be described by [73]

$$\langle(\Delta x)^2\rangle_{int} = \langle(\Delta x)^2\rangle_{back} + \langle(\Delta x)^2\rangle_{shot} \tag{3.44}$$

where $\langle(\Delta x)^2\rangle_{back}$ is the term due to fluctuations in the back action force and $\langle(\Delta x)^2\rangle_{shot}$ is the term due to shot noise in the detector. The fluctuations in the back action force are given by [73]

$$\langle(\Delta F)^2\rangle_{back} = \frac{8Phb}{c\lambda} \tag{3.45}$$

where P is the light power at the lever and b is the measurement bandwidth. At cantilever resonance, this leads to

$$\langle(\Delta x)^2\rangle_{back} = \frac{8Phb}{c\lambda}\frac{Q^2}{k} \tag{3.46}$$

For the off resonance case (ie, far away from ω_0), $\langle(\Delta x)^2\rangle_{back}$ is reduced by a factor of Q^2. Shot noise in the detector arises as a consequence of the discrete nature of the

light quanta. The number of photons per unit time at the detector, N, is given by

$$N = \frac{P_{det}}{h\nu} \tag{3.47}$$

where ν is the frequency of the light. Thus, N can be expressed in terms of the interferometer phase [74]:

$$N = \frac{P}{h\nu}(a\cos\phi) \tag{3.48}$$

The mean square fluctuation $\langle(\Delta N)^2\rangle$ in bandwidth b is given by the shot noise formula as:

$$\langle(\Delta N)^2\rangle = 2Nb \tag{3.49}$$

The shot noise variation in N will cause an apparent mean square displacement which can be arrived at by combining the above expression with equation 3.43 to yield [73]:

$$\langle(\Delta x)^2\rangle_{shot} = \frac{hc\lambda b}{16\pi^2 P\cos^2(\phi/2)} \tag{3.50}$$

which can be seen to depend on the interferometer phase. The maximum interferometer sensitivity to displacement is achieved when operating it in quadrature, i.e. with $\Delta\phi = \pi/2$, so the above expression simplifies to:

$$\langle(\Delta x)^2\rangle_{shot} = \frac{hc\lambda b}{8\pi^2 P} \tag{3.51}$$

It can be seen that $\langle(\Delta x)^2\rangle_{back}$ increases with interferometer power, P, while $\langle(\Delta x)^2\rangle_{shot}$ decreases with increasing P. Thus, there will be a value of P which minimises the sum of the two noise terms, which is given by [73]:

$$P_0 = \frac{kc\lambda}{8\pi Q} \tag{3.52}$$

For a Q in the thousands, the optimum power will be a few hundreds of microwatts, decreasing with increasing Q.

3.4.3 Comparison of cantilever thermal and interferometer noise

Of the three noise terms, $\langle(\Delta x)^2\rangle_{back}$, $\langle(\Delta x)^2\rangle_{shot}$ and $\langle(\Delta x)^2\rangle_{thermal}$, the thermal noise term is, within our likely experimental parameters, always going to dominate

significantly. For example, with a 13kHz cantilever with $k = 0.2\text{Nm}^{-1}$ and a Q of 10000, the thermal noise amplitude for a 1Hz bandwidth will be 1.0×10^{-10}m whereas the contributions for the back-action noise and detector shot noise, for an interferometer power of 200μW, will be 2.4×10^{-15}m and 4.4×10^{-15}m respectively. With a Q-factor of 10, which is around what one would expect at normal pressure, and at a temperature of 4K, the thermal noise amplitude of 7.1×10^{-13}m is still almost two orders of magnitude higher than the shot noise component, which is the larger of the other two noise components.

3.4.4 Maximising sensitivity

The previous section has discussed the noise mechanisms in an MRFM experiment and we now proceed to look at how we aim to maximise the sensitivity. Temperature is an important parameter in the sensitivity. The magnetisation of the sample (assuming it follows the Curie law) will be described as in equation 3.1. For small values of x, $\tanh x \approx x$, so at room temperature, the magnetisation M_0 is proportional to the reciprocal of the temperature. How far down this approximation holds depends on the fields being considered, but at a temperature of 10K at a field of 3T, the error is less than 2%. The force signal will scale with sample magnetisation, and thus will go as $1/t$. The thermal noise of the cantilever goes as $T^{1/2}$ as shown by equation 3.40, so for a given SNR, the minimum detectable signal force will also scale as $T^{1/2}$. Combined with the temperature dependence of the sample magnetisation, this means that the amplitude signal-to-noise ratio (ASNR) will scale as $T^{-3/2}$.

The cantilever Q affects the SNR. A higher Q will mean a larger response to both the signal force and to thermal fluctuations. However, the response to the former increases linearly with Q, whereas the latter goes as $Q^{1/2}$, giving the overall Q dependence of the ASNR as $Q^{1/2}$. A similar argument applies to the cantilever force constant: the response to the signal will go as k^{-1} but the noise force is proportional to $\sqrt{k}$ so the ASNR will go as $k^{-1/2}$. Thus for the optimal signal to noise ratio, we want to cool experiments and use soft (low force constant) cantilevers with high Q, so operating in a vacuum, in large magnetic fields. The above discussion uses the amplitude signal-to-noise ratio to aid explanation. The power signal-to-noise ratio, which is normally used, is the square of the amplitude ratio.

This discussion relates just to the cantilever and the sample, but the force on a test

dipole in the field of a probe magnet obviously depends on the gradient generated by the probe. However, in the case of an MRFM experiment, the test dipole is not an ideal point dipole, but a volume element of the sample. The size of the volume element dictates its moment. The flatness of the surface of constant field around $\theta = 0$ means that we can consider the sensitive slice as flat and with thickness $\Delta B / \frac{\partial B_z}{\partial z}$ (See section 3.1.4) so the slice thickness will decrease with increasing probe moment (i.e., increasing gradient). Thus, although a larger probe moment would mean that the interaction with a given number of spins would be larger, the number of spins in the sample that the probe field interacts with decreases at the same rate. In a first approximation, therefore, the signal to noise ratio will remain unchanged. This is why the smallest detectable number of spins is not an ideal measure of the sensitivity, as the concentration of spins in the sample will play a large part also. This idea is illustrated by modelling in chapter 4.

Chapter 4

Modelling simple FDMR experiments

The tip sample interaction in magnetic resonance force microscopy, discussed in detail in section 3.1, gives rise to interesting features, both spatial and spectral, due to the fact that different parts of the sample only interact when the total field they see fulfils the resonance condition. This chapter describes modelling of the tip sample interaction using a set of simple programs written in C. (See appendix A.) This work leads to a better understanding of some of the instrumental issues and also gives some understanding of the expected line-shapes.

4.1 Model implementation

This section describes the setup of the model used as a prelude to discussing its implementation. Due to the symmetry of the tip sample interaction, it is equivalent to consider scanning a probe magnet over a fixed sample, or scanning a sample over a fixed sensing tip. This simplifies the modelling process as it means that modelling the interaction of a fixed tip with a two dimensional fixed sample involves exactly the same calculations as working out the force map due to a point spin as the tip is scanned, allowing the same functions to be used to look at a variety of different problems. Although the model is nominally for ESR based interactions, the physics is exactly the same for NMR.

4.1.1 Assumptions and simplifications

The program makes a number of assumptions. The sample is assumed to contain unpaired electrons with $s = 1/2$ such that the magnetisation can be expressed as equation 3.1, reiterated below:

$$M_0 = \mu_s n \tanh\left[\frac{\mu_s B_z}{k_B T}\right] \tag{4.1}$$

The equations for the field and gradient due to the probe moment are given in spherical polar coordinates in section 3.1.2. However, it was thought difficult to construct a model of a square sample in spherical coordinates, so the equations were re-cast in cartesian coordinates to aid the modelling of force maps. If, like before, we take the probe magnet with moment $\mathbf{m}$ parallel to the $\hat{\mathbf{z}}$ axis and positioned at the origin then the z component of the field due to the moment is

$$B_z = \frac{\mu_0 m}{4\pi} \frac{2z^2 - x^2 - y^2}{(x^2 + y^2 + z^2)^{5/2}} \tag{4.2}$$

and the gradient of B_z in the $\hat{\mathbf{z}}$ direction is given by

$$\frac{\partial B_z}{\partial z} = \frac{3\mu_0 m}{4\pi} \frac{z(3x^2 + 3y^2 - 2z^2)}{(x^2 + y^2 + z^2)^{7/2}} \tag{4.3}$$

The assumption is made that if a certain field gradient and field value are calculated at a particular point, then those values may be regarded as constant throughout the chosen volume element centred at that point.

4.2 Static experiment emulation

The program works by considering a number of volume elements (which together make up the sample) in turn. For each volume element, the value of the field in the z direction due to the probe magnet ($B_{z_{\text{tip}}}$) is calculated and the external field is added to yield the total B_z at that element. The field gradient in the z direction is also calculated. The magnetisation of the element is calculated and used together with the calculated gradient to give the force on the probe magnet due to that volume element. The magnetisation is then recalculated, this time including the effect of an applied millimetre wave B_1 field. Taking the difference of the two calculations results in the

magnitude of the oscillating force on the cantilever due to the amplitude modulation of the illuminating field. This may be done for all the volume elements that make up the sample and the sum of the results is the oscillating force on the cantilever for the given value of the external field. If this is then repeated for a range of different field values, then the expected amplitude modulated force detected ESR spectra is obtained for 100% modulation of the B_1 field.

The frequency modulated case is less trivial to model, however. Calculating the magnitude of the force on the cantilever for two different frequencies of the B_1 field and taking the difference would effectively be modelling the case of a square wave frequency modulation, which is straightforward enough. In this situation, the frequency is only ever the two limiting values, limiting the regions that will interact with the cantilever and the fields at which an interaction will take place. The actual frequency modulation experiments, however, were done with a sine wave. In this case, the frequency of B_1 will pass between the two limiting values and at different times during the modulation cycle will take on different values. Thus, there will be an interaction at a wider range of fields. In order to model this, for each value of the external field, the magnetisations would have to be calculated for the range of frequencies covered. The peak interaction will not always be at the same point in the modulation cycle, so the point at which the maximum occurred would have to be established and taken into account as it will affect the relative phases of the contributions from different parts of an extended sample at a given value of the external field. This was decided to be too involved, so the square wave method was done as a simple approximation to see the line-shapes due to frequency modulation. The same effect may be obtained by using the AM model data and taking the derivative by calculating the difference in response from one field value to the next.

The program, which may be seen in appendix A sets a starting value of the external magnetic field. The contributions of each volume element in turn of a sheet of spins are then summed to give a sheet total before incrementing the z value and repeating, always adding the contributions to the previous sum. When the desired number of layers has been reached for a specific volume, the external field value is incremented, and the process repeated to create the spectrum. Initially carried out using a rectangular lateral cross section for the sample, this process was found to be more efficient for high resolutions when considering a cylindrical sample. For a square cross section with the origin in the centre, symmetry means that the result for the whole sheet may be found by calculating it for one quarter and multiplying by four. With a cylindri-

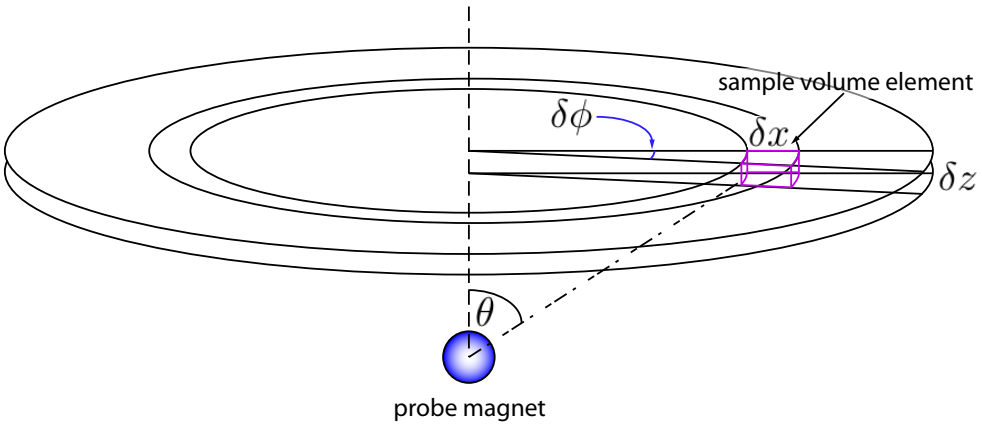

Figure 4.1: The geometry used to model the sample for the swept field model. A cylindrical sample proved easier to model to high resolutions than a cuboid sample.

cal sample, the interaction with an arbitrarily small angular slice may be calculated and multiplied appropriately to yield a result for the whole. This is illustrated in figure 4.1. The sample points are equally spaced along a radius of the sample. The resulting force per unit volume is then multiplied by the appropriate factor to give the force. The resolution issue is important as by the nature of an MRFM experiment, we are dealing with very high field gradients. This means that the interaction volume for a given geometry may be very small, so if it happens that there isn't a sample point located in the right place to interact at a given external field, then there will be no signal. Obviously this is only a general problem if the sample spacing of the model is larger than both the real paramagnetic centre spacing in the sample and the effective thickness of the resonant slice in the relevant direction.

The parameters used in the model were chosen to have reasonable values that were experimentally realisable. The exception to this was the amplitude of the B_1 field as this reduced the distortions present in the results due to the spatially quantised nature of our model sample. As can be seen in equation 3.3, the dip in magnetisation of the sample at resonance increases with B_1 (until saturation when $\delta M_z = M_0$). The width of the magnetisation dip also increases with B_1, so the spatial extent over which the change in millimetre wave power will affect the magnetisation is greater. This allowed larger pixel sizes to be used, reducing the computational intensity of the model. The relaxation times τ_1 and τ_2 were assigned the value of 5μs as the intention was to acquire a feel for the effects on the spectrum, rather than to simulate a specific experiment.

This is a very long relaxation time, similar to that for (fluoranthene)$_2$PF$_6$, a sample used in our experiments in chapters 7 and 8, and represents a favourable sample that is easy to saturate (see section 3.1.1). A probe magnet moment of 10^{-9}Am^2 was chosen. This is close to the value of the moment (8.3×10^{-10}) that a 10μm diameter particle with $\mu_0 M = 2T$ magnetisation, such as iron would have. The millimetre-wave frequency was 90GHz. The sample had a g value of 2.0023 giving a resonant field of $B_{\mathrm{res}} = 3.216$T.

4.2.1 Resonant slice sections

The model described above simply summed all the contributions together to give the force at a given value of the external field. There was, however, other information yielded in the calculations, and one thing worth examining was how the different parts of a spatially extended sample interact with the cantilever magnet. The sensitive slice is an important concept in MRFM, even if imaging is not the aim of the measurement, so it was thought an appropriate place to start. This was done with the same methodology as for modelling the swept field spectrum, but only the y and z coordinates of the sample were incremented and the interaction as a function of the sample position in the xy plane was placed into a 100×100 array to form an image of a vertical slice through the sample. This allowed the form of the sensitive slices to be modelled and also yielded information regarding resolution. Figure 4.2 shows the vertical cross sections of the sensitive slices in a sample 100μm across and 100μm thick. The probe magnet has been placed in the centre of the sample. This is, of course, a physically impossible situation, but it allows the whole resonant slice to be shown and illustrates the point well. The figure shows both the vertical lobes of interaction where the probe field adds to the external field and the horizontal lobes where the probe field subtracts from the external field. A larger value of field offset from resonance would bring the slices closer in to the probe magnet and a smaller offset would push them further out. At the resonance condition, the interaction would be along the line where $B_{\mathrm{tip}_z} = 0$. The scale is in arbitrary units, with black representing a negative force and white representing a positive force. Because the interaction falls off so fast with distance (as r^{-4}), the scale has been expanded to show values close to zero and clip off the extreme values, allowing the full shape of the sensitive slice to be shown. The reason that the negative and positive parts of the AM spectrum would appear to be inverted compared with figure 3.4 in chapter 3 is that if we take the

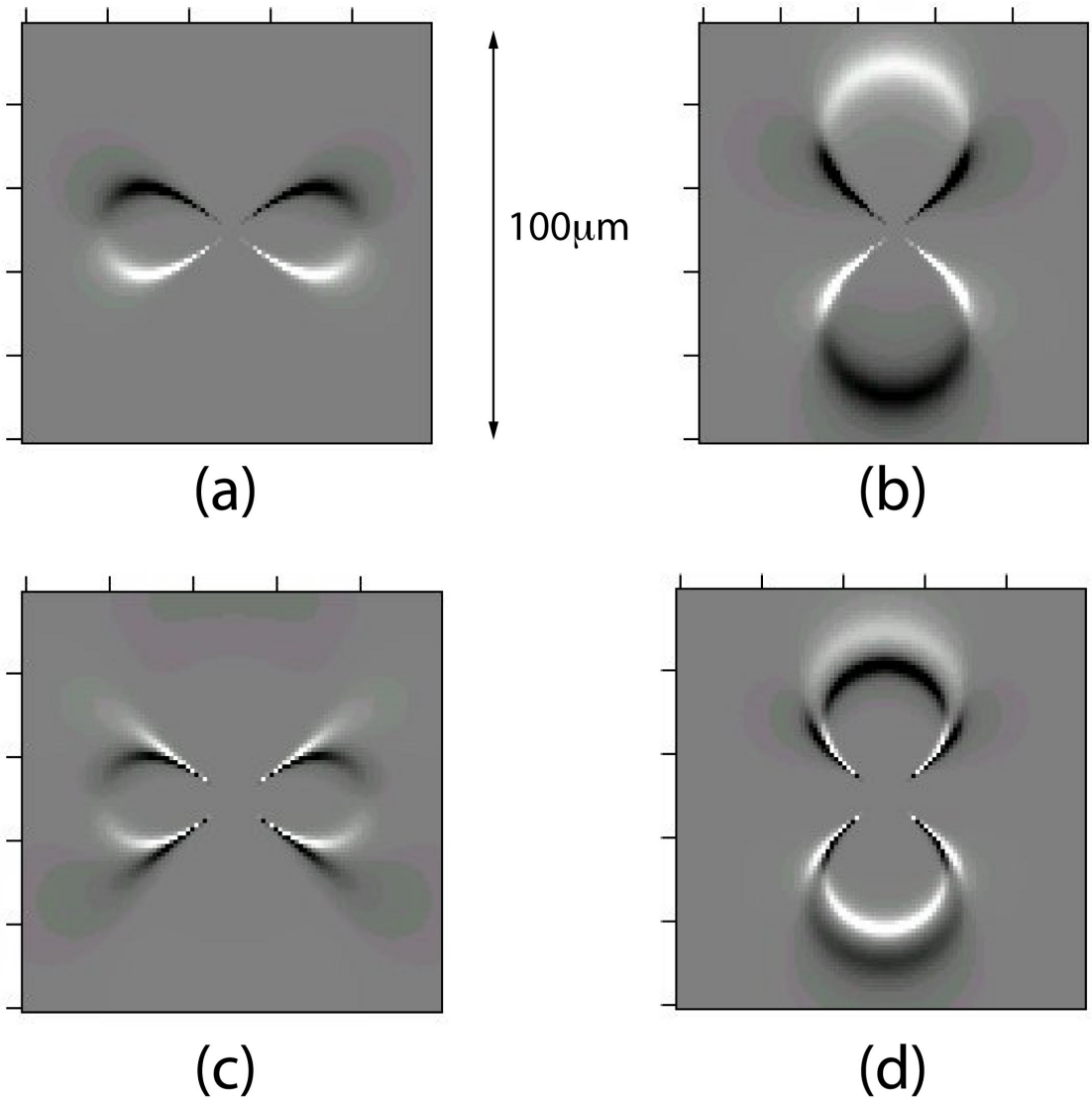

Figure 4.2: Amplitude and simplified frequency modulated model of resonant slice sections through a sample 100μm across by 100μm thick, with the probe magnet placed in the centre of the sample showing the surfaces of constant B_z. (a) External field set to $B_{\rm res} + 0.003$T AM (b) External field set to $B_{\rm res} - 0.003$T AM. (c) External field set to $B_{\rm res} + 0.003$T FM. (d) External field set to $B_{\rm res} - 0.003$T FM. The black areas represent a negative force and the white a positive force, with grey representing zero which is the value of the interaction throughout most of the sample. The scale has been expanded to show values close to zero.

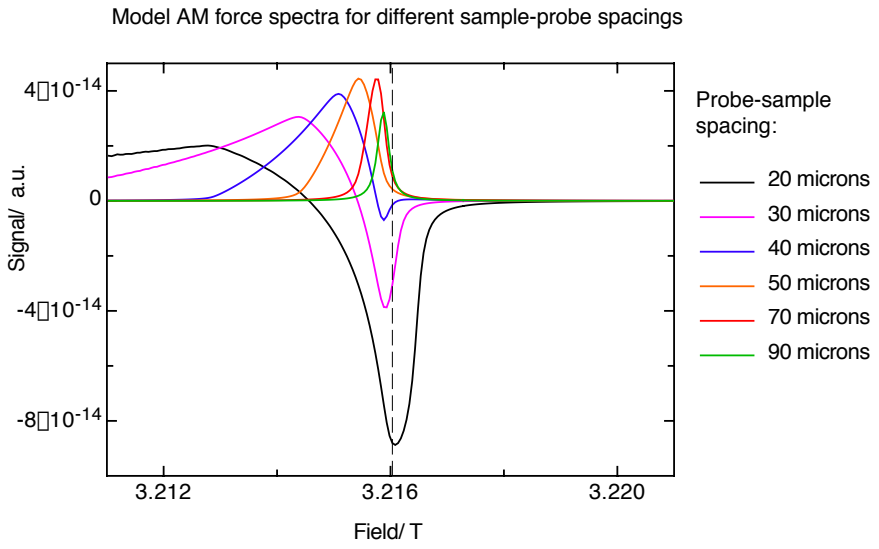

Figure 4.3: Model FDMR spectra with a 20μm thick cylindrical sample of 100μm diameter for a range of probe-sample separations showing the evolution in line-shape with increasing distance. The vertical dashed line shows the resonant field at 90GHz.

phase of our modulating signal as our reference, then the sample magnetisation will be in anti-phase to the modulation of the millimetre wave amplitude. This 180° phase change means that the interaction with a negative gradient will be in phase with the modulation. The FM pictures show the force due to the magnetisation difference, i.e. $M_z(\omega) - M_z(\omega')$ and the sign of $\omega - \omega'$ dictates the phase of the signal.

4.2.2 AM spectra and probe-sample separation

As is obvious from the discussion in chapter 3, the strength of interaction of a given sample volume element with the probe magnet depends a great deal on the bearing angle θ that the position vector, $\mathbf{r}$ of that element makes with the probe magnet axis. This immediately tells us that the signal we obtain from a given sample with a given probe may vary considerably depending on the exact configuration of the experiment. In this section, the AM force signal was modelled for the same sample and probe, with varying separations. Some of the observed trends are not very intuitive and the model provides a useful aid to getting a feel for what is happening.

The situation that was modelled was with a cylindrical sample of diameter 100μm and thickness 20μm. The sample spacing in both directions was 0.5μm, sufficiently

fine for a large B_1 field, in this case 10^{-4}T. The probe-sample separation was varied from 10 to 1000 microns to allow for a wide range in the value of the angle subtended by the sample at the probe. Figure 4.3 shows a selection of the spectra obtained for some of these separations. The shape of the force detected line changes dramatically as the probe is withdrawn from the sample. As expected, the line is much broader when the probe is close, due to the larger field gradient. A less obvious change is the presence of a large negative peak that gets smaller as the separation increases.

In figure 4.3, the dashed vertical line marks the expected position of the ESR signal given a g value of 2.0023. Thus, the signal before this point must be from regions of the sample where the probe field adds to the uniform field. The signal at fields higher than the resonant condition must be from portions of the sample where the probe field is in the opposite direction to the external field (see figure 3.4 in chapter 3). Similarly, the positive portions of the signal must be from portions of the sample within the 39° cone around the z axis, and the negative portions from the region outwith the 39° cone. The spectra for the larger sample-probe separations show only a single peak on the low side of the resonance as the entire sample is within both the 39° cone of the negative gradient and the 55° positive B_z cone. When the angle subtended by the sample is greater than 39° then the high field side negative peak begins to emerge, appearing first as a steepening of the high field side of the FDMR line. There will be no signal above the $B_0 = \omega/\gamma$ unless the half subtended angle is greater than 55°. When $B_{\text{ext}} = B_0$, then the interaction will be along the $\theta = 55°$ line. Note that although the B_z contribution from the probe magnet is zero at this point, the gradient is not, so this portion of the sample will still interact with the cantilever.

The above shows that the line-shape is strongly dependant on the experimental geometry. The same line-shape (after normalisation) may be obtained from different experiments, provided that the angles subtended by the sample remain constant and that the field at the sample due to the probe scales accordingly. Thus, if the dimensions of the sample and the sample-probe spacing are both doubled, then the same line-shape will result if the probe moment is increased by a factor of 8 ($= 2^3$).

For a given angle between the position vector of a magnetic moment and the axis of a second moment, the interaction scales as r^{-4}, so the FDMR signal may also be expected to have this strong separation dependence. However, this argument would only apply if the sample were a single point dipole. As it is distributed, the probe

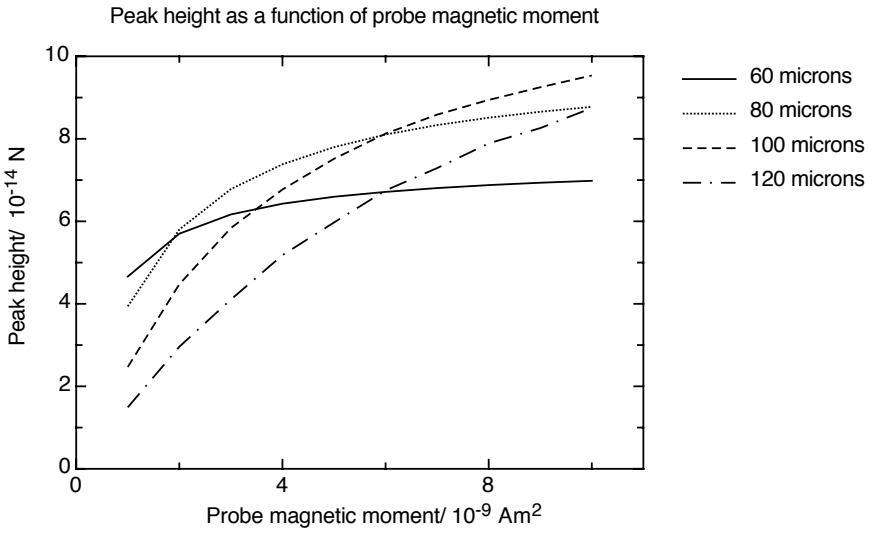

Figure 4.4: Height of positive peak as a function of probe magnetic moment for a range of probe-sample separations. The sample used in the model had a 100μm diameter and was 20μm thick.

magnet interacts with a certain volume depending on the field gradient strength at the point in the sample where the spins are in resonance. Although the interaction with one spin scales with the gradient, to a first approximation so does the reciprocal of the resonant slice width, suggesting no change in sensitivity as mentioned in section 3.4.4. As well as this, the interacting volume of the sample giving a positive signal will scale with the area of the surface within the 39.2° cone of the field gradient. These effects combine to give a situation where, for a certain range of probe-sample separations, the signal actually gets larger as the distance increases. This can be seen in figure 4.3 in the curves representing the 40μm, 50μm and70μm spacings; at larger separations the signal amplitude starts to fall off. As the spacing is increased, the sample becomes more point-like as far as the probe is concerned and the r^{-4} dependence is closely followed. Similarly, if the probe moment is increased, the signal size will also increase, but due to the thinner resonant slice, not in proportion with the increase in probe moment. This is illustrated in figure 4.4. Figure 4.4 shows the effect on the signal peak level of increasing the size of the probe magnetic moment, in which it can be seen that as the moment increases, the rate at which the peak grows decreases. For smaller probe-sample separations, the rate drops faster than for the larger separations. The signal will grow linearly with probe moment if the whole sample fits within a resonant slice, but not once the slice is too thin to accommodate the entire sample.

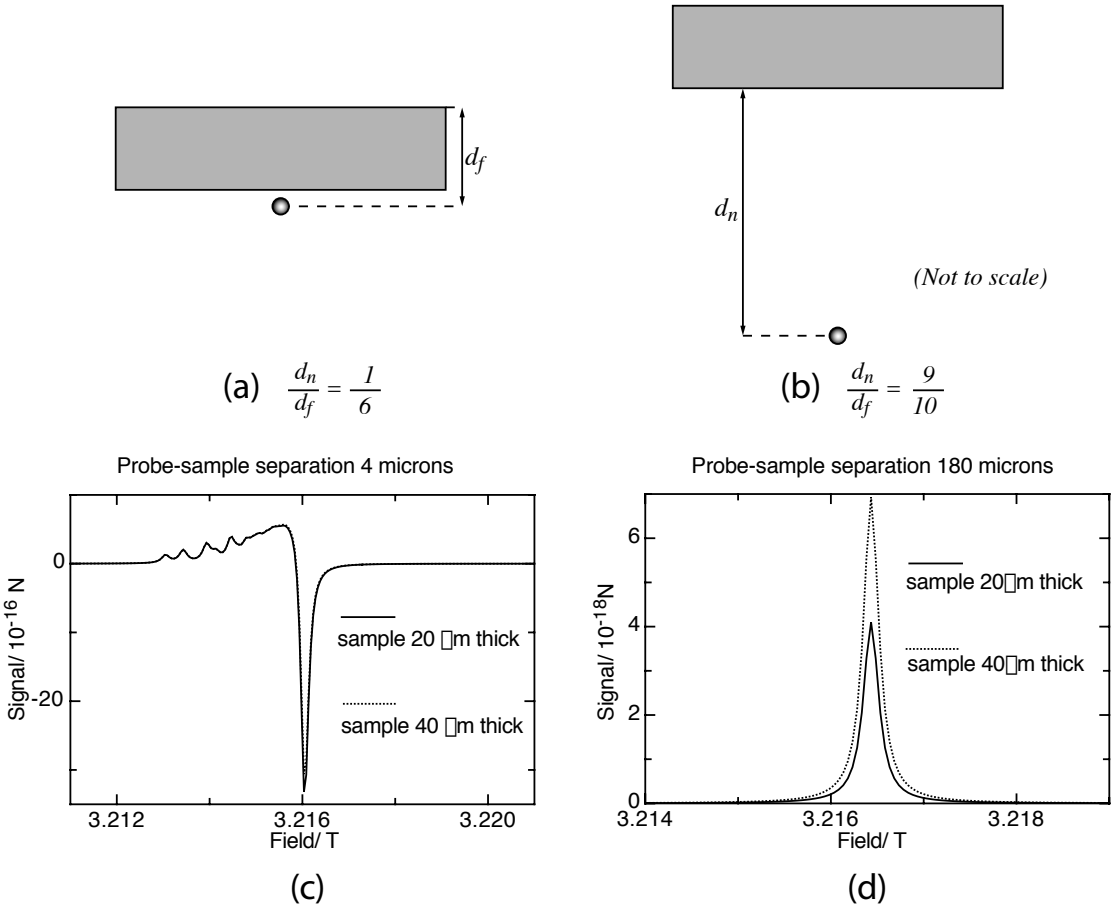

Figure 4.5: Two MRFM experiments with the same sample and probe magnet, but different values of the ratio of the distances between the probe and the near and far sides of the sample (d_n and d_f respectively). (a) shows $d_n/d_f = 1/6$ and (b) shows $d_n/d_f = 9/10$. (c) Model AM spectra for the situation shown in (a), showing the similarity in spectra for 20μm and 40μm sample thickness, with a probe-sample separation of 4μm and a probe moment of $10^{-12}\mathrm{Am}^2$. (d) Model AM spectra for a similar set-up with a probe-sample separation of 180μm.

During a swept field measurement, if the range of external field is large enough, then the entire sample will interact with the cantilever and contribute to the signal. In practice, however, the rapid fall off in signal with distance means that the influence that a given volume element of sample has on the final spectrum depends on the experiment geometry. One can imagine the situations shown in figure 4.5. The figure shows two MRFM experiments involving the same probe magnet and the same sample. In example (a), the proximity of the tip means that the gradient from the probe magnet at the near side of the sample will be 1296 times that at the far side, so the nearer spins will swamp the signal. In example (b), however, the sample magnet

distance is such that the interaction of the far spins will only be lower than that of the near by a factor of 1.4 as the sample thickness is small compared to the separation. The effects on the spectra can also be seen in figure 4.5. The two lines in each graph represent two different sample thicknesses, (c) showing the spectra from example (a) and (d) showing that from example (b). The doubling of sample thickness in the first example has negligible effect with the two lines overlaying, but a substantial effect on the second example. Obviously, for separations sufficiently large that the sample thickness is less than that of the resonant slice, then the signal will scale with sample thickness. The irregularities in the low-field side of the spectra in (c) are due to the spatial under-sampling of the model.

4.2.3 Multiple species samples and spectral resolution

The situations modelled above involve extended samples that are composed of a single type of spin. Of more relevance would be discussions of systems containing more than one type of spin. This would enable an evaluation to be made of the ability to resolve two species in the presence of the large gradients in MRFM. This was implemented by amending the swept field model to calculate the interaction with a second set of spins, at the same position as the first, but with a slightly different g factor. The contributions from the two sets were then added, making the total spin density in the sample double that of the single species model. Examples of the spectra produced by the two species model may be seen in figure 4.6 (a). This shows model FDMR spectra for a 20μm thick by 100μm diameter sample for a variety of probe-sample separations. The dimensions allow comparison with the spectra in figure 4.3. One set of spins has a g factor of 2.0023 as before and the other of 2.002. For the closest spacing, the line-shape is similar to that for the same spacing in figure 4.3 but there are visible distortions: the negative peak is broader in the two species example and has a visible bulge in the right hand side. These small differences are more easily resolved by taking the derivative. This is easily done numerically as in figure 4.6 and experimentally would be realised by an FM experiment. The slight bulge in the high field side of the negative peak in the AM spectra becomes two sharp peaks in the derivative spectrum.

As the separation increases, the positive peak can be seen to split into two. This is just visible in the 40μm case and quite obvious in the two larger separations. The positive peak due to the $g = 2.002$ spins is initially lower in amplitude as it coincides

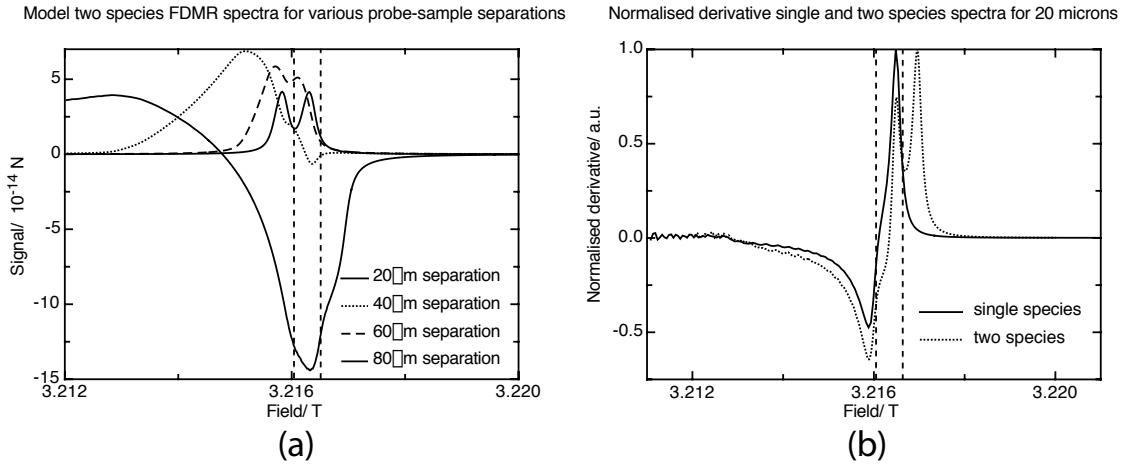

Figure 4.6: (a) Model AM FDMR spectra for a 20μm thick 100μm diameter cylindrical sample at a range of tip-sample distances for a sample containing two types of spin with g factors 2.0023 and 2.002. The vertical dashed lines show the positions of the resonant fields for each species. The relaxation times for the two species are the same. (b) Comparison between normalised derivatives of two species and single species model spectra.

with the negative peak of the $g = 2.0023$ spins, but as the separation increases and the field gradient due to the probe magnet decreases, the peaks may be seen to become equal in magnitude as is expected as there are equal numbers of spins for the two species. As the distance increased, the peak of the response would shift closer to the resonant field position.

The spectral resolution in FDMR experiments is likely to be limited by the field gradients employed, rather than the linewidths of the samples. Figure 4.7 shows the FWHM linewidths obtained in models of FDMR experiments featuring a 10μm thick sample with a diameter of (a) 10μm and (b) 100μm at a distance of 60μm from the probe magnet, as the size of the probe magnetic moment is increased. In both cases, when the probe moment is small, the minimum linewidth is set by the relaxation times and the magnitude of B_1 (10^{-4}T in this case), as given by equation 3.4. As the probe moment increases, the range of fields across the sample becomes bigger than the minimum linewidth and the measured linewidth increases linearly with the probe moment size. This behaviour is to be expected as the field gradient due to the probe magnet increases linearly with the magnitude of the moment. Also shown in the graphs is the difference in tip field between the near and far sides of the sample. This is closer to the linewidth measured from the model in (a) as the smaller lateral extent of the sample means that there is only appreciable variation in the tip field

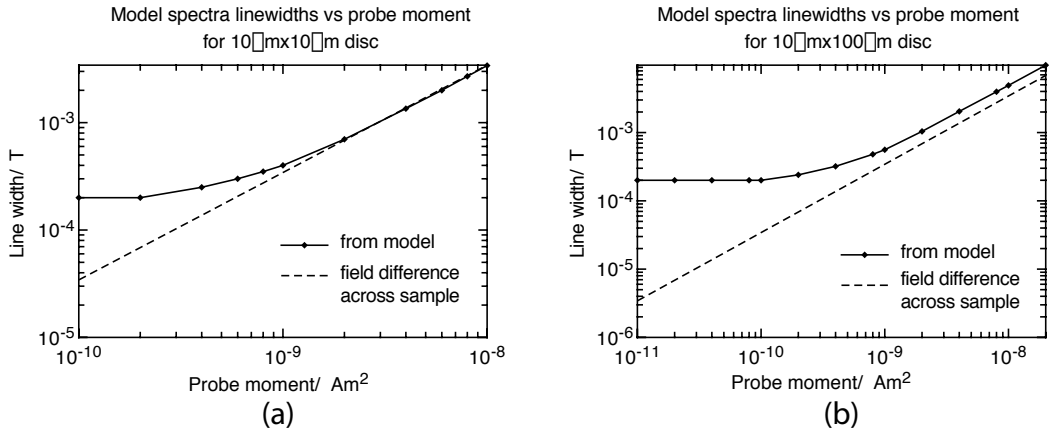

Figure 4.7: FDMR linewidths measured from model with 10μm thick sample and diameter of (a) 10μm and (b) 100μm along with calculated variation in field from front to back of sample.

through the thickness of the sample. The lateral variation of field in the geometry used in (b) means that one would expect larger linewidths, as indeed are shown. This simple relationship applies when the thickness of the sample is significantly less than the sample-probe separation. When these become comparable, the situation is less straightforward as illustrated in figure 4.5, but the linewidth will still be dependent on the field gradient.

4.3 Scanning experiment emulation

Looking at the signal resulting from a static sample in a static field yields useful information regarding the distortion of the line shape, but for a feel for the potential as an imaging technique, it is more useful to look at the results when scanning the probe relative to the sample (or, indeed, vice versa as both are equivalent). The procedure for looking at the force map generated by a point spin is the same as that for calculating the total force on a static probe due to a single sheet of spins. Instead of summing the contributions over the area of the sheet, values are recorded in a two-dimensional matrix. As for the static case, this is easily done for both amplitude and frequency modulation. A rectangular grid is better suited to this than the circular one used for the static experiments as we want the pixel size to be the same over the extent of the image. Resolution is not as important as any interesting features may

be examined closely by running the model for a smaller area. Because only a single image is being obtained the program will anyway be faster than for the bulk sample static experiment. The force map modelling was conducted with only one or a few spins as the contribution from each spin at each point of the scan had to be calculated separately. The model allowed the confirmation of the point spread function due to a point dipole. Figures 4.8 and 4.9 show model force maps when scanning at a height of 20μm in a $100\mu\text{m} \times 100\mu$m plane. The sample consists of two spins. The vertical position of the central one remains at zero and the spin in the lower right quadrant changes for each image, starting at zero in the (a) images and moving in 5μm steps to -15μm in the (d) images. The two figures show the same geometry, but figure 4.8 is for the amplitude modulated case and figure 4.9 is for the simplified frequency modulated case. Note that the shape of the force map is what would be yielded by taking the resonant slices shown in figure 4.2 and looking at the section obtained by slicing through them at a constant z value. Looking at figure 4.9 (d), note that the central spin interaction passes from negative to positive when moving along the radius from the centre, whereas the sign change along a radius from the second spin is in the opposite direction. This corresponds to the change of sign as a function of angle as shown in the vertical cross sections of the sensitive slice shown in figure 4.2.

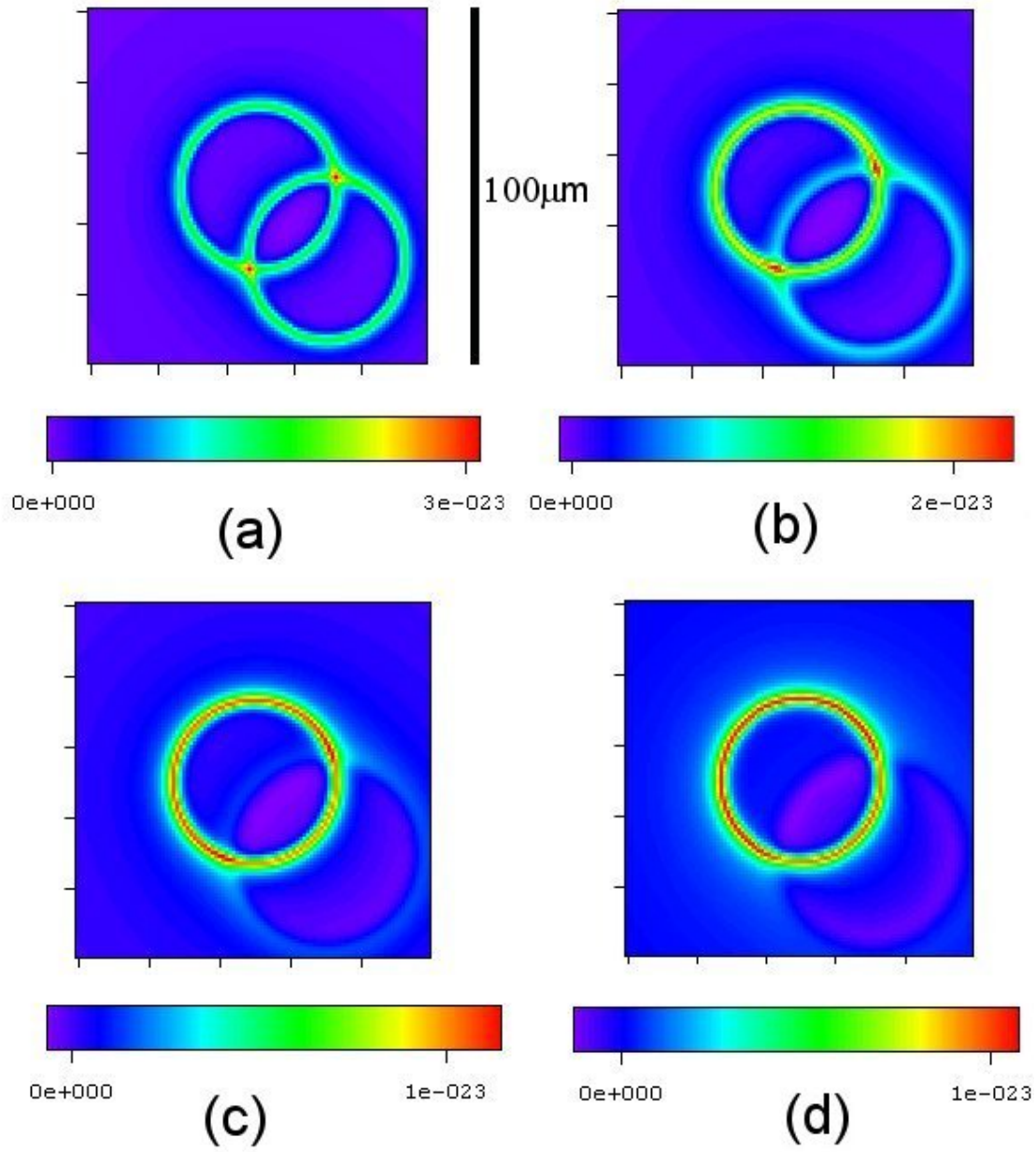

Figure 4.8: Model force maps for an AM experiment. The central spin position is the origin for all images and the second spin moves -5μm in the z direction for each image. The probe z position was 20μm for all images. The probe moment was 10^{-9}Am^2 and the B_1 field amplitude was 5×10^{-4}T to yield broad features. (a) Second spin at $z = 0$. (b) Second spin at $z = -5\mu$m. (c) Second spin at $z = -10\mu$m. (d) Second spin at $z = -15\mu$m. Note that the scales are in Newtons and scale from minimum to maximum in each image. The field offset from resonance was 10^{-3}T for (a) to (d).

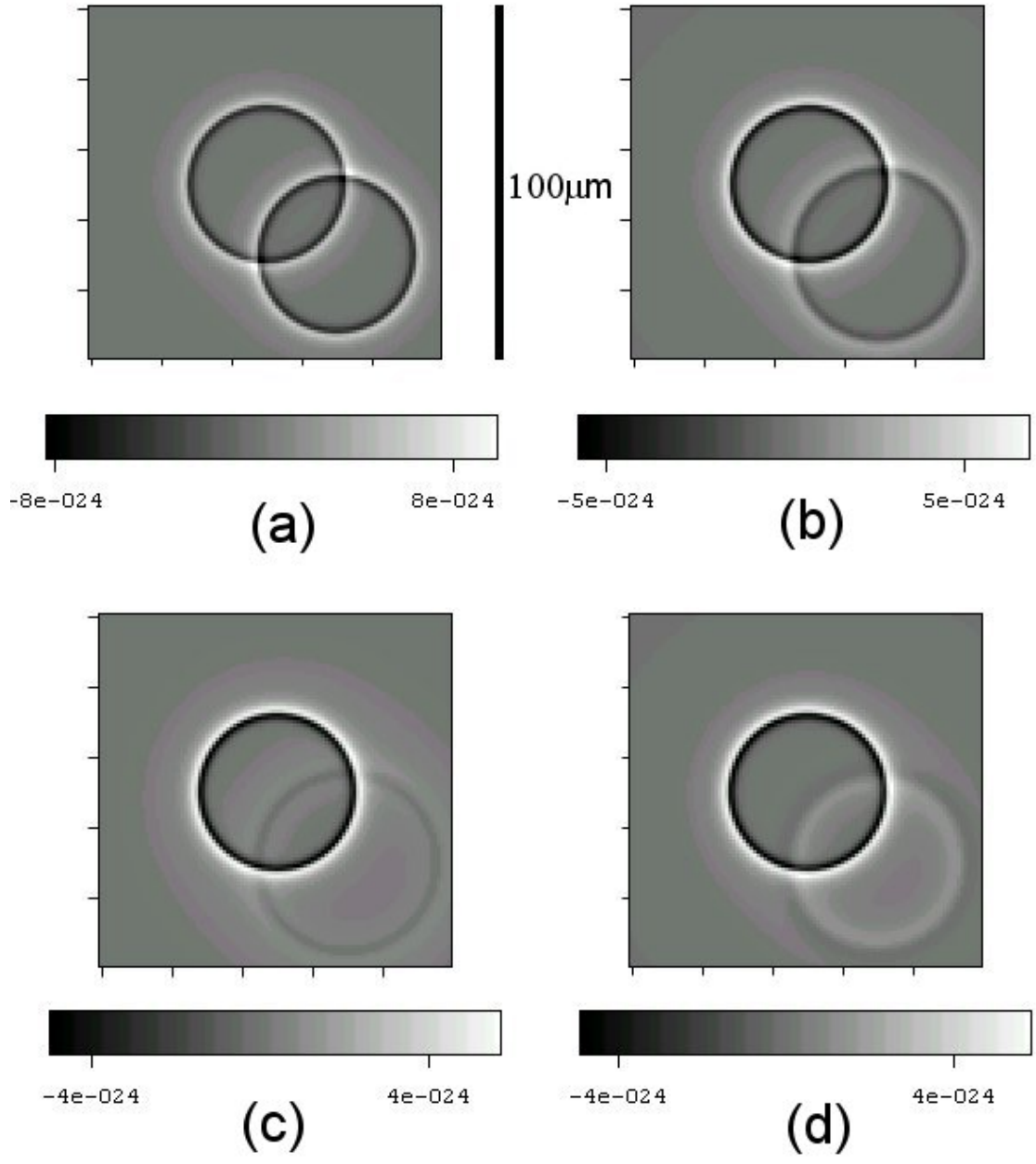

Figure 4.9: Model force maps for an FM experiment. The central spin position is the origin for all images and the second spin moves -5μm in the z direction for each image. The probe z position was 20μm for all the images. The probe moment was 10^{-9}Am^2 and the B_1 field amplitude was 5×10^{-4}T to yield broad features. (a) Second spin at $z = 0$. (b) Second spin at $z = -5\mu$m. (c) Second spin at $z = -10\mu$m. (d) Second spin at $z = -15\mu$m. Note that the scales are in Newtons and scale from minimum to maximum in each image. The field offset from resonance was 10^{-3}T for (a) to (d).

Chapter 5

Instrumentation I: Fibre optic interferometry

This chapter describes the fibre optic work carried out in the project, covering the design, implementation and characterisation of the fibre-optic interferometer. We will also look at the experimental implications of some of the ideas discussed in section 3.3.1. Various configurations have been used for the interferometer system, but the core components remain the same, and the more complex implementations of the system will be described later. Figure 5.1 shows the simplest version used. The light source, a superluminescent light emitting diode (SLED) is followed by an isolator before being connected to a directional coupler. The light then travels down the sensor fibre, and the reflected signal travels back up to the coupler, where it is split in two again. The component in the SLED arm is absorbed by the isolator and the other component impinges on a photodiode, whose output is then amplified. The various components are "pigtailed" with single mode optical fibres which are terminated in FC/APC connectors. These connectors have a ceramic ferrule with the fibre inside, the end of which is polished. The ferrule end is polished with an 8 degree angle, ensuring that there is minimum back reflection at each join. The use of pigtailed components greatly simplifies the construction and reconfiguration of the interferometer.

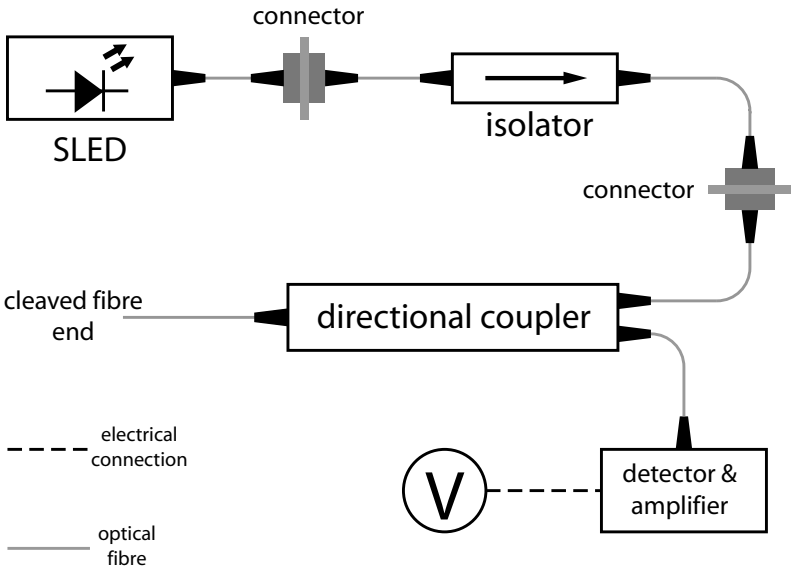

Figure 5.1: Simplest implementation of the fibre optic interferometer, using one 50:50 directional coupler and showing the connections between the fibre pigtailed components. The isolator is included to prevent back reflections in the system from upsetting the operation of the light source.

5.1 Light source

As mentioned above, the light source for the interferometer is a superluminescent LED, with a nominal operating wavelength of 1550nm[1]. A SLED was chosen over a laser diode as it has a much broader emission spectrum, and thus a shorter coherence length, than a laser (see the discussion in section 3.3.2). Our SLED has a bandwidth of around 50nm, leading to a coherence length of around 48μm. A short coherence length removes the possibility of stray reflections interfering with each other and causing slow drift as fibre lengths change due to thermal effects. The operating wavelength was influenced by the easy availability of optical fibre components at 1550nm due to its importance in the telecommunications industry as a low attenuation wavelength in optical fibres.

The SLED comes in a 14 pin package, and incorporates a small Peltier cooling element to enable temperature stabilisation of the diode, its output being temperature dependent, both in terms of power and centre wavelength. It also has a thermistor

[1]Opto Speed SA, Mezzovico, Switzerland

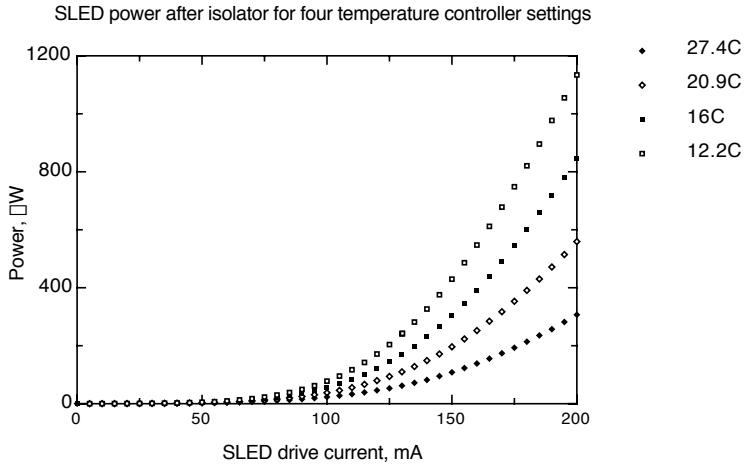

Figure 5.2: Graph of the SLED power (including isolator) as a function of the applied drive current. Data is shown for four different SLED temperature settings.

to enable sensing of the temperature. The diode drive current and temperature are controlled by separate current[2] and temperature[3] controllers. This section will go on to describe the characterisation of the SLED.

5.1.1 SLED power characterisation

The output power of the SLED was characterised as a function of both the drive current and the diode temperature. The power was measured using a Melles Griot power meter with a germanium sensing head suitable for IR measurements. The set-up for power measurements was fairly straightforward: the power meter head was mounted on an optical base plate and the fibre connector was positioned pointing at the detector. The angled connector required placing close to the detector to ensure that all the emerging light was caught. Figure 5.2 shows the SLED output as a function of drive current at a range of different temperature settings. The measurement was made with the isolator in place, and includes the small losses due to all the connectors. The graph shows that there is very little output until the drive current reaches around 80mA. At currents close to the 200mA maximum shown, the power is nearly linear with current. Also obvious from figure 5.2 is that the operating temperature of the SLED has a dramatic effect on the output power. This is shown more explicitly

[2]Newport model 505
[3]Profile TED 200

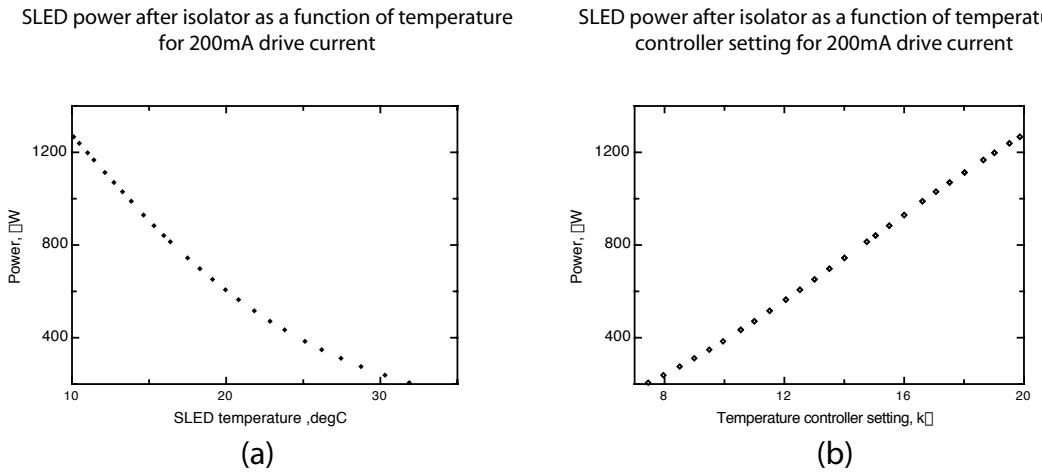

Figure 5.3: Graphs of the SLED output power (again including the isolator) as a function of (a) temperature and (b) temperature controller setting. These two graphs show the same data points, with the resistance values changed to temperature values for (a).

in figure 5.3 where the same power against temperature data is plotted twice. The temperature controller measures and displays the resistance of the thermistor incorporated into the SLED package, which is converted to absolute temperature by the equation

$$T = \left(\frac{1}{T_0} + \frac{\ln\left[\frac{R}{R(T_0)}\right]}{c} \right)^{-1} \tag{5.1}$$

where T is temperature in kelvin, $R(T_0)$ is the resistance at temperature T_0 and c is a constant of the thermistor. The temperature-power relationship is not obvious, but the power is almost linear with the resistance setting.

These power measurements were reasonably repeatable, although variations of up to $\pm 10\%$ were noted occasionally. These variations, however, are almost certainly the result of rotational mis-alignment of the connectors when two were being coupled together. The connectors have a locator on them to ensure correct position, but if this is moved even slightly, the two angled fibre ends will not butt correctly against each other, and losses will result. This problem may be minimised with care.

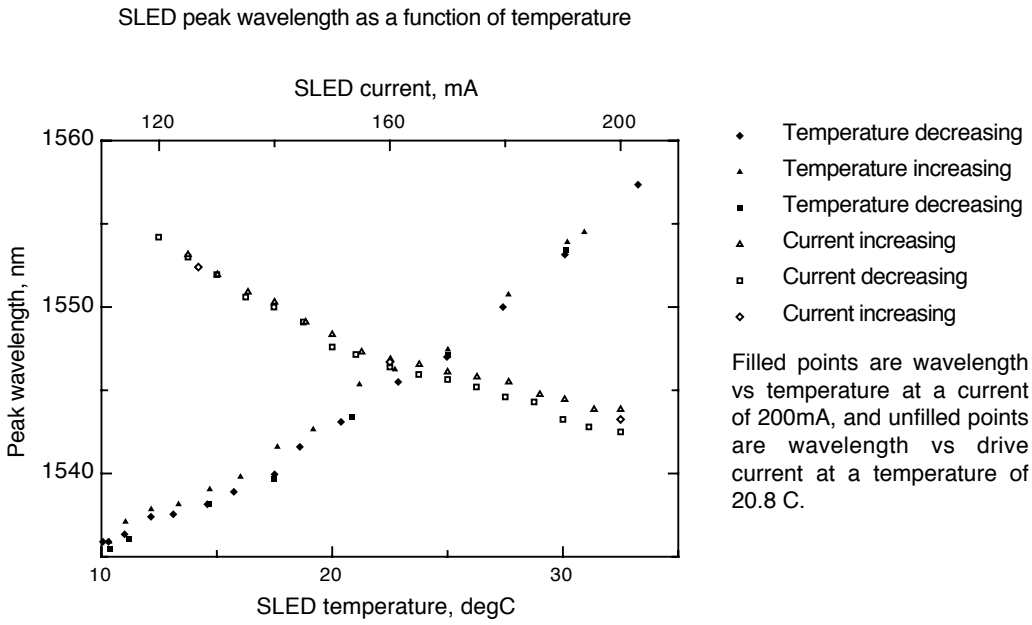

Figure 5.4: SLED peak wavelength as a function of temperature (filled points) and as a function of drive current (open points).

5.1.2 SLED spectral characterisation

The power characteristics of the SLED are an important part of its behaviour, but also very important is the spectral behaviour as the performance of the interferometer will hinge on it. As with the SLED power, the spectrum is also dependent on the drive current and operating temperature. Figure 5.4 shows how the peak wavelength of the SLED varies as a function of both the drive current and the thermistor temperature. This was measured using an optical spectrum analyser (OSA), a scanned-grating based device that measures power as a function of wavelength. Both measurements are disappointing in terms of repeatability: measurements were taken with the controlled variable moved in both directions to try and show up any possible hysteresis, but there is no obvious pattern. A possible cause of the spread is the relatively flat top to the measured spectra, an example of which is shown in figure 5.5. However, it is clearly visible that both the current and temperature have an effect on the centre wavelength, the 20nm wavelength shift being almost half of the bandwidth of the SLED.

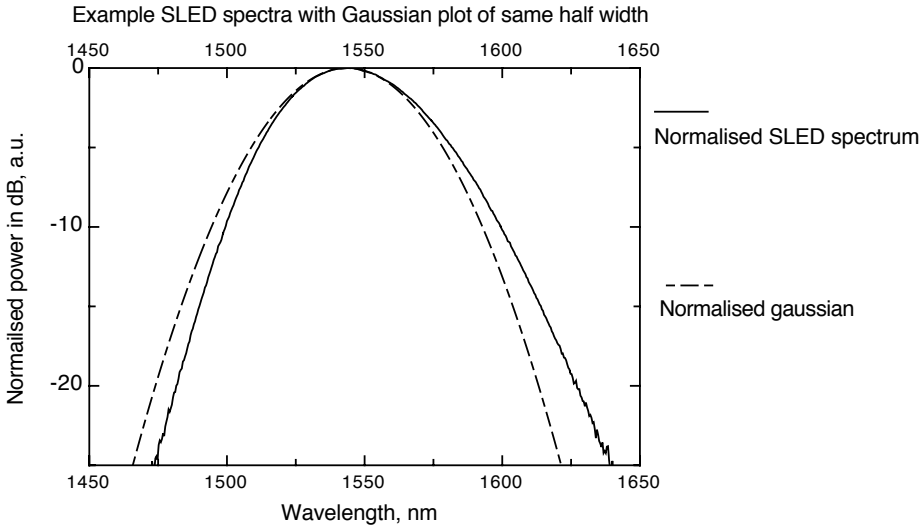

Figure 5.5: Example SLED spectrum plotted on the same axes as a gaussian line with the same full width at half maximum (-3db) of 54nm.

Figure 5.5 shows the SLED spectrum and a Gaussian distribution for comparison with the same peak wavelength and the same full width at half maximum (FWHM), in this case 54nm. The comparison shows that the spectrum is like a skewed Gaussian: it rises faster than the true Gaussian on the low wavelength (high frequency) side and tails off more gradually on the high wavelength side. The agreement with the Gaussian is, however, sufficient to make a Gaussian curve a reasonable first approximation to the real spectrum.

5.1.3 Model interferometer behaviour

The characterisation of the SLED enables the modelling of the interferometer signal as a function of the separation between the end of the sensor fibre and the object whose motion is being observed. This is a useful exercise as knowledge of the coherence length, while important, does not give us the full story for optimum interferometer set-up. The first part of the exercise uses the ideas in section 3.3.1 to obtain a sinusoidal function that would continue with the same amplitude forever as if the source had an infinite coherence length. The model is improved by multiplying by the magnitude of the degree of coherence, which is obtained by taking the inverse fourier transform

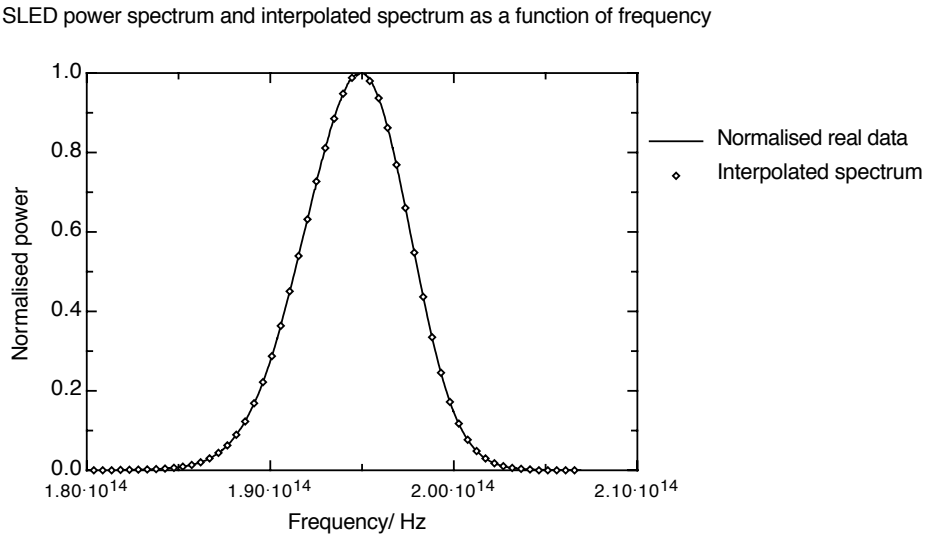

Figure 5.6: SLED spectrum in frequency terms, along with the interpolated points created by the thinning program. Note that the vertical scale is linear.

of the source spectrum. This was done using a C program employing the fast fourier transform (FFT) method.

Equation 3.36 requires that the power spectrum be a function of frequency, rather than wavelength. The FFT implementation employed [75] required that the data points entered be evenly spaced. Also required was that the input spectrum extended down to zero frequency which would result in a prohibitively large dataset if it were done at the same resolution as the spectrum was measured. A program was written to convert the SLED spectrum data to one in terms of frequency. The data was then re-sampled more coarsely by interpolating between real data points as since the measured data was taken in terms of evenly spaced wavelengths, the data point spacing varied as a function of frequency. The data was then padded out with further data points consisting of frequency points down to zero and beyond the original range to fill an array of 8192 values for submission to the FFT program which required the data set to contain an integral power of 2 values. The power values for these extra padding points were all set to zero. The quality of the fit is illustrated in figure 5.6, which shows a real SLED spectrum in terms of *frequency* (line) together with the interpolated points that make up part of the file that the FFT is performed upon. The output of the FFT function is the complex degree of coherence as a function of

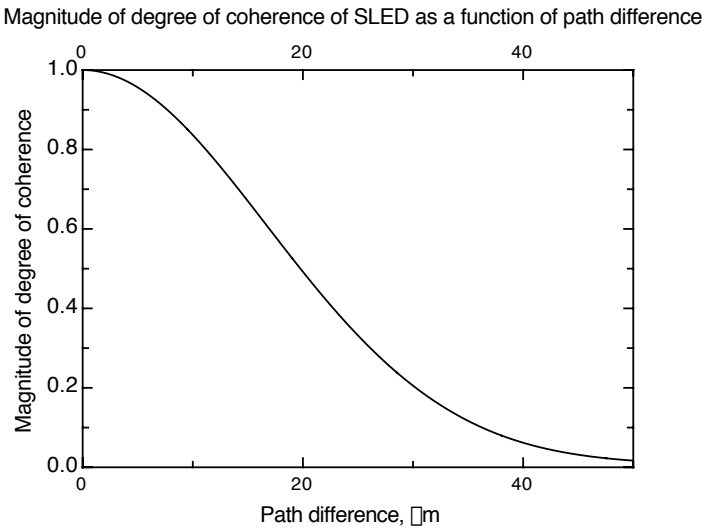

Figure 5.7: Magnitude of the degree of coherence, corresponding to the spectrum shown in figure 5.6.

time. This is converted to sets of real and imaginary components as a function of the path difference between the two interfering fields and the magnitude of the degree of coherence is calculated from the real and imaginary parts, before being normalised to peak at one at zero path difference. The result is shown in figure 5.7. This quantity is then used as a multiplier for the interference term of the interferometer ouput to show the effect of a finite coherence length on the interferogram. No account is taken of the change of coupling of the reflected light back into the fibre which would give rise to further decay of signal level as a function of distance. Note that the coherence length of around $50\mu m$ is the point at which the fringes are almost invisible (noting, of course, that the fibre cantilever separation is only *half* the path difference) so any desired operating distance will be well within this.

5.2 Directional couplers

The directional coupler forms the heart of the interferometer systems. Two kinds were used in the project: 50:50 couplers and 90:10 couplers. The combining element was usually a 50:50 coupler, although a variety of interferometer configurations were

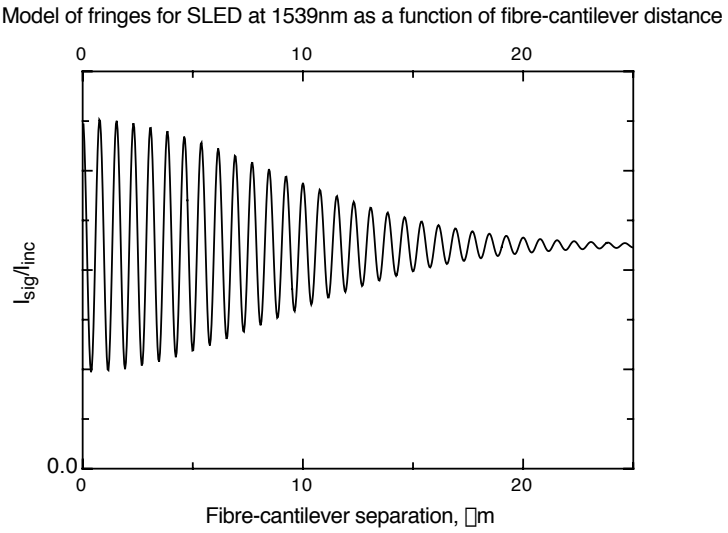

Figure 5.8: Model interferometer fringe pattern using the degree of coherence.

tried. Two different 50:50 couplers were used. The first was a 3 port device, with one input split equally between the two outputs, whereas the second was a four port device with two inputs and two outputs. The 90:10 couplers were three port devices and were usually used to allow a small amount of the light to be extracted for monitoring purposes. The output from the different arms of the 50:50 couplers were both around 40% of the input and the output from the 90% arm and 10% arm were 76% and 9% of the input respectively. Further interferometer development will use a fibre pigtailed circulator instead of a directional coupler to reduce the losses. This will be of particular benefit when using a fibre grating to increase coherence length as discussed in section 5.6.1.

5.3 Detection electronics

In order to detect the interferometer signal, photo-diodes were employed with a series of amplifiers. The main detection system was a 2 channel photo-diode amplifier, built in-house by the school's electronics workshop. The circuit diagram can be seen in figure 5.9. This had two optical inputs. Each photodiode was connected to an op-amp to pre-amplify the signals which were then split and sent to a pair of difference

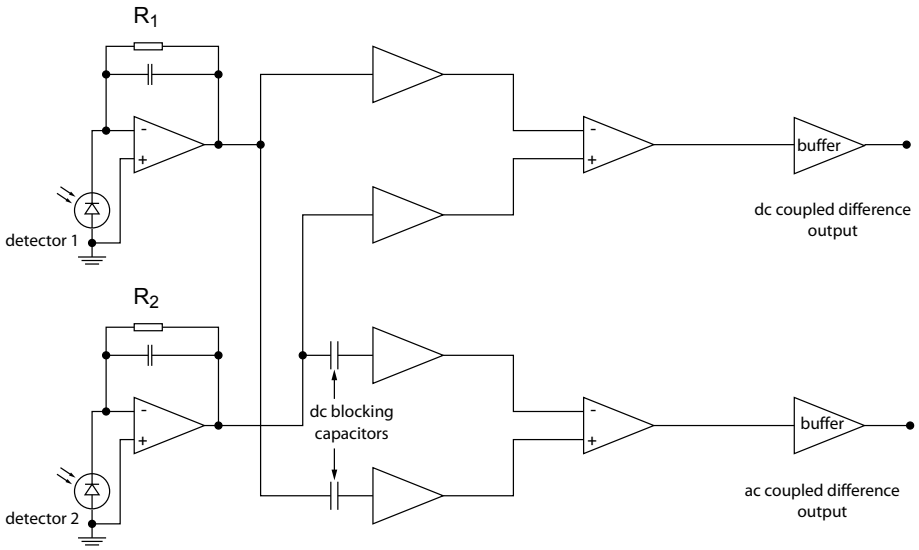

Figure 5.9: Simple block diagram for the two channel photodiode amplifier used to detect the interferometer signal.

amplifiers, one ac coupled and one dc coupled, before passing through buffers to the output. Thus, the outputs were the buffered amplified difference between the inputs, which can help to reduce the effects of amplitude noise on the SLED output on the interferometer signal if the second input is a portion of the SLED light coupled off before the interferometer [68]. When the input to the second channel was removed the system behaved just as a single channel system. Both ac and dc coupled outputs were available. The buffer stages were to allow the detector-amplifier system to drive a 50Ω load, such as a spectrum analsyer or oscilloscope. The gains of each amplifier channel were variable by potentiometer, but the initial gain for each photodiode is set by the resistors R_1 and R_2. The original variable resistors for controlling the dc channel gain were replaced by multi-turn potentiometers, the more accurate adjustment being necessary for using the gains along with a second input to set an offset level.

To approximately characterise the detector, the 50:50 coupler was used in conjunction with the same power meter used for the SLED and coupler characterisation. One arm of the splitter was connected to an input of the detector box, and the other arm led to the power meter. The output of the dc channel was measured at minimum gain as a function of the power read from the other arm of the splitter. The experiment was repeated with the two interferometer arms switched and the result averaged to give the output of the detector and amplifier system as a function of input power. The

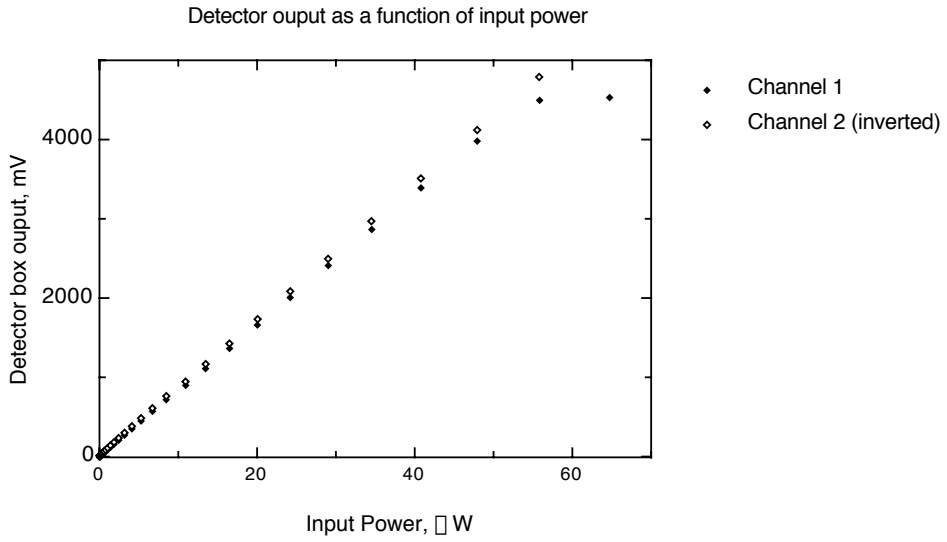

Figure 5.10: Graph of detector dc output as a function of input power for each channel. Note that the data for channel 2 has been inverted as this channel has negative gain. R_1 and R_2 are both $100k\Omega$.

results for both detector channels is shown in figure 5.10. Both channels show that the output is linear with input power, which is expected of the photodiodes. Note that both show output increasing with input, however, the output has been inverted for the channel 2 data due to the difference nature of the amplifier. The channel 1 signal can be seen to saturate above around 4 V. Channel two also saturates, but at around 6 volts. The data in figure 5.10 is for both R_1 and R_2 set to $100k\Omega$. Various values were used for these resistors, so the intention is to show that the output is linear within the range of the op-amp, not to make absolute power measurements. The signal power with only the reflection from the cleaved fibre end is on the order of a few micro-watts, rising to tens of micro-watts when there is a reflecting surface present at the end of the fibre.

5.4 Sensor fibre preparation

The optical fibres used operate in a single mode at 1550nm. The core diameter is $9\mu m$ and the cladding diameter is $125\mu m$.The fibre assembly consists of the fibre itself covered in a clear protective primary coating. This is in turn covered with a 0.8mm

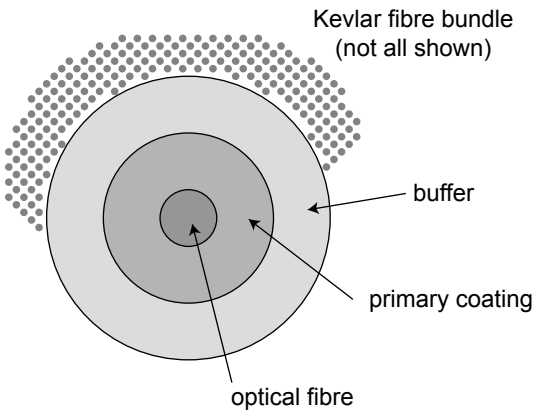

Figure 5.11: Protective layers around the optical fibre optical fibre (not to scale). The final sheath around the Kevlar fibres is not shown.

diameter plastic secondary coating, or buffer. The buffer is surrounded by a bundle of very fine Kevlar filaments to prevent physical damage to the fibre, which are in turn encased in a further plastic layer. The outer layer and Kevlar fibres are removed by cutting and the buffer may be removed carefully with a cutter or by immersion in a suitable solvent (for example methylene chloride) which also removes the soft primary coating.

Because our interfering cavity is formed by the fibre end and the cantilever, the cleave quality is important. A perfect fibre cleave, i.e. where the fibre is left with a flat end exactly perpendicular to the fibre axis, will reflect 4% of the light back up the fibre, assuming a refractive index of 1.5. To obtain high quality cleaves, a special fibre cleaver is used. Two different models were employed, but both worked in the same way: a blade was used to very lightly score the fibre, then a small amount of bending was enough to fracture the fibre. Cleaving was carried out with the fibre connected to the interferometer and the dc output of the interferometer being monitored, to allow the cleave quality to be assessed immediately.

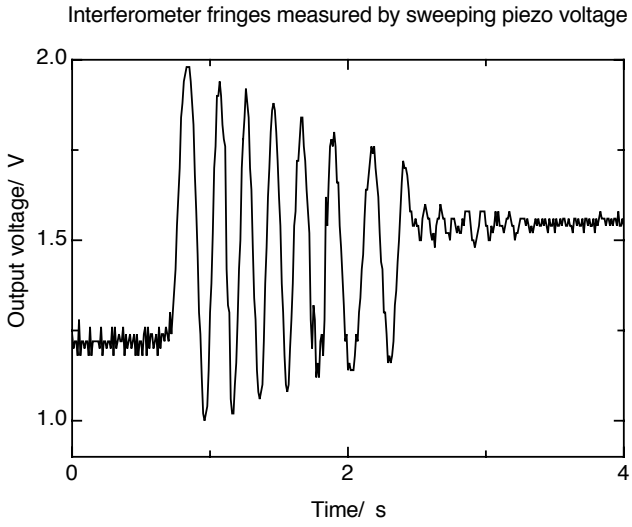

Figure 5.12: Interference fringes obtained by moving a piezo stack mounted reflector away from the cleaved fibre end. The voltage resolution is poor, but the fringes are clear, as is the decay with distance away, which is the result both of coupling loss due to distance and the low coherence of the SLED.

5.5 Interferometer testing

Most of the characterisation of the interferometer took place when using it to look at real cantilevers, but some simple work was done to verify that fringe patterns could be obtained. These were done by placing the fibre close to the end of a piezoelectric stack transducer, then recording the interferometer's dc coupled output using a digitising oscilloscope. An example trace is shown in figure 5.12. The control voltage was varied by hand, so the fringes may be uneven in width, but each fringe (maximum to the next maximum) represents a distance change of $\frac{\lambda}{2}$, ie 775nm, for a total movement of about 5.8 μm.

5.6 Interferometer improvement

The preceding sections describe the initial development of the fibre optic interferometer. During its subsequent use in real experiments (as opposed to characterisation) some limitations became apparent. These are described in this section, together with steps taken to improve the interferometer.

5.6.1 Increased coherence length

As described in section 5.1 the low coherence length of the SLED was chosen to minimise problems due to the interference of stray reflections and indeed this property proved useful. The very short coherence length did, however, have some drawbacks. When this was 50μm, it meant that the fibre end would have to be within 25μm of the cantilever. (See the description of the optical fibre positioning in section 7.2.) While this was achievable at room temperatures, it was not certain that after the system was cooled the fibre would still be close enough to the cantilever, so an increase in the coherence length of the light source to some intermediate value was thought appropriate. The favoured answer was to use some kind of filter to narrow the SLED bandwidth, rather than use an alternative source. This would mean that the source and its drive electronics could remain as they were and it would be easy to revert to the original system when appropriate. Intermediate coherence light sources are hard to obtain at 1550nm as most devices at this wavelength are highly specified for communications applications.

The chosen solution used a device known as a *fibre Bragg grating* (or FBG) which is a fibre pigtailed device. The grating consists of a length of fibre (the order of millimetres or centimetres) which is patterned to present the propagating light with a periodic impedance change. The periodicity is carefully chosen to lead to high reflectivity to light of a chosen wavelength. The width of the filter response can also be chosen. The reflective nature of the device meant that it would have to be used in conjunction with either a circulator or a further directional coupler to recover the reflected component. A directional coupler was chosen as they are significantly cheaper than circulators. This did, however, mean that the light was subject to a further 6dB of loss over that when using an isolator, which will be solved in future experiments by using a circulator. The grating and extra directional coupler were set up as shown in figure 5.13 and inserted into the interferometer between the optical isolator and the directional coupler.

The choice of grating bandwidth presented a trade-off between optical power and coherence. A narrower pass band would result in a longer coherence length (see section 3.3.2) but would obviously also reduce the available optical power. If the grating bandwidth is much less than the SLED bandwidth and is centred on the SLED peak (so we can regard the SLED output as flat over the grating region), then the amount of power delivered to the interferometer will be linearly dependent on the

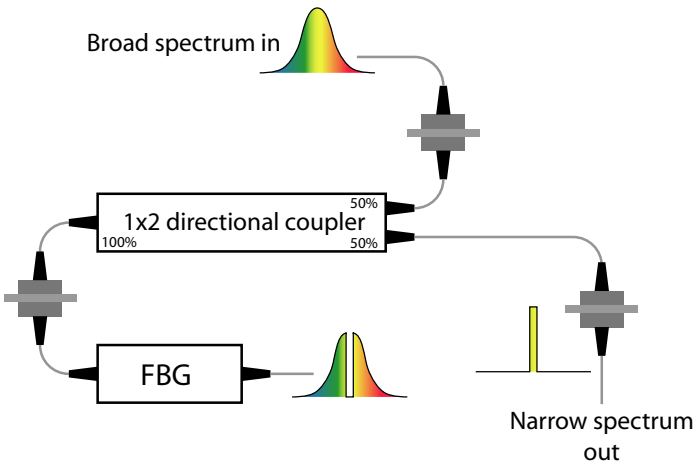

Figure 5.13: Use of a fibre Bragg grating and a directional coupler as a filter to increase coherence of light source.

grating bandwidth. Overall, the inclusion of the extra coupler and the grating were expected to reduce the light power at the sensor fibre end by about the order of 16dB (a factor of 40). The grating width was specified as being 5nm at -0.5dB and 7nm at -20dB. This would yield a coherence length of around $400\mu m$. The delivered grating had -0.5dB and -20dB widths of 5.2nm and 7.4nm respectively and its spectrum may be seen in figure 5.14 (a). The coherence length was measured by taking the inverse Fourier transform as detailed in section 5.1.3. The result of the transform is shown in figure 5.14 (b) and the coherence length can be seen to be $400\mu m$ taking it to be at the first minimum [70]. It can be seen that the transform looks similar to a sinc^2 curve, which is to be expected as the spectrum approximates a top hat function, the Fourier transform of which is sinc^2. With the grating and second 3dB coupler in place, the interferometer configuration is as shown in figure 5.15. The new 3dB coupler was chosen to be 2x2, rather than 2x1 as this would provide more flexibility as well as an opportunity to monitor the power in the interferometer. (A 2x1 coupler of this type is basically like the 2x2 coupler, with one of the ports terminated). With the SLED running at typical settings (200mA current, 16°C temperature setting) the optical power at point (i) was measured as 1.11mW and the power after reflection from the grating (point (ii)) was $21.4\mu W$. This provides an overall loss figure for the grating, 2x1 3dB coupler and the intermediate connectors of 17.2dB, slightly worse than the initial estimate. The power being launched into the sensor (and monitor)

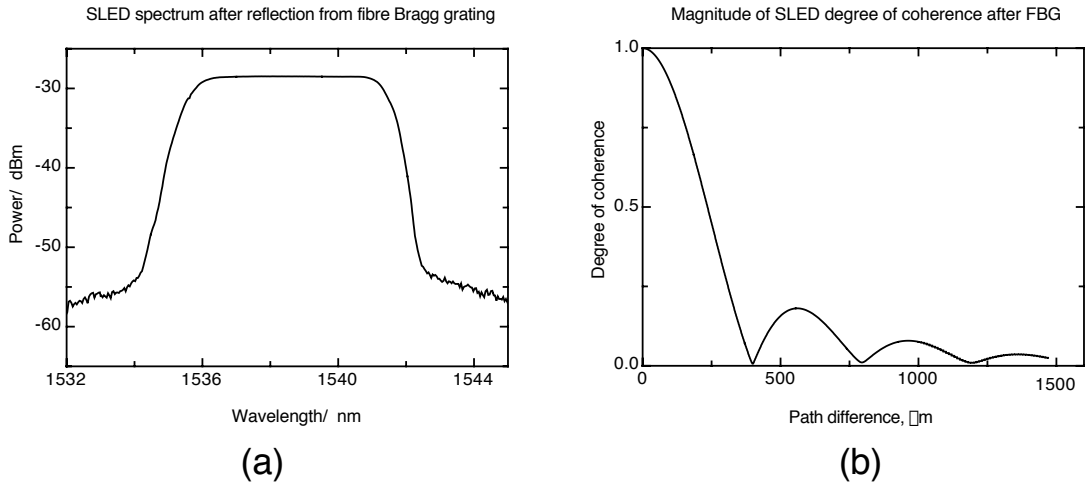

Figure 5.14: (a) Spectrum of SLED after reflection by the fibre Bragg grating, together with (b) the magnitude of the degree of coherence obtained by taking the inverse Fourier transform of the spectrum in (a).

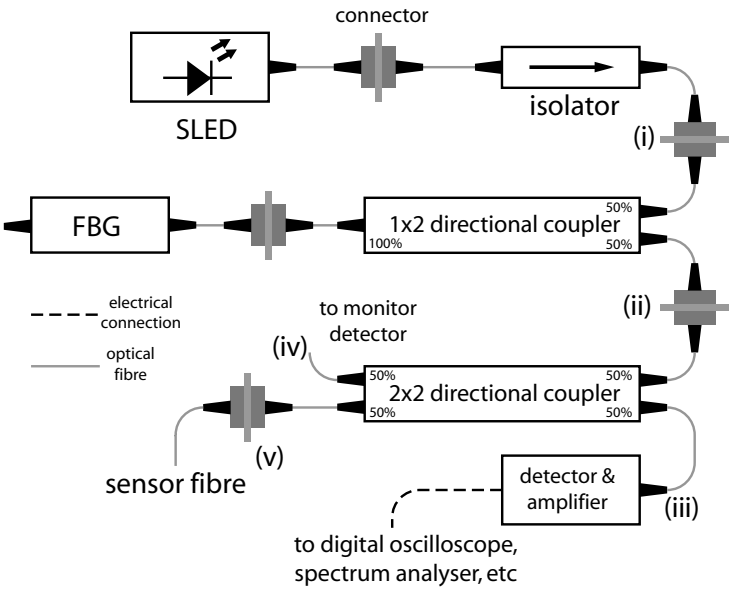

Figure 5.15: Fibre-optic interferometer after the addition of the fibre Bragg grating and the second 3dB directional coupler.

fibres (points (iv) and (v)) was about 10μW, as expected from the input to the 2x2 3dB coupler. The measured interferometer signal at point (iii) was about 40nW for the reflection from just the bare fibre end and about 1.2μW with the fibre end against a reflecting (but non-polished) surface. The background level for the power meter was 10nW. The exact power levels did vary as fibres were disconnected and reconnected showing that the connection quality is not perfectly repeatable, but by no more than 10%. This shows that the reflection from the cleaved fibre end is at least 25 times lower than that from the reflector, as expected.

5.6.2 Interferometer tuning

The discussion on interferometer noise and sensitivity in section 3.4 assumes that the interferometer is working at a quadrature point, i.e. the phase shift between the two reflected light components is $\pi/2$. This is the point where maximum sensitivity will be achieved. However, this is not necessarily the case, and indeed was probably not as the fibre was simply glued in place and no further adjustment was possible. It was desirable to have a way of tuning the interferometer phase. Some experiments have used piezoelectric devices to tune interferometer phase by adjusting the fibre-cantilever spacing but the addition of further complexity to the system was thought undesirable. An alternative is to instead adjust the operating wavelength of the interferometer, which will lead to a change in phase. This has been done elsewhere by altering the operating temperature of the light source [76]. A change in phase is related to a change in interferometer wavelength by

$$\frac{d\phi}{d\lambda} = -4\pi\frac{d}{\lambda^2} \tag{5.2}$$

where λ is the wavelength and d is the fibre cantilever separation. The required wavelength change for a $\pi/2$ phase change (enough to go from a sensitivity minimum to a maximum) is therefore given by

$$\Delta\lambda = \frac{\lambda^2}{8d} \tag{5.3}$$

This required wavelength shift is plotted as a function of separation d in figure 5.16. For a given available wavelength shift, $\Delta\lambda$, the minimum necessary spacing to achieve

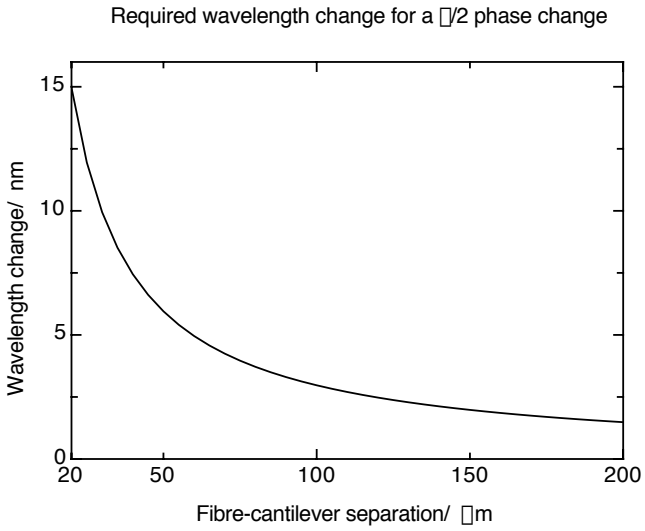

Figure 5.16: Required wavelength shift to change the interferometer phase by $\frac{\pi}{2}$, for an interferometer with an operating wavelength of $1550nm$.

a $\pi/2$ phase shift is given by

$$d \geq \frac{\lambda^2}{8\Delta\lambda} \tag{5.4}$$

As figure 5.16 shows, the required wavelength change for a given phase shift is a function of the fibre-cantilever spacing. Figure 5.4 shows that the current and temperature can both be used to alter the SLED centre wavelength. However, the short coherence length of the SLED means that the fibre and cantilever would have to be very close, so the required wavelength shift would be very large. The addition of the fibre grating, however, does offer a partial solution. Its use means that the spectrum is much narrower. Although the grating would remove the ability to temperature tune the wavelength of the light, the grating itself can be used to tune the wavelength by stretching. This method is in fact used as a way of sensing strain. A simple experiment was carried out with our grating to try tuning by straining, shown in figure 5.17. The grating was clamped in two places to a small micrometer-driven translation stage, on the moving part and on the stationary surround. The fibre was held by small pieces of aluminium, with thin pieces of rubber above and below the fibre to avoid crushing it. The grating could then be strained by adjusting the stage position. Figure 5.17 shows two FBG spectra, one while it was stretched and one while relaxed. The wavelength shift is about half a nanometre. This method yielded shifts of up to just over a nanometre, which would correspond to a phase shift of

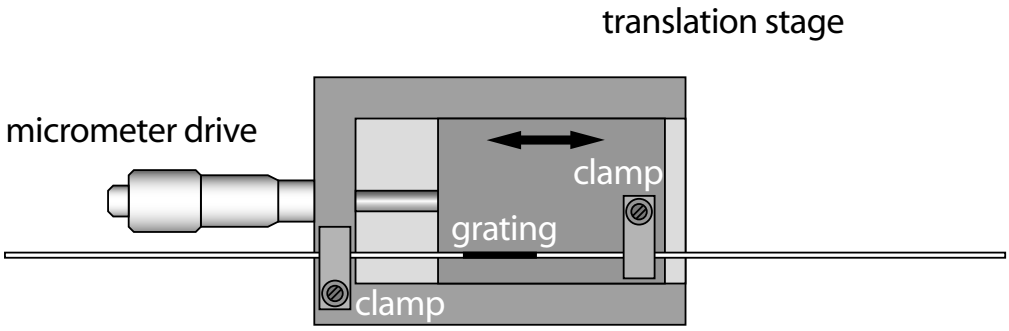

Figure 5.17: Simple arrangement for straining the fibre Bragg grating by clamping it to the moving and stationary parts of a small translation stage.

$\pi/4$ at a fibre cantilever separation of $150\mu m$. Although not a large enough phase shift to go from a minimum to a maximum, it would ensure we could move away from a minimum. This method can only shift the wavelength of the interferometer in one direction, but this should not matter. A better arrangement would be to wrap a similar grating (without plastic buffer coating) around a piezoelectric tube. The grating could then be tuned by using a voltage to expand the tube.

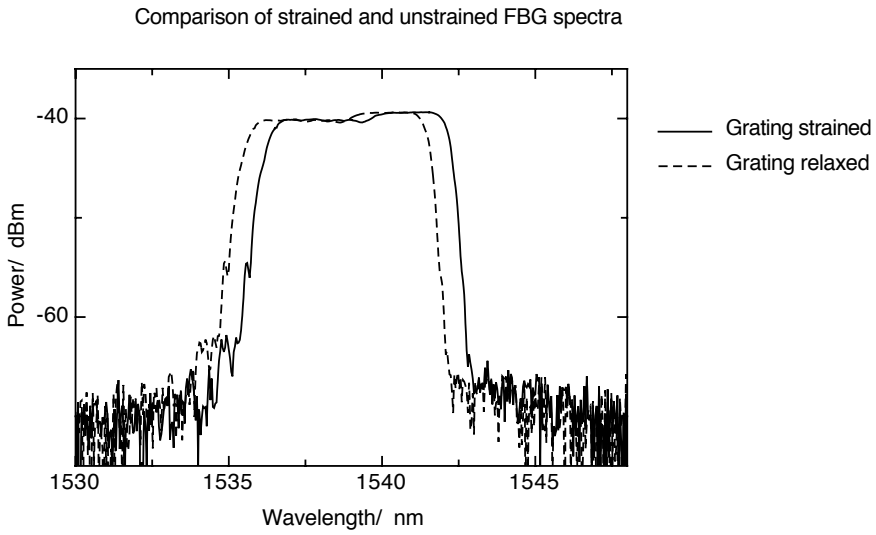

Figure 5.18: FBG reflection spectra showing the wavelength shift resulting from straining the grating. The shift is to longer wavelengths, as one would expect.

Chapter 6

Instrumentation II: Working with cantilevers

A large part of the effort in an MRFM project concerns the use of the micromachined cantilevers. This section discusses the background work done with the cantilevers and looks at some of their properties. Two different cantilever shapes were used; single beams and V shaped cantilevers with two legs. The single beam cantilevers were obtained from Nanosensors GmbH, Germany (now part of NanoWorld AG, Switzerland) and were made from highly doped single crystal silicon. The V shaped probes were made from silicon nitride and obtained from Veeco Instruments Inc, USA. Versions of both these brands of cantilever were used with and without integrated tips.

6.1 Cantilever characterisation

The initial characterisation of the cantilevers was simply to establish the resonant frequencies and their spread in value and the Q of the cantilevers while in air. This was done using the experimental arrangement shown in figure 6.1. Not shown in the figure is the stereo microscope used to aid the alignment of the cantilever with the fibre. The piezoelectric discs allowed the cantilever position to be adjusted very finely and also allowed the excitation of the cantilever by the application of an ac voltage. The addition of extra sets of piezoelectric discs (not shown) allowed separate control over the dc position and the ac excitation. The cantilevers were attached to the perspex spacer by double-sided tape. This made the addition and removal

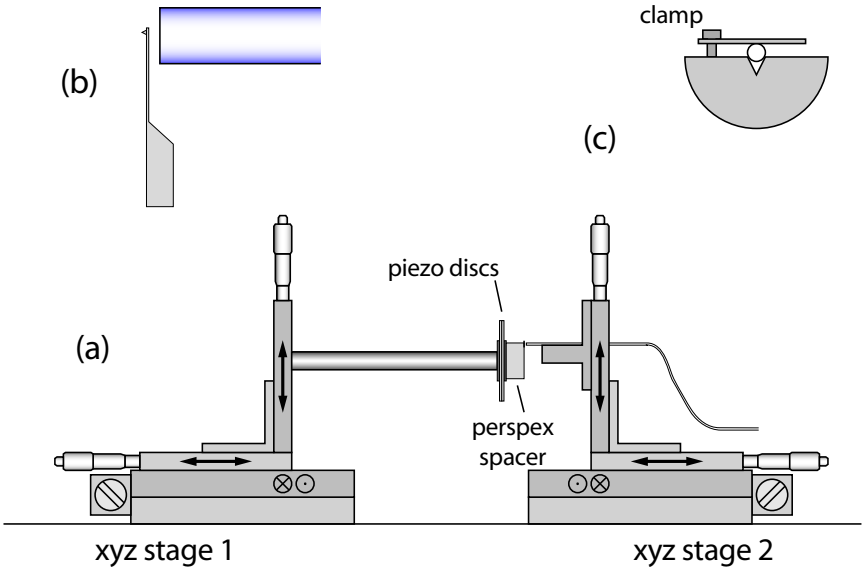

Figure 6.1: Experimental arrangement for looking at cantilever behaviour in air. The microscope used in these experiments is not shown. (a) Stages for positioning of cantilever and fibre. (b) Close up of cantilever and fibre. (c) End-on view of fibre holder showing fibre clamped into a v-groove. The fibre diameter is greatly exaggerated for clarity.

of cantilevers a simple (and non-destructive) process. The system was originally set up with either fibre or cantilever mounted on a moving stage, but this allowed less flexibility when attaching the cantilever. As mentioned in section 5.3, the photodiode amplifier had both ac coupled and dc coupled outputs. The dc coupled output was connected to a voltmeter to aid in alignment and the ac output was connected to an audio frequency spectrum analyser[1]. The system was found, as expected, to be very sensitive to mechanical noise, resulting from, for example, footsteps, closing doors and the cooling fans from bench top instruments. The worst of this noise was eliminated by carrying out measurements on a small but heavy optical breadboard which was supported by stacks of thin pieces of plastic foam. Acoustic noise was only a problem when frequencies of the order of kHz were present, easily minimised. A typical spectrum for a Nanosensors silicon cantilever is shown in figure 6.2. The cantilever was model CONT, usually intended for contact mode AFM and with a nominal resonant frequency of 13kHz and force constant of 0.2Nm^{-1}. Visible in the spectrum are both the fundamental resonance and the first overtone. The overtone

[1]Stanford Research Systems model SR770

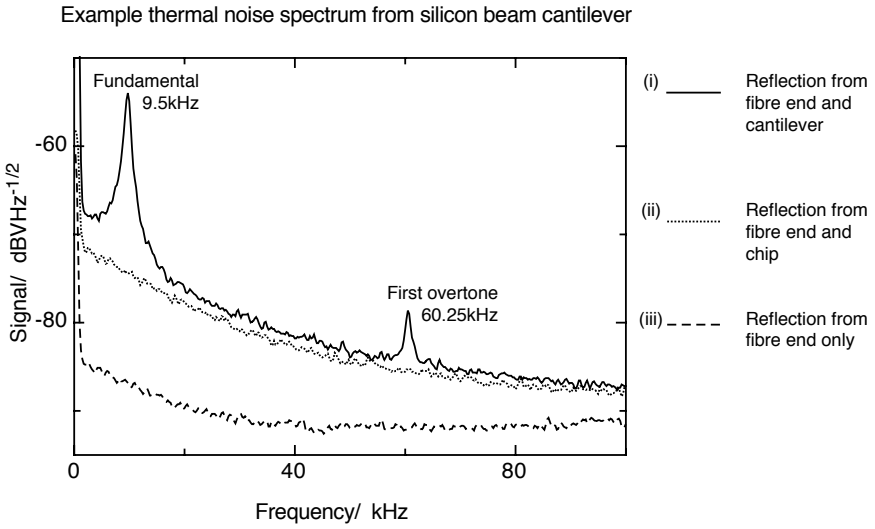

Figure 6.2: Thermal noise spectrum of a Nanosensors single beam silicon cantilever as measured in air and at room temperature using the photodiode amplifier described in section 5.3 and an audio frequency spectrum analyser. Also shown are the noise spectra produced by the reflection from the cantilever chip and the reflection from the fibre end alone. The spectra shown are averages of 100 spectra.

frequency agrees with the value obtained using the coefficients given in section 3.2.1 to within the resolution of the spectrum (250Hz). The high noise shoulder visible in plots (i) and (ii) is due to $\frac{1}{f}$ noise on the laser: plot (iii) shows a similar shape but at a much lower level. The Q of the fundamental is about 16. This low value is typical for these cantilevers and due largely to damping by the surrounding air (see the discussion in section 3.2.2). The Q of the overtone resonance is about 40. The overtone was not always visible in a measured spectrum, but the fundamental was usually straightforward to see, with the peak between 5dB and 25dB above the surrounding noise, depending on path difference. Because the low frequency shoulder in the noise was due to the SLED, it varied with the intensity of the reflected light. The intensity of the desired signal also varied with the reflected intensity, so if the peak was visible above the noise with a small portion of the light reflected by the cantilever, it would still be visible above the noise when more of the incident light was reflected.

The measurement of several cantilevers of the same type revealed that there could be quite a large variation in the resonant frequencies. The cantilever for which the spectrum is shown in figure 6.2 (i) had a theoretical resonant frequency of around

13kHz, but cantilevers of the same type were measured to have resonant frequencies from 9kHz to 15kHz. Variations in resonant frequency are due to variations in the cantilever dimensions, especially thickness. (See the expressions for the cantilever parameters in section 3.2.1). Such variations were not important. The electronics will function from around 1kHz to above the range of the spectrum analyser (100kHz). The important thing is to know the resonant frequency which is easy to measure using this method. Measuring resonant frequency by driving using the piezo disc was less successful because the mount had associated mechanical resonances. A magnetic excitation method tried subsequently and described later (see chapter 8) proved more useful.

6.2 Cantilever Q and pressure

The Q of the cantilever is a very important parameter in MRFM as obtaining a high Q is instrumental in trying to maximise the sensitivity of our experiments. Section 3.2.2 discusses the damping mechanism and splits the losses up into three mechanisms: energy lost to the fluid, energy lost via the cantilever supports and energy dissipated within the cantilever itself. Given that we are using a particular type of cantilever, it is obvious that we can only reduce the damping due to the fluid, which is usually the limiting factor [60]. This is done by operating the system in a vacuum. For the vacuum measurements, the cantilever and fibre were held together in various mounts, the design and construction of which are detailed in chapters 7 and 8. In order to get the interferometer light into and out of the vacuum vessel, a fibre optic vacuum feed through was used[2]. This consisted of a short section of fibre inside a metal case with FC/PC connectors at each end and a flange in the middle. Sections of pipe were made to which the feed-through could be attached and lengths of fibre with the appropriate connectors enabled the connection of the interferometer to the feed-through. Figure 6.3 shows the thermal noise spectra of a cantilever in air and in vacuum for comparison. The resonance becomes both sharper (i.e., higher Q) and about 15dB higher. Note also the shift in resonant frequency, which itself varies (though not a great deal) with pressure [61]. The low resonant frequency results from the cantilever having a piece of NdFeB magnet mounted on the end. The Q of the resonance in air and at 0.2 Torr are 18 and 1400 respectively. The relative frequency

[2]Oz Optics, Canada

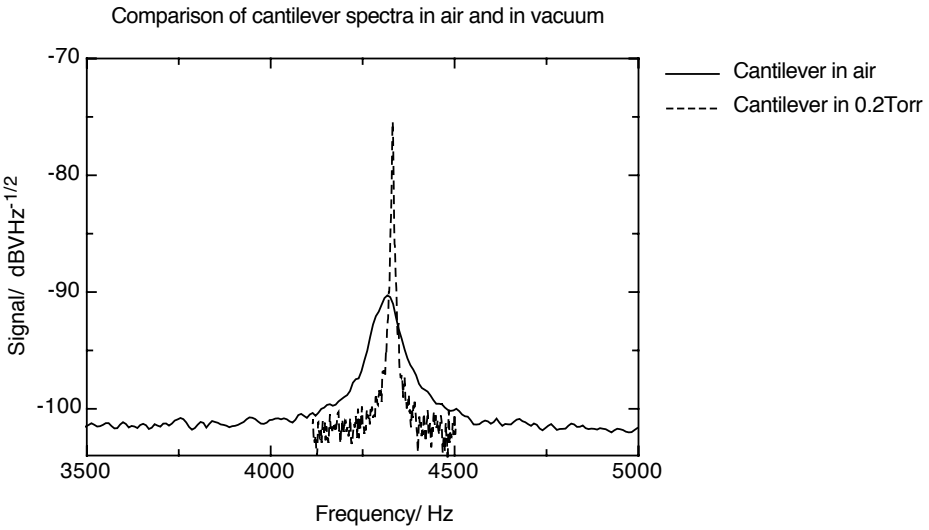

Figure 6.3: Two thermal noise spectra of the same cantilever, one taken in air and the other in 0.2Torr. The vertical scale is arbitrary, but the same for both. The baseline for the low Q resonance appears smoother because of the coarser sampling.

difference between the high- and low-pressure frequencies is 0.35%. In reference [77], Sader and colleagues present formulas for the change in resonant frequency due to damping which would suggest a change on the order of a tenth of this. In that paper, however, they themselves measured changes in frequency far larger than they could account for using the expressions presented.

6.2.1 Measuring cantilever Q

In instances where the thermal noise driven resonance is clearly visible with a spectrum analyser, the Q can be obtained directly from the spectrum. If a very large number of averages is taken (typically a few thousand) then this is trivial. With more noisy cases, it is useful to instead fit a curve to the resonance. The resonance may be well approximated by a Lorentzian function, which has the general form of [42]

$$y = H\frac{\Gamma^2}{4(x - x_0)^2 + \Gamma^2} \tag{6.1}$$

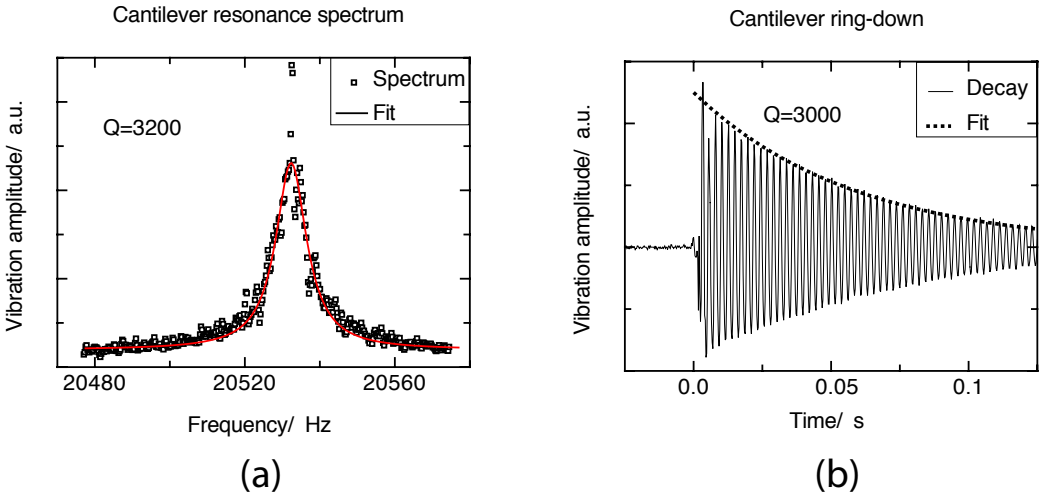

Figure 6.4: Examples of real data and fits for determining cantilever Q factor for a loaded SiN cantilever in a vacuum of 1.5×10^{-2} torr. (a) An average of 100 spectra , together with a fitted Lorentzian curve, indicating a Q of 3180. (b) An example of the cantilever ring-down after excitation. The fitted curve indicates a Q of 3000. Fitting to the minima yields a Q of 3170. It should be noted that the oscillation shown in (b) is *not* at the cantilever frequency. The samples for the data are spaced at 2ms, so the oscillations shown are an artifact of aliasing.

where H is the height of the peak, x_0 is the centre position and Γ is the full width of the resonance at half maximum amplitude. A program written in Matlab[3] was obtained that fitted a line of this form to data taken with the spectrum analyser. The program first linearised the spectrum (the analyser data was in units of dBV) then returned best fit values for H, Γ and noise offset level. As we require W, the full width at $1/\sqrt{2}$ rather than at $1/2$, we multiply Γ by a factor of $(\sqrt{2}-1)^{1/2}$. An example of a spectrum shown together with its fit is shown in figure 6.4(a). An alternative approach to calculating the Q, particularly useful in situations where the thermally excited vibrations cannot be detected using a spectrum analyser (for example when working at low temperatures), is to measure the ring-down time of the cantilever vibrations. This involves exciting the cantilever and fitting a decaying exponential function to the envelope of the resulting vibrations. The cantilever may be excited simply by striking the mount or, more usefully in experimental situations, using a burst of piezo-electric movement in the SPM system. Again, fitting of the results was done using a Matlab program[4]. The envelope of the ring-down may be described as

[3]Greg Johnson, Private communication
[4]Greg Johnson, Private communication

an expression of the form

$$y = A \exp\left(-\frac{t}{\tau_a}\right) \tag{6.2}$$

which describes the amplitude of the cantilever vibration after time t assuming an initial amplitude of A. The time τ_a is the time it takes the oscillations to decay to $1/e$ of the starting value. The Q of the cantilever is given by

$$Q = \frac{\omega \tau_a}{2} = \omega \tau \tag{6.3}$$

where ω in the resonant frequency and τ is the time it takes for the *power* (not the amplitude) of the cantilever vibrations to decay by a factor of e and is half of the corresponding amplitude decay time. An example of a cantilever ring-down measurement is shown in figure 6.4(b). The two different measurements shown in figure 6.4 were performed on the same cantilever in the same conditions one after the other, so should ideally yield the same result. The spectrum analyser and ring-down data yield values in reasonable agreement. Both these methods provide only an indicator of Q as the variation between Q values calculated from repeated spectrum analyser measurements was found to be on the order of 10%. The variation in values from ring-down measurements was around 30%, so the spectrum analyser method was preferred where applicable as results were more consistent. The large scatter in ring-down measurements is perhaps due to the cantilever vibrations being sufficiently large as to engender a non linear response from the interferometer.

6.2.2 Pressure dependence of cantilever Q

An overview of the variation of cantilever Q with air pressure has been presented in section 3.2.2. In figure 6.5 are plotted data sets from a number of measurements on a loaded silicon nitride cantilever. Blom's paper [61] predicts that Q will vary as the inverse of pressure between $1 Nm^{-2}$ and $100 Nm^{-2}$. A linear fit to a log-log plot of the data in figure 6.5 between $10 Nm^{-2}$ and $100 Nm^{-2}$ yielded a gradient of -0.8.

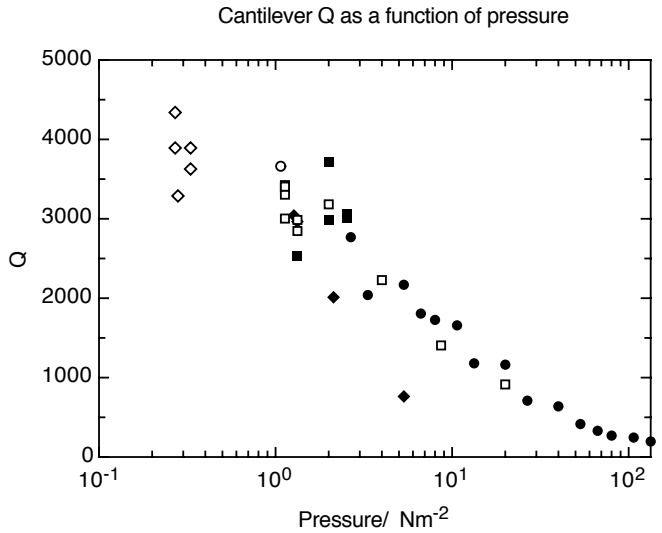

Figure 6.5: Q factor of a loaded SiN cantilever at a range of pressures. A logarithmic scale has been used for the pressure as the interesting behaviour is at low pressure. The different data markers represent different data sets, but all are calculated from lorentzian fits and all were measured on the same cantilever.

6.3 Cantilever loading

In order to perform an MRFM experiment, it is required to have either the field gradient source or the sample mounted on the cantilever. This section describes some of the effects that this has on the cantilever behaviour and the process of mounting particles on the cantilevers.

It is obvious that adding mass to a cantilever will change its resonant frequency, and expressions for the correction due to adding tips are given in section 3.2.1. This is in fact a method used for calibrating cantilevers [78] (i.e. measuring their force constants). The cantilever frequency, ω_c, should vary as [79]

$$\omega_c = \sqrt{\frac{k}{M + m_{\text{eff}}}} \tag{6.4}$$

where m_{eff} is the effective mass of the cantilever (given as approximately $0.24\times$ its actual mass in [79]) and M is a mass added to the end. Note, of course, that when $M = 0$, the equation reduces to that for any simple harmonic oscillator.

The force constant of the cantilever will remain the same when a mass is added only

if the mass is added at the tip. Otherwise, the force constant will be modified as [79]

$$k_{\mathrm{mod}} = k\left(\frac{l}{l+\delta l}\right)^3 \tag{6.5}$$

where l is the length of the cantilever and δl is the distance away from the free end. This can lead to large changes in force constant and hence resonant frequency. For example, a $450\mu m$ long cantilever with a mass $50\mu m$ from the end would be 42% stiffer than the same cantilever with the mass at the end, leading to a frequency increase of 19%.

The fragility of the cantilevers meant that while mounting particles on them by hand was possible, it proved difficult, so a micro-manipulator[5] was employed for the purpose. This was a stepper motor driven device controlled by joystick that could move a probe in all three dimensions with a claimed accuracy of 50nm. The probes were very finely pointed needles with a nominal tip radius (before use!) of 0.35μm. An adhesive was firstly applied to the end of the cantilever using the micro-manipulator. The particle was then picked up with the needle by static forces, then touched to the adhesive on the cantilever. Two different substances were used to adhere particles to cantilevers. High purity vacuum grease[6] offered the ability to re-use the same cantilever for multiple measurements, but would allow the possibility of particle movement in high fields. A two part epoxy adhesive[7] provided a more permanent solution but obviously meant that a cantilever could only be used with one particle. The grease was easier to handle with the micromanipulator needle and when using the epoxy, more care was required to regulate the amount applied to the cantilever. An example of an SiN cantilever with a piece of fluoranthene glued to the end is shown in figure 6.6.

6.4 Driven cantilever measurements

There were circumstances where it was desirable to measure the response of the cantilever to a driving force. If the interferometer spacing happened to be unfavourable for a thermal noise measurement, then driving the cantilever proved useful for charac-

[5]MicroManipulator Co, Carson City, Nevada, USA
[6]Dow Corning
[7]Araldite$^{\mathrm{TM}}$

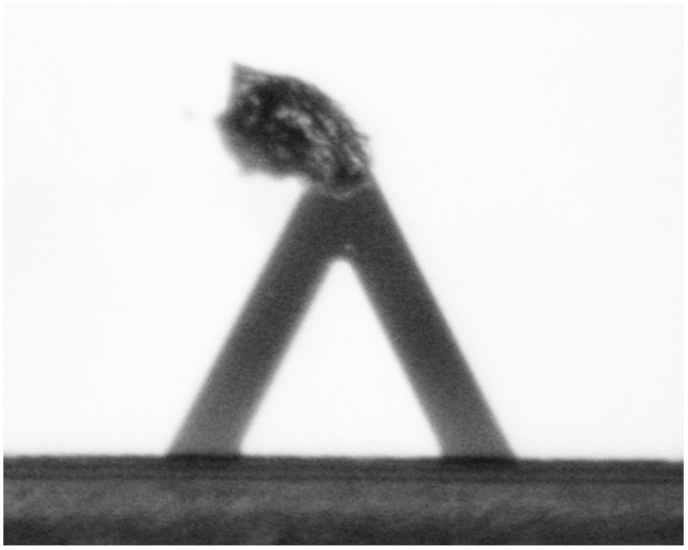

Figure 6.6: A silicon nitride cantilever with a piece of fluoranthene glued to the end shown at 200 times actual size.

terisation. This was carried out with two similar but different arrangements, shown in figure 6.7. The first used a similar arrangement to the characterisation stages shown in figure 6.1 with a small coil co-axial with the fibre and the second used the neater coil arrangement described in detail in sections 8.3.1.2 and 8.4. Measuring the cantilever frequency response this way has the advantage over the thermal noise observation that the response could be measured to a level further down from the peak. Typical thermal noise spectra in air had peaks 15dB to 20dB above the noise floor, whereas using the driven technique, the response could be measured to greater than 30dB below the peak.

Another opportunity afforded by driven measurements is that of calibration of the interferometer. When driving the cantilever at resonance and gradually increasing the driving current while viewing the interferometer output on a spectrum analyser, there comes a point when an increase in the driving current produces only a small increase in the size of the resonant frequency peak, and large signals are observed in the second harmonic. This is because at this point, the cantilever vibration amplitude is sufficient that the interferometer output can no longer be taken to be linear with cantilever position. The fundamental frequency interferometer output will not increase beyond that obtained when the peak to peak cantilever vibration amplitude is a quarter of the interferometer light wavelength. This assumes that the interferometer is sitting equidistant between a fringe maximum and a fringe minimum: if it

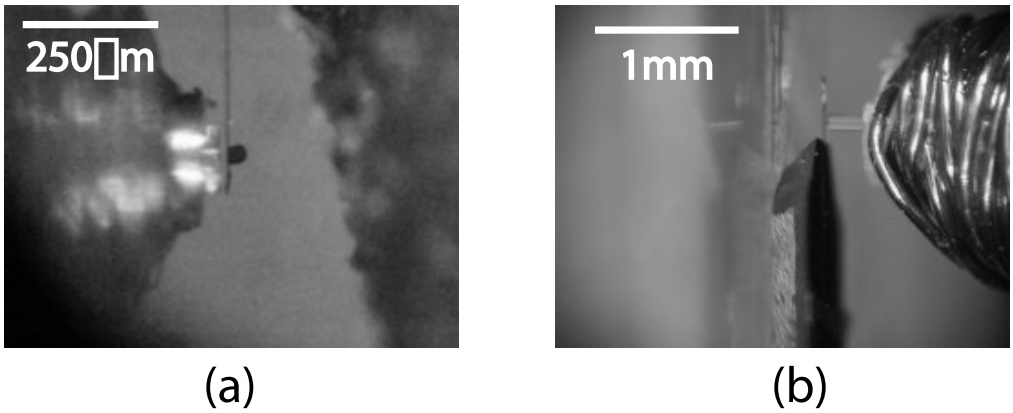

Figure 6.7: Two different arrangements for exciting the cantilever using small coils coaxial with the fibre. (a) The miniature coil built into cantilever mount #3 (see section 8.3.1.2). (b) Coil for experiments using translation stages rather than the cantilever mount. This arrangement was easier to set up, but less repeatable than the integrated coil. Both cantilevers have pieces of ferrite on the end, but in the case of (b), it is hidden in the glue.

is closer to one than to the other, then the nonlinear effects will be seen at lower vibration amplitudes. With large enough vibration amplitudes, higher order harmonics may also be observed. Because the fringes limit the maximum and minimum output voltages of the interferometer, knowledge of these maxima and minima enables the calibration of the interferometer. If the maximum and minimum voltages are denoted by $V_{\max}$ and $V_{\min}$ respectively, then the interferometer output, V_{out}, may be modelled as

$$V_{\text{out}} = \frac{V_{\max} - V_{\min}}{2} \cos\phi + \frac{V_{\max} + V_{\min}}{2} \tag{6.6}$$

where $\phi = 4\pi d/\lambda$ is the phase of the interferometer. Thus the sensitivity, s, of the interferometer is simply the derivative of the above with respect to d:

$$s = \frac{4\pi(V_{\min} - V_{\max})}{\lambda} \sin\phi \tag{6.7}$$

This shows that the sensitivity will be zero when ϕ is 0 or π. (Note that the zero point only applies to infinitesimal vibration amplitudes. For any non-zero vibration, there will be a small interferometer output, but it will all be at the frequency of the second harmonic of the cantilever vibration.) The above equation implies that in order to calculate the sensitivity, a knowledge of the cantilever phase is required. If

the measured interferometer voltage is V_{meas} then the phase may be calculated by

$$\phi = \cos^{-1} \frac{2V_{\text{meas}}}{V_{\text{max}} - V_{\text{min}}} \tag{6.8}$$

Although the value of ϕ is not single-valued, this does not matter as the gradient magnitude is equal whether the fringe is increasing or decreasing. Only the sign will vary but this can be determined using phase sensitive detection, or simply by observing the output on an oscilloscope. Thus, the interferometer may be calibrated by driving the cantilever with a coil until the extreme interferometer output values are reached to obtain V_{max} and V_{min}, then simply noting the d.c. coupled interferometer output and hence determining the phase. This coupled with the small amount of tuning available from the stretched grating (see section 5.6.2) should greatly aid in future measurements.

Chapter 7

Preliminary force detected ESR experiments

The main instrument of the project was based around an SPM system produced by Oxford Instruments, as described in chapter 8. Preliminary FDMR experiments using home made apparatus are detailed in this chapter. It begins looking at the overall approach taken to our high-field experiments before going on to describe the design of the experiment and the results yielded.

7.1 Our approach to FDMR

One of the distinctive features of our chosen FDMR strategy is to use "high" magnetic fields. This leads to an approach that differs significantly in terms of technological details to FDMR work undertaken by other groups. A summary of the previous work was presented in chapter 1. This section will describe the main consequences of working at higher fields.

One issue raised by performing FDMR at high fields is the use of superconducting magnets. Due to their cooling requirements, the field region is generally harder to access than that in an electromagnet. The sample space is typically down inside a cryostat with the sample mounted on a probe and inserted into the magnet.

If the sample itself requires cooling, this adds further complications. ESR systems

typically employ a flow cryostats or a variable temperature insert (VTI) to cool samples. We used a continuous flow cryostat, a system consisting of a vessel with evacuated walls through which cold helium is drawn to cool the experiment. Since a high cantilever Q is required, we may also need to evacuate the experiment. The instrumentation relevant to these concerns is discussed in chapter 8.

7.1.1 Magnet-on-cantilever approach

The majority of MRFM/FDMR experiments carried out so far have used the sample-on-cantilever approach as outlined in section 1.2.2.1. Mounting the sample on a cantilever, however, is a non-trivial task which is required for each experiment. With the magnet on the cantilever (e.g., see [8, 29]), multiple experiments may be performed with one cantilever and magnet. It also allows for the examination of arbitrarily large samples. We have used both methods: the experiments discussed in this chapter feature the magnet-on-cantilever method and both methods are used in chapter 8.

7.1.2 Millimetre-wave techniques and devices

The high field FDMR experiments will exploit the part of the electromagnetic spectrum from 90GHz to 300GHz. Known as the "millimetre wave" region, it sits between the microwave and far-infrared regions. These high frequencies make it harder to illuminate the sample than when using lower frequencies, such as for NMR experiments or lower field ESR, which typically use coaxial cables [22] or strip-line [80]. Neither strip-line or cables are suitable for use above about 40GHz as they become lossy. The usual solution is to use hollow metal *waveguides* down which the millimetre waves propagate. Waveguides are used over a very large frequency range, from a few GHz up to a THz, but single-mode guides (which avoid the coupling of radiation into other modes) become lossy around 90GHz. An alternative solution is *quasi-optics*. Here, instead of wave-guide, the signals are propagated through free space and manipulated with a range of optical elements, analogous to conventional optics. Most of the waveguide components found in conventional 10GHz spectrometers have quasi-optical counterparts. There follows a brief outline of some of the more important elements relating to the microwave requirements of the project.

7.1.2.1 Millimetre-wave sources

Millimetre-wave radiation may be generated in a number of ways. A common method currently used in the St Andrews ESR spectrometer is to use a *Gunn diode*, a solid state device placed in a cavity and biased to produce oscillations [81]. The spectrometer oscillator uses a commercial diode placed in a home made cavity operating in second harmonic mode. A wide tuning range (about 15GHz at 90GHz) is available by altering the cavity length, and thus its resonant frequency, with a micrometer drive. A second micrometer allows for the adjustment of a sliding short circuit behind the diode to optimise the output power coupling. Finer adjustments to frequency may be made by adjusting the bias voltage. Another device used at St Andrews is a *backward wave oscillator* [82] which uses the interaction of an electron beam with a slow wave structure to produce radiation from 75GHz to 110GHz. Due to its bulk and relatively noisy output, it was not used for ESR, but was useful for some characterisation measurements described later. A third way of generating millimetre-waves is to frequency multiply the output from a lower frequency oscillator. A system capable of generating 150mW at 94GHz has recently been constructed at St Andrews, based on a 7.5GHz source [83]. (This approach will be used for future work and should result in much lower noise.) All three of the above methods allow easy tuning.

7.1.2.2 Waveguides and feed-horns

A single mode waveguide normally has a rectangular cross section, usually with a 2:1 aspect ratio, but some applications use circular guides. In a rectangular guide, the polarisation is parallel to the short dimension, but in a circular guide the polarisation may become distorted. Plain single mode guides become lossy at mm-wave frequencies, and a low loss solution is to use oversized corrugated guides which have very low losses and preserve polarisation well. Smith et al. [51] employed such a guide in a high field spectrometer with less than 0.01dB loss. The low loss is due to the corrugations, of which there should be as many as possible per wavelength. To go from single mode waveguide to a corrugated guide, or from waveguide to free space, feed-horns are used. These are essentially sections of waveguide that flare at one end to couple from the guide to the Gaussian beam modes used to propagate the beams in free space. These are also corrugated for better performance and can offer efficiencies greater than 95%. The feed-horns are made by electroplating copper

onto aluminium mandrels with the corrugation pattern cut into them, so very fine corrugations (periods of several hundred microns or less) may be obtained. Gaussian beam optics requires a more sophisticated mathematical treatment than ray optics and is used where the size of the beam is comparable to that of the optical elements. The beams may be characterised by a beam waist size and wavelength, from which other parameters may be deduced [84].

7.1.2.3 Beam manipulation

Various devices allow for the manipulation of the beam. One such component is the wire grid polariser. These are formed from grids of very fine tungsten wires and transmit radiation polarised in the plane perpendicular to the grid axis. Very high performance is achievable using this type of polariser: a grid of 25μm tungsten wires separated by 50μm will have cross polar rejection of the order of 60dB and losses of less than 0.01dB at 94GHz. Wire grids may be used up to THz with finer wire.

A very useful device in quasi-optical systems is the Faraday rotator [85]. This is a free space device consisting of a sheet of ferrite material magnetised in the direction through the material. A linearly polarised beam may be treated as two counter-rotating circularly polarised beams, and the refractive index of the ferrite differs for the two beams. This means that the relative phases are changed by a pass through the device, resulting in a rotation of the linear polarisation. The rotation direction is the same *relative to the device* for either direction through the device: i.e. a beam travelling one way will experience a clockwise rotation and a returning beam would suffer an anticlockwise rotation when looking along the direction of the beam. If the thickness of the rotator is such that a 45° rotation is obtained on each pass, then a beam passing through the device and then reflected back through it will experience a total rotation of 90° and may be diverted by an appropriately angled polariser. This allows the construction of free space isolators and circulators, so that the detector in an ESR spectrometer will not see any signal directly from the source and the source will not be affected by power reflected back from the cavity.

Gaussian beams are by nature divergent, so require focusing elements. Focusing may be performed using dielectric lenses (made from HDPE, for example) but they may be thick and thus lossy; an alternative is to use off axis elliptical mirrors. Mirrors may be combined in such a way that the resulting optical system is frequency independent,

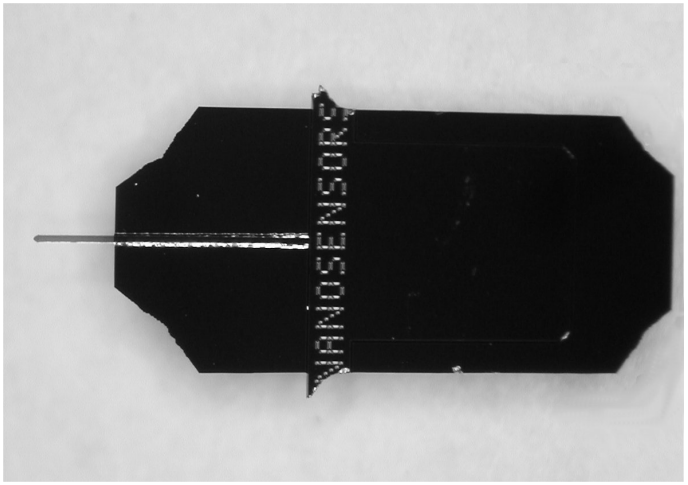

Figure 7.1: A Nanosensors cantilever with its chip. The cantilever itself is $450\mu m$ long and $45\mu m$ wide.

allowing the same optics to be used over a large range of frequencies. This is the approach used in the St Andrews ESR system.

7.1.2.4 Detectors

The device used to detect the ESR signal is a type of bolometer, a name for any device in which the incident radiation warms a sensing element. The detector is specifically a *hot electron* bolometer, a semiconductor (InSb) device whose conductance properties change with temperature. This type is faster than resistive wire bolometers and less noisy than using a semiconductor diode.

7.2 Cantilever mount design #1

The cantilevers used for the first proof of principle experiments were beam shaped cantilevers obtained from Nanosensors GMBH. A photograph of a Nanosensors cantilever is shown in figure 7.1. A mount had to be designed to accommodate the cantilever and the sensing optical fibre, allowing placement of the cantilever close to the experimental sample. Cantilevers of the type used for force detection are very fragile so, in case a cantilever was broken it was important to design a system to replace it without having to re-align the fibre. Nanosensors also supply a small silicon

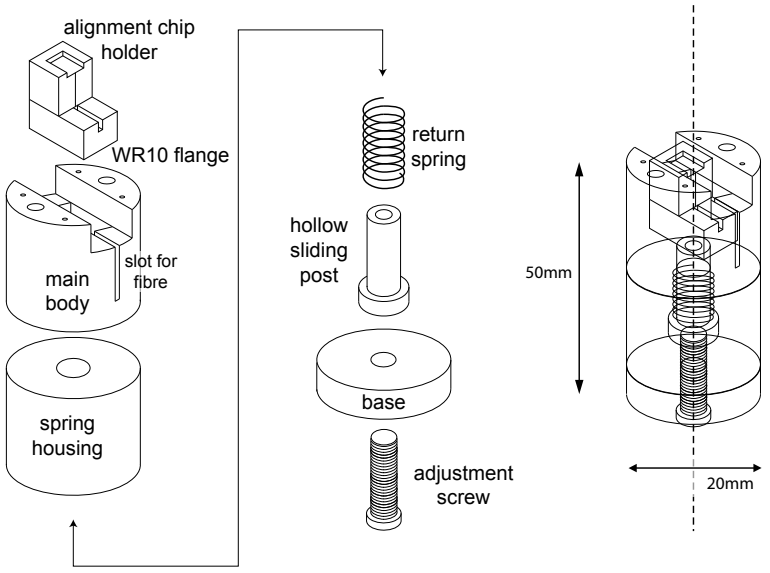

Figure 7.2: Simple schematic showing the parts of cantilever mount #1and how they fit together.

mounting chip with a ridge that mates with a corresponding groove on the base of the cantilever chip, allowing cantilever placement with a quoted accuracy of $\pm 5\mu$m. One of these alignment chips fixed to the mount would allow easy cantilever replacement.

An adjustable fibre-cantilever spacing was desirable, but would add a great deal of difficulty to the experiment so a fixed spacing would be used. Variable sample-cantilever distance, however, was a definite requirement, so the mount would consist of a piece holding the fibre and cantilever and itself be able to move in the z(magnetic field) direction it the overall support structure. The mount would obviously have to be made of a non-magnetic material.

A suitable mount was designed and constructed as shown in figure 7.2 which shows the mount split into several main parts. The upper-most piece, which has machined into it a notch to accept a Nanosensors alignment chip, has a rectangular cross section which locates it in the main body piece while allowing it to slide up and down. Precise machining ensured that possible lateral motion of the alignment chip holder was minimised. The line running down the face of the alignment chip holder adjacent to the chip notch is a small groove, approximately 200μm wide, used to aid the location and alignment of the optical fibre. The wide notch in the base of the alignment chip

holder allows the optical fibre to slowly bend through 90° in order to emerge from the mount through the slot in the body. The alignment chip holder is screwed to a sliding post which can move up and down in the spring housing. A screw is used to push the post up and a spring provides a restoring force allowing the vertical position of the cantilever to be adjusted. The top of the mount body has holes drilled out to mate with a waveguide flange of type UG387/U-M, allowing it to be attached to a variety of waveguides through which the mm-wave field was to be applied. The mount was constructed from nickel silver, an alloy of copper, nickel and zinc. This material is non-magnetic and has good machinability. It is a commonly used material in cryogenic systems in which low thermal conductivity is necessary. When assembled, the completed mount was 20mm in diameter and 50mm in length, with around 15mm of the adjustment screw protruding from the bottom.

A closer look at the alignment chip holder is shown in figure 7.3. This shows the cantilever and alignment chip, together with the optical fibre. The alignment of the fibre with the cantilever was carried out under a stereo microscope. A cantilever was placed on the alignment chip using vacuum grease to hold it in place. The alignment chip was then moved to line up the cantilever with the top of the fibre locating notch in the face of the alignment chip holder and glued in place using an epoxy adhesive. Once this set, the piece was placed on its back and the fibre was laid into the alignment notch, using a stepper motor driven micro-manipulator to position it. The manipulator held the fibre in place as it was glued and set. The bare fibre had a minimum bend radius of around 5mm, sufficient to extract the fibre out through the side of the mount. It was found that the stress on the fibre at the point it was glued to the mount meant it easily broke. This was solved by keeping the bare section as short as possible and gluing the plastic coating of the fibre to the mount also. The bare section of the fibre also had to be glued as the fibre was found to move inside its plastic coatings. The bottom piece of the alignment chip holder was then attached and more glue was added to pot the fibre in place for extra strain relief. Once the whole mount was assembled, it could be inserted into a surround made from Tufnol^{TM}, a material made from tightly compressed fabric in a hard resin and commonly used in magnet systems. This had an outer diameter of 49mm, sized to provide a loose fit with the cryostat used for some of the measurements, allowing it to guide and protect the mount when it was inserted and removed. Other experiments just used the fairly large bore of the magnet, so no protective holder was required. The final assembled guide is shown together with the surround in figure 7.4. In order

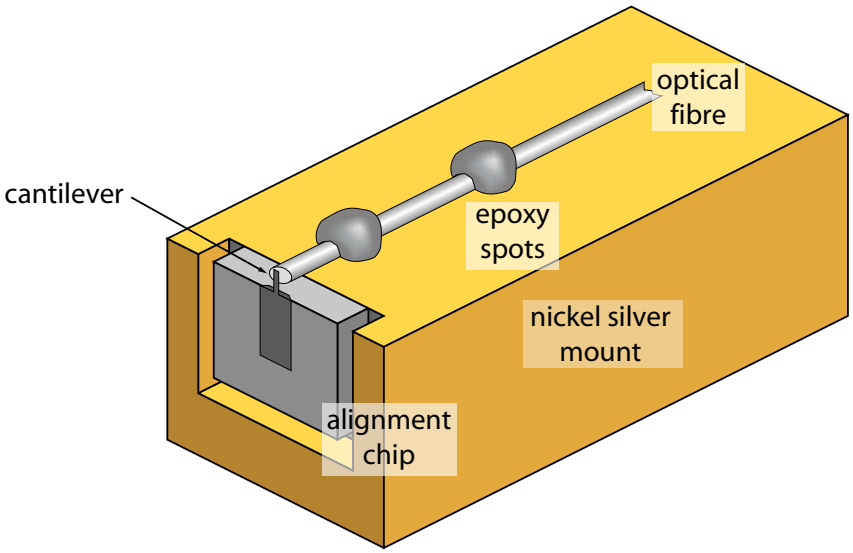

Figure 7.3: Schematic of the top part of the alignment chip holder showing the positioning of the optical fibre with respect to the cantilever. The sizes of the cantilever and the fibre have been exaggerated.

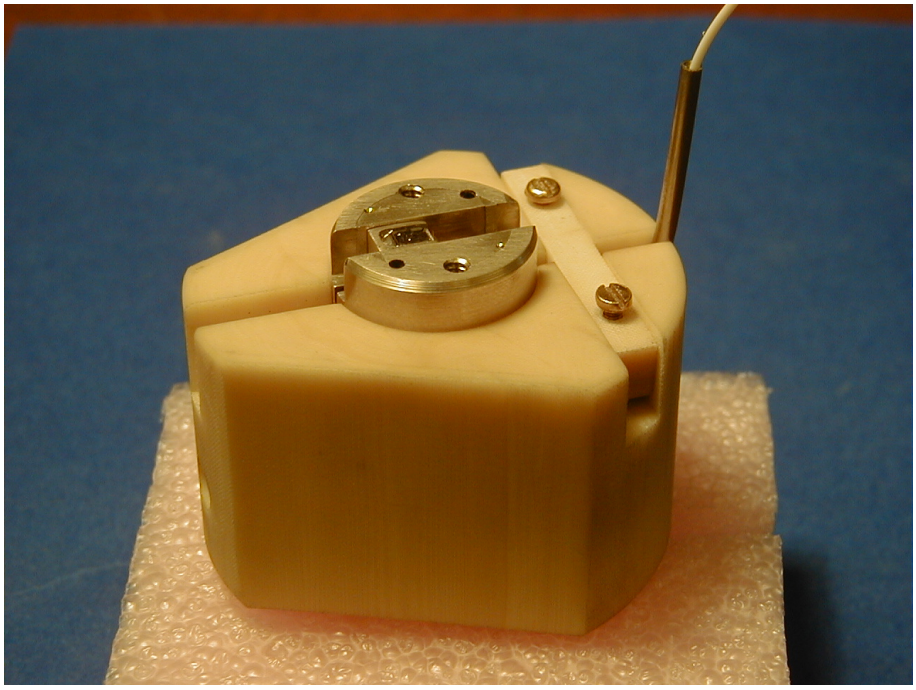

Figure 7.4: The first cantilever mount with Tufnol^{TM}surround. The optical fibre can be seen emerging from a stainless steel protective tube.

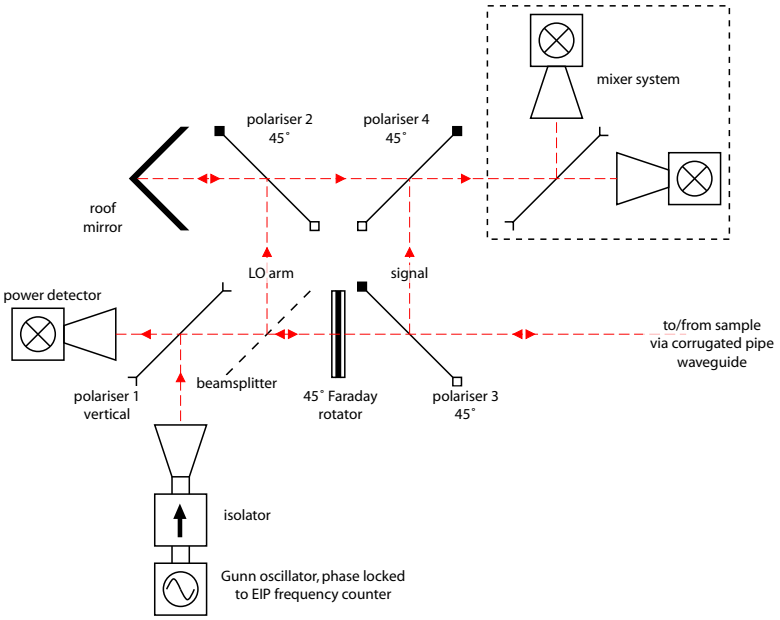

Figure 7.5: Simplified diagram of the quasi-optical ESR system, with the focussing elements not shown.

to position the sample above the cantilever, it was glued to a 0.5mm thick, 5mm square piece of polyester (PET). At this thickness, the PET was close to transparent to millimetre waves. Lower loss dielectrics are available, but the PET was used for its optical transparency which enabled the lateral alignment of the sample with respect to the cantilever to be ascertained more easily. After the sample was positioned over the cantilever, the PET was held in place by clamping it between the top of the cantilever mount and the flange of the mm-wave waveguide.

7.3 Experiment design

The first preliminary experiments were based around the St Andrews group's existing quasi-optical high-field electron spin resonance spectrometer, operating in non-resonant induction mode [51]. The bulk of the signal processing is carried out by the quasi-optical circuit shown in figure 7.5. The detector was an indium antimonide (InSb) hot electron bolometer. The detector required cooling to 4.2K, so resided in a liquid helium cryostat. The output from the detector was fed to a lock-in amplifier which was connected via GPIB (*g*eneral *p*urpose *i*nterface *b*us) to a computer, also

connected to the magnet control system and other instruments via GPIB. The spectrometer was controlled by a program written in Lab View^{TM}. The ESR program could also be used for FDMR experiments, requiring just that the millimetre-waves were modulated (rather than the magnetic field) and that the lock-in amplifier measured the interferometer output rather than the InSb bolometer output. The magnet in the ESR spectrometer was a ± 12 Tesla Teslatron swept field superconducting solenoidal magnet from Oxford Instruments with a room temperature 89mm diameter bore. Synchronous detection requires that the magnetic field be modulated and this modulation was provided either by a set of coils built into the sample cryostat, or a separate set of coils outside of the cryostat. The modulation coils were driven by a output from the lock-in amplifier, after separate amplification. The spectrometer could be configured (with different millimetre wave sources) for operation at 90, 180 and 270 GHz. The source was an indium phosphide (InP) Gunn diode and a frequency doubler and tripler facilitated the extension to the higher frequencies. Using the ESR spectrometer with few changes meant that ESR and FDMR experiments could be carried out immediately after each other for comparison purposes.

The quasi-optical circuit for the spectrometer was bolted on an aluminium base-plate positioned above the magnet, the axis of which was vertical. The base-plate was supported by a stainless steel frame. The top of the corrugated waveguide to which the experiment was fixed sat below the base-plate and was covered by a PTFE window, allowing evacuation of the experiment if desired. The experimental arrangement for the first FDMR experiments using mount number one is shown in figure 7.6. The diagram shows schemes for both amplitude and frequency modulation of the B_1 millimetre wave field. The amplitude modulation was done by a solid state fast modulator, a waveguide component inserted between the waveguide directional coupler and the feedhorn. This device had its own driver circuit, and was controlled by the reference oscillator of the lock-in amplifier. The modulator allowed for any attenuation between zero and full, but in these experiments, 100% modulation was used with a square-wave driving the modulator. The frequency modulation was carried out simply by modulating the gunn diode bias voltage with the lock-in reference oscillator through the diode power supply. The cantilever holder was bolted to the flange of a corrugated feed-horn which was in turn fixed to the end of a long corrugated pipe. A schematic of the feed-horn flange bolted to the top of the cantilever holder is shown in figure 7.7.

Many FDMR experiments [5, 11, 12, 14] have used DPPH as a test sample. DPPH,

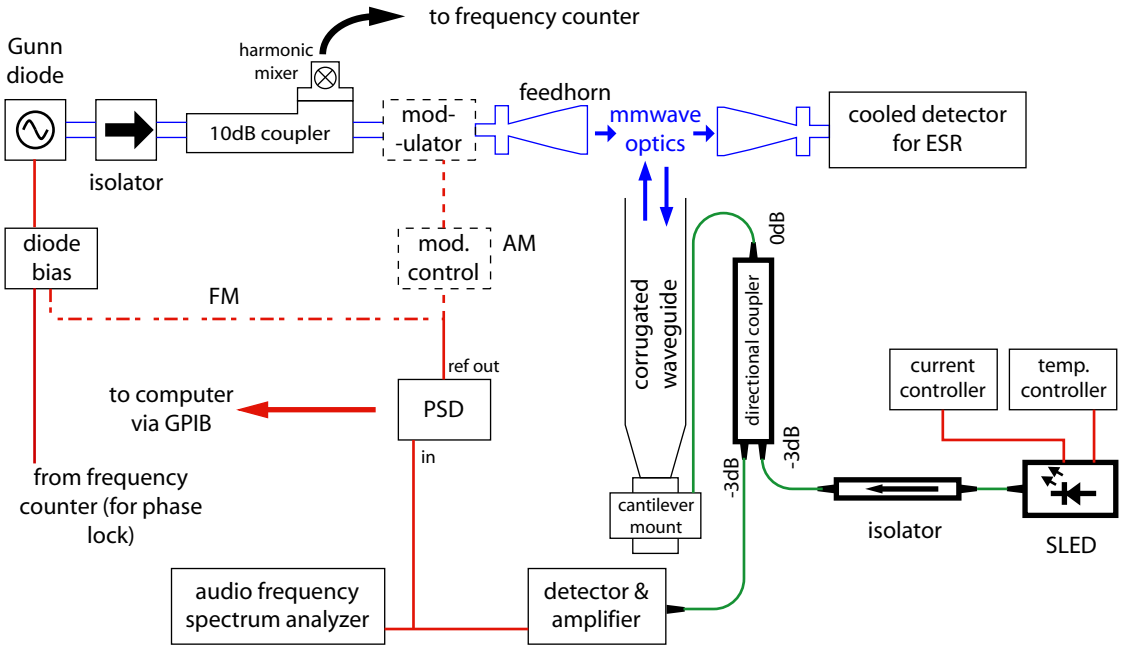

Figure 7.6: Schematic of the experimental arrangement to measure force detected magnetic resonance. For clarity, the magnet and modulation coils for the conventional ESR experiments have been omitted. The green lines indicate fibre optic connections, while the red indicate electrical connections.

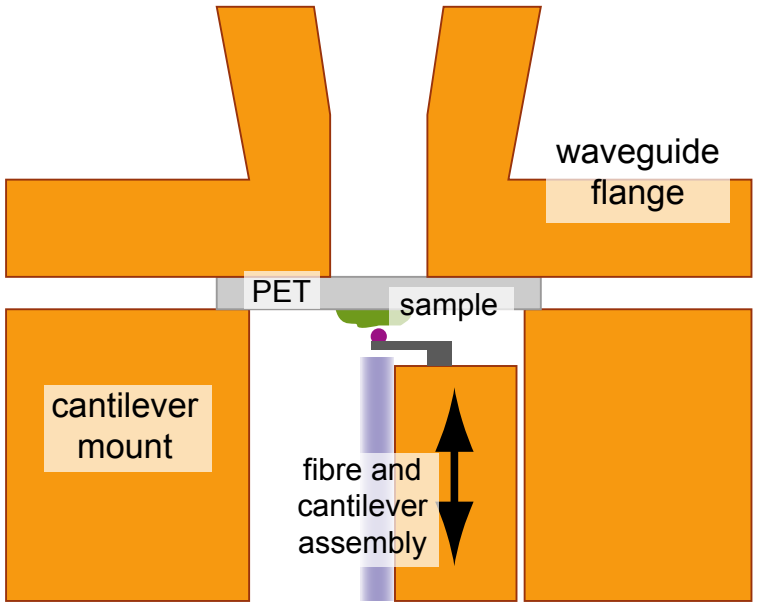

Figure 7.7: Schematic of first cantilever mount with sample in place and feed-horn attached.

however, is difficult to saturate at room temperature with $\tau_1 \approx \tau_2 \approx 2 \times 10^{-8}$s. We decided to use instead (fluoranthene)$_2$PF$_6$. This material is a one dimensional conductor with a narrow linewidth at 10GHz of around 1.5×10^{-6}T, although the linewidth at 94GHz was found to be about 10^{-5}T. It is an ideal test sample for FDMR experiments as it has a long τ_1 and τ_2 ($7.2\mu s$ and $5.4\mu s$ respectively) so may be saturated at low power levels. This ease of saturation is important to this type of FDMR experiment, especially when working in non-resonant mode. The sample used was a single crystal, approximately $0.5 \times 0.3 \times 0.2$mm. The (FA)$_2PF_6$ was glued to the PET support. The support was then positioned on the top of the cantilever mount and held in place with vacuum grease before being clamped to the cantilever mount by the flange of the corrugated feed-horn. Once the mount was attached to the horn, the adjustment screw was used to bring the cantilever close to the (FA)$_2$PF$_6$ sample. This was done under a microscope with 50× magnification. A graticule in the microscope allowed the sample-cantilever spacing to be measured as around 80μm.

7.3.1 Cantilever probe magnets

The probe magnet is a vital part of an FDMR experiment. Previous experiments by other groups have used a range of materials: iron, nickel, cobalt and the permanent magnets neodynium iron boron (NdFeB), praseodynium iron boron (PrFeB), samarium cobalt (SmCo) and Alnico.

There are various trade-offs in choosing a cantilever magnet. A large anisotropy field is desirable so that any resonant interaction of the magnet with the RF will not occur at fields of interest for $g \approx 2$ samples. A large moment would be desirable for best magnetic moment sensitivity and a low ac conductivity is desirable as otherwise eddy current losses could become significant and lower the Q of the cantilever.

Three materials were tried as gradient sources: NdFeB magnet, iron and a barium/strontium hexa-ferrite.[1] Of these, the most promising was the ferrite. The cantilever Q was lowered when a field was applied when the cantilever had a magnetic particle on it. With the ferrite, the Q at 3.5T was lowered by factors of between 1 and 4 compared to the zero field value, but with the iron or the NdFeB, the Q was almost totally destroyed, to the point where the thermal noise peak could not be seen above the amplifier noise floor. The Q reduction was larger for larger par-

[1] Ferroxdure 300, manufactured by Philips

ticles: the Q was completely destroyed for a cantilever with an approximately 50μm piece of NdFeB mounted on the tip, but for a 20μm particle the thermal noise peak was visible up to 10T. Similarily for ferrite tip magnets, a 50μm particle led to a Q reduction of a factor of 3, but a 20μm particle tipped cantilever showed no clear Q reduction at 3.5T. The drop in Q was thought to be at least partly due to losses from eddy currents induced in the magnetic tips by the cantilever motion. The ferrite had a much lower conductivity than either of the metals, so would not be as subject to this effect. Both metal and non-metal magnets would be susceptible to losses due to the energy required to re-orient the magnetisation as the cantilever moved up and down. The drop in Q occurred most dramatically at lower fields: above 0.5T or so it didn't change a great deal. Dramatic lowering of the Q was also reported by Wago et al. [10] where they describe a drop in Q from a zero field value of over 100,000 to 100 at 0.45T for a cantilever tipped with a 110μm diameter nickel sphere. They attributed this to micro-magnetic losses.

Eddy current losses would not completely preclude the successful use of metallic tip magnets. The eddy current losses in a sphere are given in [86] and will depend on a^5 where a is the particle size. Moving from 50μm particles to 1μm particles will thus reduce the losses by a factor of 3×10^8. The losses also scale with the square of the field and the square of the cantilever frequency. This is unfortunate as sensitivity increases with both the field and the cantilever frequency. Metallic tip magnets at smaller sizes may therefore be worth further investigation for lower field measurements. This problem does, however, suggest that magnet-on-cantilever experiments should be performed with the cantilever plane perpendicular to the applied magnetic field as the cantilever motion will be parallel to the field and hence induction current losses lower than if the cantilever motion was perpendicular to the field. Both our experiment and Wago's mentioned above use this arrangement, so Q reductions may have been even worse otherwise.

7.3.1.1 Field dependency of cantilever resonant frequency

Any extra forces exerted on the probe magnet due to the applied field, and hence on the cantilever itself, may be expected to alter its behaviour. Looking at figure 7.8 we can see that if we presume the probe moment to be perpendicular to the plane of the cantilever, any cantilever deflection will result in a change in orientation of the probe magnet. This will lead to a torque on the probe moment and thus an extra force on

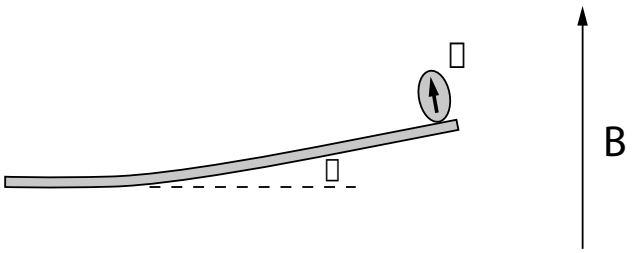

Figure 7.8: Simple schematic of a magnetic probe particle on a cantilever. The moment of the probe particle points out of the plane of the cantilever.

the cantilever. The effect of the extra torque on the cantilever's resonant frequency can be included as an extra contribution, k_{mag} added to the cantilever force constant, k_0, and the resulting cantilever frequency will be given by

$$\frac{\omega_c}{\omega_0} = \sqrt{\frac{k_0 + k_{\mathrm{mag}}}{k_0}} \tag{7.1}$$

as the resonant frequency goes as the square root of the force constant as stated in section 3.2.1. ω_0 is the cantilever resonant angular frequency with no field and ω_c is that with the field. Assuming that the easy axis of the magnetic particle is initially perpendicular to the cantilever plane, and parallel to the magnetic field, then if the cantilever is bent away from the horizontal, the easy axis of the magnet will move away from the field direction by the same amount. The magnetisation vector **M** of the magnet will now be pointing in a direction between that of the magnetic field and the new orientation of the easy axis [87].

By considering the energy of the probe magnet as a function of the cantilever angle θ, and assuming the probe moment parallel to the field and perpendicular to the cantilever plane, it may be shown that the magnetic part of the force constant can be described by[2]

$$k_{\mathrm{mag}} = \left(\frac{\alpha}{l}\right)^2 \left(\mu B \frac{(2K/M) + \mu_0 M(N_y - N_z)}{B + (2K/M) + \mu_0 M(N_y - N_z)}\right) \tag{7.2}$$

[2]G. M. Smith, private communication.

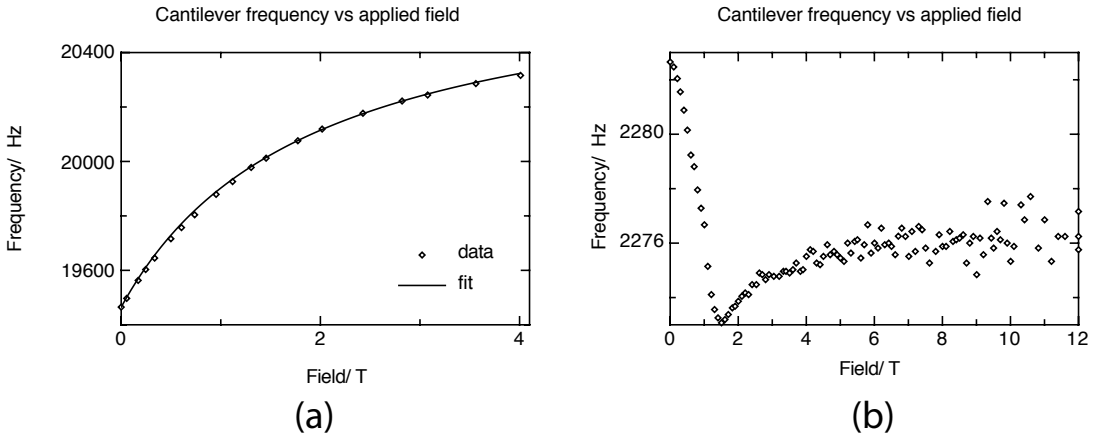

Figure 7.9: Typical cantilever resonant frequency behaviour as a function of applied field when the magnetisation of the probe magnet initially lies primarily (a) perpendicular to and (b) in the plane of the cantilever. The tip magnet in (a) was a piece of ferrite and in (b) was a sample of magnetic recording media. The line in (a) is based on equation 7.3 with a moment value chosen for a good qualitative fit.

in which μ is the moment of the tip magnet, B is the applied external magnetic field, $2K/M$ is the crystalline anisotropy (a simple approximation: the full anisotropy contribution to the energy is more complicated), M is the magnetisation of the ferrite and N_y and N_z are the demagnetisation factors in the respective directions to account for any shape anisotropy. α is a constant depending on the cantilever and resonant mode and for a beam cantilever oscillating in its fundamental mode has a value of 1.37 [87]. If we assumed negligible crystalline anisotropy then we could neglect the term in K and the expression would reduce to that given by Marohn et al. [87] where the field dependence of the cantilever came from the shape anisotropy of the probe magnet and there was no crystalline anisotropy. We are assuming, however, that our probe magnet is spherical, so the shape anisotropy terms vanish and the expression for resonant frequency becomes

$$\omega_c = \omega_0 \sqrt{\frac{k_0 + \mu B \frac{2(K/M)}{B+2(K/M)}}{k_0}} \tag{7.3}$$

The discrete points in figure 7.9 (a) show measured data of frequency as a function of field for a SiN cantilever with a piece of ferrite on the end. The line is based on equation 7.3 with a value for $2K/M$ of 1.95T and a probe moment of $9 \times 10^{-11}\mathrm{Am}^2$.

The value for $2K/M$ is that expected for the ferrite material[3]; the moment value was chosen to fit the data. With an estimated particle radius of 10μm and a value of $\mu_0 M_{\rm sat} = 0.3T$ for the ferrite, the expected moment value is 10^{-9}Am^2, an order of magnitude greater. The size estimate will be uncertain and cantilever force constants can vary greatly from that specified. The form of the model does, however, fit the data. A simpler model by Zhang et al. [8, 9] features the resonant frequency going as the square root of field with no mention of anisotropy and the rate of frequency increase does not drop off as fast as is observed.

The behaviour shown in figure 7.9 (a) is typical of the behaviour of cantilever frequency with field when efforts had been made to align the particle moment perpendicular to the cantilever plane. A different trend was observed in instances when the moment was initially confined to the plane of the cantilever, an example of which is shown in figure 7.9 (b). The particle on the cantilever was a small piece of a magnetic multi-layered recording media sample, fixed flat to the cantilever. The frequency behaviour is dramatically different. It has the same form, however, as measurements and theory by Miller et al. [88] on cantilevers with in-cantilever-plane magnets on their ends. In the figure shown, the scatter of the graph is worse at high frequency because the frequency was measured by observing the position of the thermal noise peak and a reduction in Q at higher fields widens the peak hence increasing the uncertainty in the measurement. The cantilever was made from silicon. The difference in behaviour provides a simple confirmation that attempts to align probe moments in a preferred direction were at least partially successful. Although the behaviour of the cantilever frequency is different for the two different tip magnet orientations, they both show that the field dependence of cantilever frequency is less severe at high fields, which is a distinct experimental advantage.

As well as changes in the cantilever resonant frequency, variations were also measurable in the cantilever position as the field was changed. Figure 7.10 shows the interferometer output as a function of field for a different silicon nitride cantilever with ferrite on the tip. The fringe pattern shows that the tip has moved a total of about 3.8 microns as the field is swept over 4T. The drop off in the fringe envelope amplitude is due to changes in the coupling of reflected light back into the fibre, due both to the increasing distance and the changing angle of the cantilever with respect to the fibre. The distance the tip moves, and therefore the force on the tip, is not linear with field. This suggests that the displacement is due to a torque on the ferrite

[3]G. M. Smith, private communication

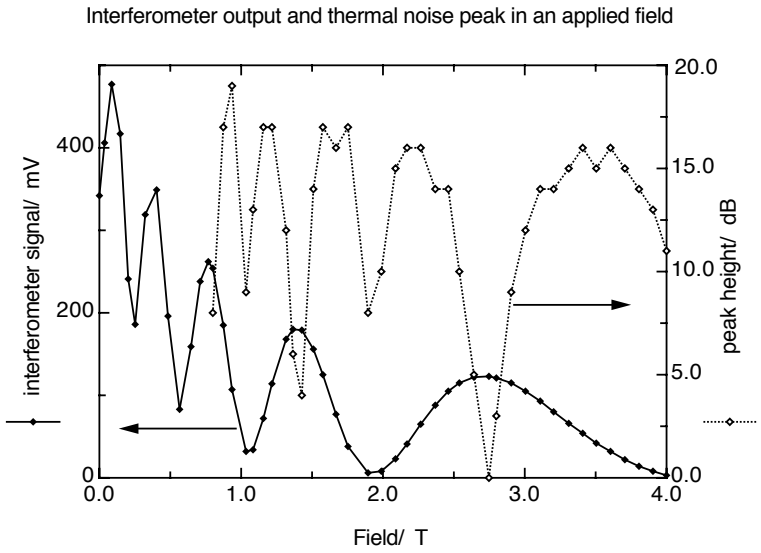

Figure 7.10: Interferometer fringes and thermal noise peak height for a SiN cantilever with ferrite mounted as a function of applied field. Although the scatter on the thermal noise peak measurements is quite large, its relationship to the dc fringes is obvious.

particle and that as the tip position changes, the axis of the ferrite moment becomes more parallel to the field direction. As well as the interferometer fringes, figure 7.10 also shows the height of the cantilever thermal noise peak as a function of field, which was simply the peak height with the noise floor subtracted from it. This clearly varies at twice the frequency of the fringes and is a maximum at the middle of a fringe, as expected. The measurement is simply of the power in the cantilever vibrations, so the phase change of the vibration is not reflected in the figure.

7.3.2 Spurious cantilever response

When FDMR experiments were performed (results discussed in section 7.4) it was also noticed that coherent vibration signals were detectable at the mm-wave modulation frequency even at fields far from resonance. This was observed primarily when amplitude modulating the mm-waves but also (at much lower levels) when frequency modulating. This was thought to be due to heating effects arising from the absorption of some of the incident radiation by the highly doped silicon cantilevers. This idea is supported by a measured orientation dependence of these spurious signals which may be seen in figure 7.11.

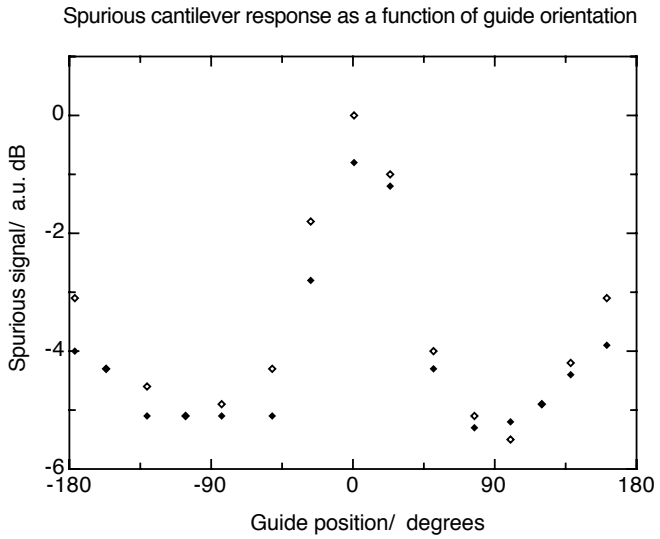

Figure 7.11: Spurious cantilever excitation due to the amplitude modulation of millimetre wave illumination, as a function of the waveguide orientation with respect to the plain of polarisation of the millimetre waves. The signal is normalised to its peak value. Two data sets are shown to indicate repeatability.

Figure 7.11 shows that the spurious signal due to the millimetre-wave peaks when the cantilever axis lies parallel to the plane of polarisation of the illuminating radiation, with peaks in response at 0° and 180°. The two data sets show that despite the scatter, the trend is repeatable. It is likely that the waveguide was not hanging exactly vertical so changes in the coupling of the free space beam to the mode in the corrugated guide would account for the difference in the size of the maxima. Similar excitation in FM schemes was due to FM to AM conversion due to standing waves in the systems: as the frequency changes, the standing wave pattern changes, resulting in an amplitude change. In FM experiments there will also be a small AM component produced by the bias voltage modulation used to frequency modulate the diode but for small modulation voltages this was not visible. The standing wave component may be reduced by adjusting the height of the quasi-optical system above the corrugated waveguide to select a turning point in the standing wave pattern.

The spurious excitation was also observed (although at a much lower level) in silicon nitride cantilevers with a gold coating, where a bi-metallic effect is probably responsible. Very recent experiments with uncoated SiN cantilevers saw none of these effects. Modulating the magnetic field, as in conventional ESR, was found to cause huge spurious signals. Even if the cantilever had no magnet on it, the modulation coil will

vibrate when in a magnetic field and the system is so sensitive to vibration, especially at the cantilever resonant frequency.

7.4 FDMR spectra of $(FA)_2PF_6$

This section shows some of the FDMR spectra obtained using the first cantilever mount. The mm-wave frequency for these experiments was around 93.5GHz. Both amplitude and frequency modulation schemes were employed. The cantilevers used with this mount were all highly doped silicon probes from Nanosensors. Various signals were obtained the best of which are presented here. The repeatability between different experiments was found to be poor. This was because the sample decayed significantly in a matter of days when kept at room temperature. The probe magnets also varied in size and shape and, although efforts were made to align the axis of the probe moments perpendicular to the cantilever axis, there were always effects of the field on the cantilever frequency that suggested that this alignment was not ideal. With the preliminary mount, positioning of the cantilever relative to the sample was by means of a screw adjusted by hand.

Figure 7.12 (a) shows a spectrum recorded with 100% amplitude modulation, with the cantilever operating in air. The line for the AM spectra is much broader than the ESR line recorded at the same time and included for comparison. This is as expected and is due to the gradient created by the probe magnet. The ESR line also shows a small feature about 5×10^{-4}T above the main transition. This is probably caused by a small piece of broken single crystal at a different orientation to the main piece. The two peaks of the ESR line differ in size, due to the phase of the signal and they are 2.4×10^{-5}T apart. The peak height is 34 times the root mean square (rms) of the baseline noise level, yielding a peak signal to noise ratio of 31dB. The cantilever Q was about 30 and the resonant frequency was 6.3kHz. The width of the line (distance between the two half maximum values, allowing for the offset) is 3.7×10^{-4}T.

Figure 7.12 (b) shows a frequency modulated spectrum. The shape of the integral of this spectrum is very similar to the AM modulated spectrum, which it should be provided the modulation of the Gunn diode frequency is small. The modulation used for this experiment was $8\mathrm{mV}_{\mathrm{p-p}}$, corresponding to 2 MHz. The Gunn diode frequency was a fairly linear function of bias voltage in its operating range, so it was

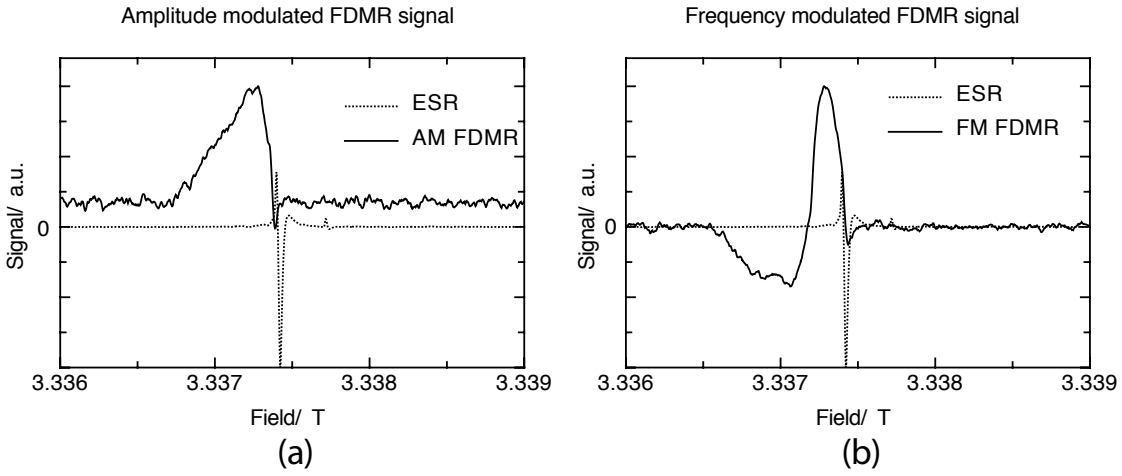

Figure 7.12: High field force detected ESR spectra at 93GHz obtained using (a) amplitude modulation and (b) frequency modulation. The accompanying ESR spectra shows that the force detected lines are much broader. The spectra are normalised and displayed in arbitrary units, but share the same zero. These experiments were carried out in air.

straightforward to relate bias modulation to frequency modulation with a voltage to frequency conversion of 280MHz per volt. The signal to noise for the FM spectrum is slightly better than the AM case at 35dB, with the peak value 59 times the rms noise value. Both spectra used a one second time constant. The distance between the minimum and maximum is 2.4×10^{-4}T. There is no reason to expect this to agree with the width of the AM line. The width of the integral of the FM signal is also 3.7×10^{-4}T. This width should agree with that measured for the AM line.

Figure 7.13 shows one of the best FDMR spectra obtained, again with frequency modulation. This was taken in a separate experiment with the cryostat evacuated to 10^{-2} torr and the cantilever Q was 3100 at a field of 3.3T. The frequency modulation used was 28MHz. The signal to noise ratio in figure 7.13 is 55dB. The line is much closer to being symmetrical than that in figure 7.12 indicating that the probe magnet is further from the sample surface, but it may still be seen that the high field side of the signal rises back to zero more steeply than the low field side. This is more obvious when the signal is integrated after first having a baseline level subtracted from it. The field separation between the peaks is 10^{-4}T. There is obviously more FM to AM conversion than in the other FM spectrum as evidenced by the high offset. However, because this level is constant, it doesn't adversely affect the signal

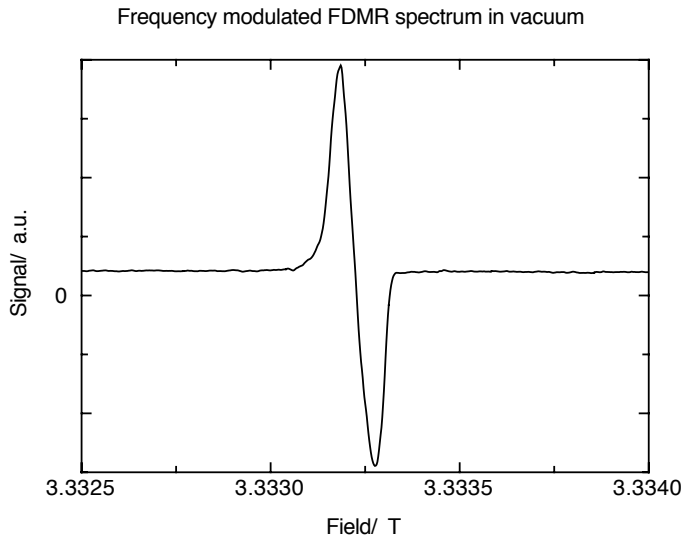

Figure 7.13: Force detected ESR spectrum of (fluoranthene)$_2$PF$_6$ taken in a vacuum of 10^{-2} Torr with a cantilever Q of 3100.

to noise. The symmetry of the line about the x axis shows that any signal effects due to amplitude modulation are small compared to those for frequency modulation. This is verified by the fact that the integral of the line returns to zero after the peak.

The above has presented some of the first high field FDMR spectra. They will be discussed in further detail in chapter 9.

Chapter 8

Towards a high field magnetic resonance force microscope

The main goal of the MRFM project was to produce an instrument that could be used to provide images of the spatial distribution of unpaired electron spins in a sample of interest. It was decided to construct the instrument around a commercially available scanning probe microscope, so the emphasis could be put on the force detection of the magnetic resonance rather than the necessary apparatus to scan the probe. This chapter describes the chosen system and its development into a magnetic resonance force microscope.

8.1 The scanning probe microscope system

The system chosen as the basis of the MRFM was an Oxford Instruments CryoSXM 35 scanning probe microscopy system. This is a sophisticated instrument for performing SPM at low temperatures (down to around 2K). This section describes the CryoSXM and the associated instrumentation that goes with it.

8.1.1 The CryoSXM 35

The core of the instrument is the CryoSXM head. This is a compact cryogenic scanning probe microscope based around a 60mm by 13mm piezoelectric tube operating

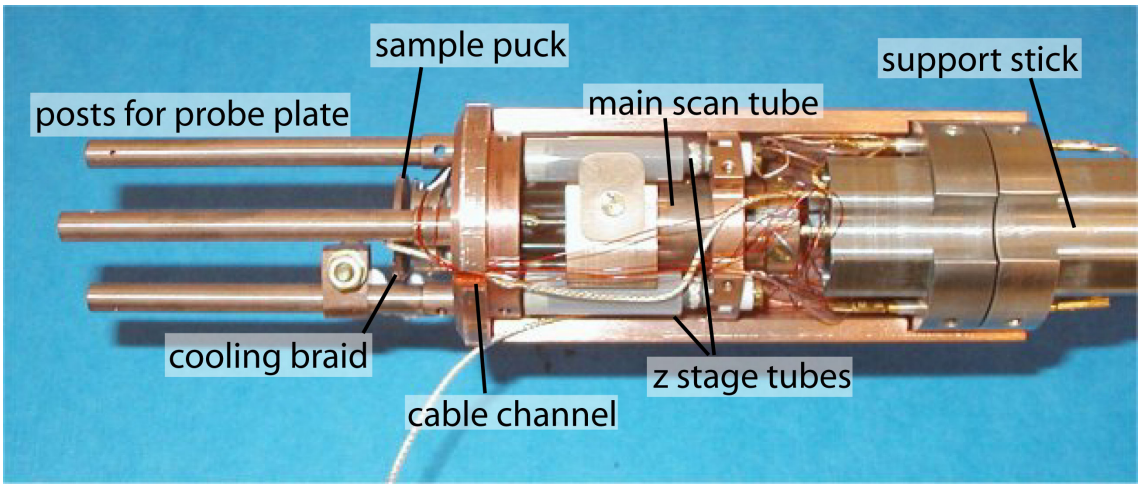

Figure 8.1: The CryoSXM 35 probe head with one half shell removed, showing the main scan tube and the coarse z stage.

on the principle mentioned in section 1.2.2.2. The head itself is made from two copper half shells and is 35mm in diameter and 95mm long and is shown in figure 8.1. The two shells hold the instrument together, attaching to a plate at the top for connections, the z drive halfway down and the plate at the bottom. From the bottom of the head protrude three phosphor bronze posts, 80mm long by 4mm in diameter, in an isosceles triangle. These posts are for mounting the baseplate on which the probe holder (e.g. an STM tip, AFM cantilever etc.). may be mounted. The SPM scans the position of the sample relative to that of the probe, so the sample moves during a scan. This will mean that the spurious excitation of the cantilever probe due to the SPM will be less (though still considerable) than if it was the probe that moved. The probe itself (by default an STM) sits on a baseplate below the sample puck. The plate slides onto the three support posts and its position is adjustable, held in place by grub screws.The tube itself provides a scan area of 35μm $\times$ 35μm at room temperature, reducing to 8μm $\times$ 8μm at 4K. At room temperature, the main tube can provide a z movement of $\pm 2\mu$m. Larger displacements in the z direction may be produced using the coarse z drive. This uses a set of three small piezoelectric tubes inside quartz tubes to move the entire main tube. The main tube is held against the quartz tubes by three springs. To move the main tube, the small piezos in the z drive extend by a small amount and so move the tube. The small piezos then quickly snap back to zero displacement and the friction between the quartz tubes and the springs is insufficient to move the main tube, so it stays where it is. This is known as a “slip-stick” or “stiction” drive and has a very large range, of the order of 20mm.

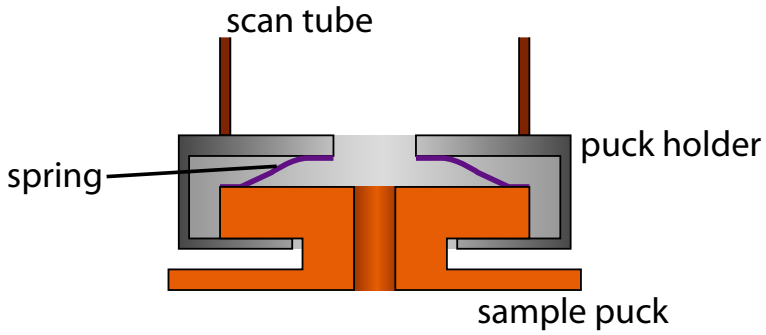

Figure 8.2: Schematic of a section through the puck holder at the end of the scan tube, showing how the spring keeps the sample puck in place within the holder. (Not to scale.)

The instrument was intended to be used at low temperatures in a magnetic field. To this end, the head is mounted on a stainless steel support stick through which the cabling for the SXM head is carried. The head is separable from the stick and uses sprung pins to connect the head to the wires. The stick carries wires for the main scan tube, the z stage and an integral temperature sensor. Notches in the bottom plate of the SXM allow for the passage of wires from underneath the scan tube. By removing a cover on the SXM, it was possible to run wires through under the cover and out onto the support stick. The fit of the SXM to its cryostat was too close to allow any wires outside the SXM. Connections to the system are made at the top plate of the system. Spare connectors with corresponding wires are made available for custom requirements, such as driving a small coil as discussed in section 8.4.

The sample mount is a small copper puck which sits in a holder on the end of the scan tube as shown in figure 8.2. The holder has a 3mm hole in the bottom which allowed for the waveguide necessary for the illumination of the sample. The sample puck is made from copper for its thermal properties and is held in place by a beryllium copper spring on the back. A hole to fit the flexible guide described in section 8.2.1 was drilled through the centre of the puck. The puck holder is over-sized to allow coarse lateral movement of the puck. This is done again using a slip-stick technique, hence the requirement for the spring on the puck. The coarse xy movement is a millimetre in each direction, but will be reduced by the need to accommodate the waveguide, again as discussed in section 8.2.1. As the sample puck is isolated from the copper body of the SXM, it is cooled by means of a copper braid clamped to one of the probe support legs.

8.1.2 Temperature and system control

In order to perform experiments at low temperatures, the system had to be housed in a cryostat. The cryostat was of the *continuous flow* type. Liquid helium is transferred into the cryostat where it boils and the cold gas is drawn over the experiment to be cooled. In this system, the liquid enters the top of the cryostat via evacuated pipes and enters the cryostat sample space at the bottom. Pumping on the sample space draws the helium through. Because we want to perform our experiments in a vacuum as well as at low temperatures, a vacuum vessel went inside the cryostat and the SXM went into the vacuum vessel. The bottom of the vacuum vessel was a good fit to the SXM and made of copper. The bottom plate of the SXM had a short conical section which mated with a similar section in the vacuum can for good thermal contact. Thus, the vacuum can is cooled directly by the flow of helium and the SXM is cooled by its contact with the can walls. As well as the temperature sensor in the SXM head, there was one in the cryostat, along with a small heater. An external control unit governed the temperature by controlling the heater current. The top of the vacuum can had a short bellows section built into it to allow for the thermal expansion and contraction of the SXM support stick.

Control of the SXM was accomplished using a computer along with a dedicated control system, known as the TOPS system. The TOPS system contained the necessary hardware to drive the Cryo SXM and detection electronics for STM experiments. It also contained auxiliary programmable analogue to digital (ADC) and digital to analogue (DAC) converters. This was provision to use our interferometer signal, as well as to control external parameters, such as the magnetic field.

Vibration control was also important. Cantilever based signal detection is inherently extremely susceptible to vibrational noise. Initial isolation of the SPM system was by suspending it on rubber bungee cords inside a metal frame. For experiments in the magnet it was supported on a polystyrene collar that raised the sample position in the SXM to the field centre position. The suitability of this could be assessed by striking the magnet dewar casing and verifying that vibrations weren't transmitted to the SXM head by looking at the interferometer signal. A set of vibration damping legs (of the kind used to support laser tables) have been obtained and these will ultimately be used to support the SXM system clear of the magnet, so the experiment will be mechanically isolated from the magnet and the rest of the lab. The system is supported by a set of bladders of compressed gas and position sensitive valves regulate

its vertical movement.

8.2 Integration of microwaves with SPM

An important part of any spectroscopy system is the ability to illuminate the sample and this presented a significant technical challenge. Most MRFM experiments use small coils or micro-strip resonators at the sample and the microwaves may be delivered to the resonator with high quality coaxial cables. This approach, however, is not practical at the frequencies considered herein, so another approach is required. This section describes the design of the various microwave components used with the Cryo SXM.

8.2.1 SXM waveguide

Implementing a quasi-optical transmission line within the SXM would have required a deal more room than was available. Thus, the only remaining options were either hollow metal waveguide, or some kind of solid dielectric waveguide. The latter is attractive for its low loss properties, but the guiding is weak so there would be issues with the millimetre-wave power being inadvertently coupled out by close contact with wires and any supporting mechanism inside the SXM support stick. This leaves metal waveguides. Single mode guides at W band (70GHz to 110GHz) can be quite lossy, but there was insufficient room in the SXM support stick for an overmoded guide, as although the stick had an internal diameter of 20mm, it narrowed to 8mm near the probe head. The wires emerging from this end of the stick congest it further, so only around 4mm of space is available. The best solution would have been single mode W band guide, but commercially available guide is typically made from extruded copper and the thermal conductivity would be far too high to use with a helium cooled system. Stainless steel guide is available but very lossy, so the route taken was to use a thin walled nickel silver pipe. This is far from ideal, but the losses would be lower than with stainless steel and it was conveniently available with an inner diameter of 2.85mm and a wall thickness of 75μm[1].

The nickel silver waveguide was sufficient to deliver the mm-wave radiation to the

[1]Goodfellow Ltd., Huntingdon, UK

SXM, but getting it to the sample was a more subtle problem. As described in section 8.1, the scanning mechanism in the SXM is based on a tube of piezoelectric material which deforms while scanning. Since the sample is mounted on the end of the tube, the waveguide will have to pass through it. This raised two problems: the hole in the bottom of the scan tube through which the waveguide had to pass was only 3mm in diameter. The outside diameter of the waveguide at this point would have to be less than this to allow advantage to be taken of the large area coarse scanning feature of the Cryo SXM. The waveguide was to be supported at the top of the scan tube by a flange fixed to the scan tube and a rigid guide would interfere with the scanning deformation of the tube. To solve this, it was decided to use a guide made in two sections: a long section of nickel silver pipe and a shorter flexible section to pass through the scan tube. A corrugated guide was designed with a diameter of 3mm and

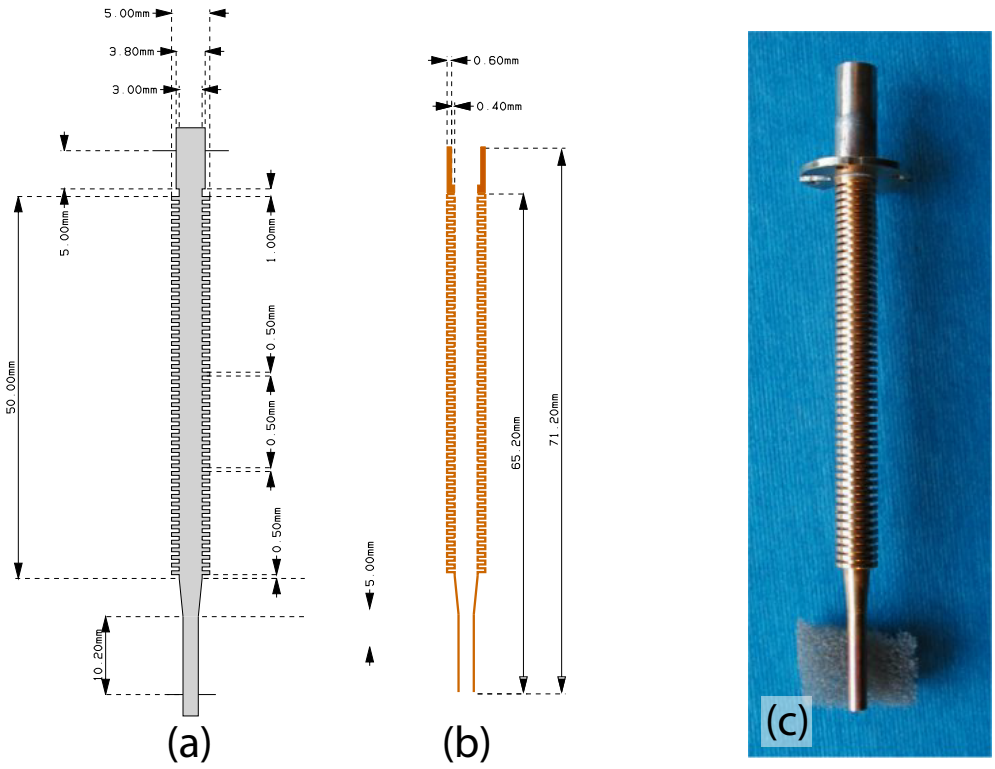

Figure 8.3: The flexible waveguide to pass through the SXM scan tube. (a) The aluminium mandrel on which the guide is formed. (b) The guide itself. (c) The actual electroform, with nickel silver collar and top flange attached.

corrugations to a depth of 1mm beyond this. The design may be seen in figure 8.3 along with the finished flexible guide. The top of the corrugated section would be fixed by a flange to the top of the scan tube and accept the lower end of the nickel silver

guide. The corrugated region was 60mm long. Following this was a 5mm section that tapered in inner diameter from 3mm to 2mm. This was to allow sufficient clearance through the hole in the bottom of the scan tube to allow some lateral movement of the bottom end of the guide. The 2mm diameter portion of the guide was 13mm long so that it would pass through the sample puck and emerge almost flush with the face of the puck. The small diameter was quite close to the cutoff size (the size below which the guide won't allow the radiation to propagate) for 94GHz (1.8mm) but the loss over only 13mm would not be large. The flexible section and taper were electroformed[2]. This involves the manufacture of an aluminium mandrel (produced in house) the shape of the required interior of the guide. Copper is then plated onto the mandrel and the aluminium is removed by etching it out with acid. This allows the design of components that would be non-trivial to machine. The copper layer was made as thin as it was thought would allow for reasonable strength, and the finished wall thickness was 100μm for the flexible section and 220μm for the 2mm section at the bottom end, allowing lateral movement of the sample puck of up to $\pm$230μm. Since the thin walls follow the bellows shape of the mandrel, the guide was very flexible, easily allowing millimetres of movement over its length, much more than was required. The slip-stick action of the puck means that we want to keep any lateral friction generated by the guide to a minimum.

The wide temperature range over which the SXM system may be used means that thermally induced dimension changes can be significant. The change in length of the CryoSXM system is accommodated in the bellows section at the top of the vacuum can, but the waveguide inside it will also change length. The main scan tube can also move a large distance with the coarse z direction travel, so the end of the nickel silver guide had to form a sliding fit with the flexible section. The different thermal expansions of the different metals could lead to sticking, however, so a nickel silver sleeve to accept the 3mm waveguide was soldered to the flexible copper section, and the flange to fix to the top of the scan tube was in turn soldered to the sleeve.

8.2.2 Millimetre wave window

Above the top plate of the SXM is a copper window which forms a sliding seal with the pipe that emerges from the SXM top plate. As it came the window was empty,

[2]Waveform Electroforming Ltd, Norwich, UK

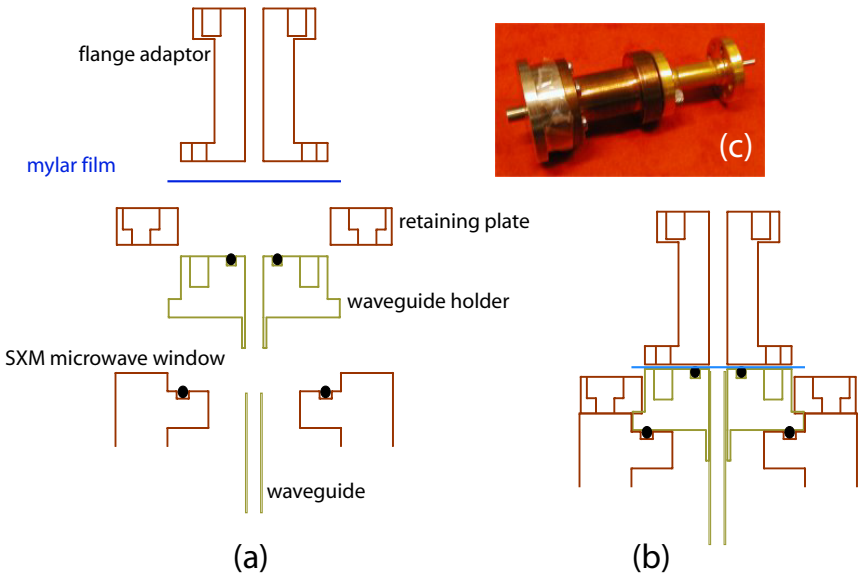

Figure 8.4: The fitting for the waveguide vacuum feed-through. (a) and (b): The main parts and how they fit together. (c) The fitting with the rectangular to circular transition attached.

so components had to be designed to allow microwaves into the vacuum can. The required fitting would have to transmit the millimetre waves but be vacuum tight and also had to mate with the top of the nickel silver waveguide. The fitting was made in two parts, as shown in figure 8.4. The lower part, made of nickel silver, sat in a recess in the microwave window and sealed against it with an "O" ring. This piece was milled to accommodate the top of the waveguide in a tight push fit. It in turn was held down by a clamping ring which bolted to the top of the window. The second part was a copper flange adaptor which sealed against the waveguide holder by means of an "O" ring set into the waveguide holder and a small sheet of 10μm mylar film. The flange adaptor was screwed to the waveguide holder and butted up against the end of the waveguide with the mylar between. The adaptor had a hole to match the 2.85mm inner diameter of the waveguide and the top was drilled out to mate with a UG/387 flange. An electroformed WR10 rectangular to 2.85mm round waveguide transition allowed connection of the system to a standard single mode waveguide.

8.2.3 SXM waveguide performance

After completion, characterisation of the waveguide was required. The expected losses were quite high. For the TE_{nm} mode propagating in a circular guide, the attenuation constant, α, is given by [89]

$$\alpha = \frac{R_m}{aZ_0}\left(1 - \frac{k_{c,nm}^2}{k_0^2}\right)^{-1/2}\left(\frac{k_{c,nm}^2}{k_0^2} + \frac{n^2}{(p'_{nm})^2 - n^2}\right) \tag{8.1}$$

where Z_0 is the impedance of free space (equal to $\sqrt{\mu_0/\epsilon_0} \approx 377\Omega$), a is the radius of the guide, k_0 is the free space propagation constant ($= 2\pi/\lambda$) for the millimetre waves, k_c is the cut-off propagation constant and p' is a constant depending on the mode. We will be using the lowest frequency propagating mode, the TE_{11} mode. R_m is the skin effect surface resistance and will obviously be frequency dependant:

$$R_m = \left[\frac{\omega\mu_0}{2\sigma}\right]^{-1/2} \tag{8.2}$$

where ω is the radiation frequency and σ is the conductivity of the guide material. For the TE_{11} mode, the expression for loss becomes

$$\alpha = \frac{R_m}{aZ_0}\left(1 - \frac{3.389}{k_0^2a^2}\right)^{-1/2}\left(\frac{3.389}{k_0^2a^2} + 0.4185\right) \tag{8.3}$$

in units of Npm^{-1} which may be converted to dBm^{-1} by multiplying by $10\log_{10} e^2$ (≈ 8.686).

Assuming that the various transitions from one part of the guide to another are perfect, the loss expected for the nickel silver guide together with the flexible guide was calculated to be 8.56dB at 94GHz. The measured loss using a backward wave oscillator at 94GHz for the entire waveguide (rectangular to circular transition, flange adaptor, waveguide holder, nickel silver waveguide and flexible guide) was 9.2dB. This is an upper limit on the loss as there was no transition from the 2mm end of the flexible section to the rectangular waveguide of the power meter and the power meter head guide was simply butted up against the end of the flexible section, so results are indicative only. The above measurement was carried out with the guide supported on a bench. When a similar measurement was performed with the guide installed in the SXM, the minimum loss was measured as 10.3dB. The difference from the previous measurement is almost certainly due to the difficulty in aligning the power meter with

the guide when the guide passes through the sample puck. A separate measurement gave a loss for the flexible part of 0.5dB. This is about double what was expected and the extra losses are attributed to the transitions in the guide.

8.3 Integration of cantilever detector with SXM

The CryoSXM as it arrived was configured for STM so adjustments had to be made to accommodate our detection system. The SPM was to be used primarily as a positioning system with the optical detection being handled by the same detector and amplifier system described in chapter 5 and used in chapter 7. This section discusses the additions made to the CryoSXM.

8.3.1 Cantilever mount design

The SXM came with a mount to hold an STM tip but without a way of accommodating a cantilever and fibre setup. An example AFM cantilever mount was obtained from Oxford Instruments but it was decided that a new mount for fibre alignment and fixing was more appropriate. Here the designs of the mounts intended for use with the SPM are discussed.

8.3.1.1 Mount #2

As described in section 8.1.1, the bottom of the SXM has three posts arranged in an isosceles triangle. Any base plate with suitably drilled holes may be attached. It was decided for simplicity to make the baseplate for the new mount the same shape as the one for the STM probe that the CryoSXM arrived with. This plate is circular, 35×7.5mm with a 11.9mm hole in the middle, with the area around the hole counterbored by 1mm to a diameter of 19mm. This recess accommodated a pillar which sat on top of the baseplate to a total height of 14mm. A 10mm high rectangular piece was located on top of the pillar with dowel pins. The centre of the front of this cantilever post was located over the centre point of the circle and provided a support for the cantilever itself. The top surface of the cantilever post sloped back by 5° as did the top half of the adjacent front face. This was to angle the cantilever slightly

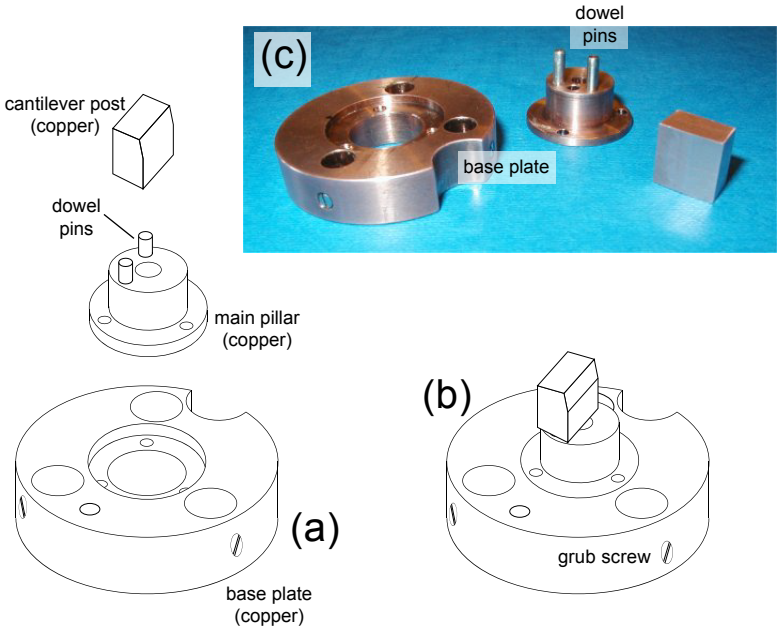

Figure 8.5: Design and construction of cantilever mount #2. (a) Exploded diagram showing the three parts of the mount. (b) How the three parts fit together. (c) The machined pieces of the mount.

with respect to the surface to ensure that the cantilever tip with the probe magnet on was raised clear above the height of the cantilever supporting chip. A semicircular notch taken out of one side of the base-plate allowed cables to pass and a 2mm hole added later allowed for the extraction of the fibre. Figure 8.5 shows the three parts of mount number two along with a diagram showing how they fit together. The original plate had a large number of sockets to accept electrical connection pins, but these were decided to be unnecessary for a cantilever mount. Three brass grub screws in the sides of the baseplate allow the plate to grip the three posts at the bottom of the CryoSXM. The procedure for aligning and gluing the fibre to the cantilever post was very much the same as that for using mount #1 as described in section 7.2, with the slight change that the post had to be held at an angle of 5° so that the fibre would be perpendicular to the cantilever. The dimensions and positions were such that the fibre axis was along the centre line of the system.

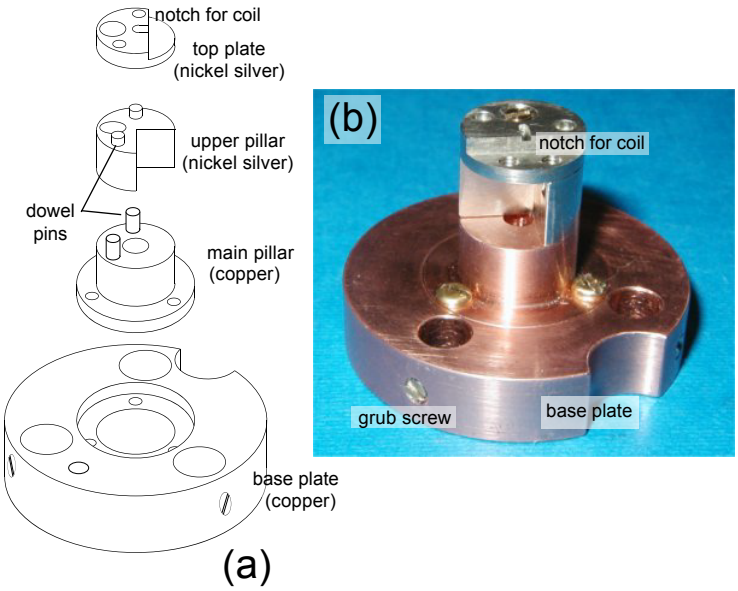

Figure 8.6: Design and construction of cantilever mount #3. (a) Exploded diagram showing the component parts of the mount. (b) The completed and assembled mount.

8.3.1.2 Mount #3

Mount #2 was found to be adequate for what it was designed for, but it was felt that it would be advantageous to have some form of control over the cantilever. This is common in different methods of cantilever based SPM (see, for example, [90]). It was decided to implement this using a small coil. There are two ways to excite the cantilever using the field from a coil: Bruland and co-workers [91] created a torque on the cantilever using a coil with its axis parallel to the cantilever and perpendicular to the moment direction of the magnet on the cantilever tip. This method was tried in a simple experiment, but it was found that positioning the coil next to the cantilever was a non-trivial task. The chosen method used the field gradient of the coil to create an oscillating force on the cantilever. The physics of this is discussed in more detail in section 8.4.1.

For this purpose, it is best if the coil axis is perpendicular to the cantilever axis, i.e. parallel to the moment of the ferromagnetic particle on the cantilever. In order to get the coil as close to the cantilever tip as possible, the coil was to be co-axial with the fibre. This was achieved by winding a coil on a hollow former that could then fit into

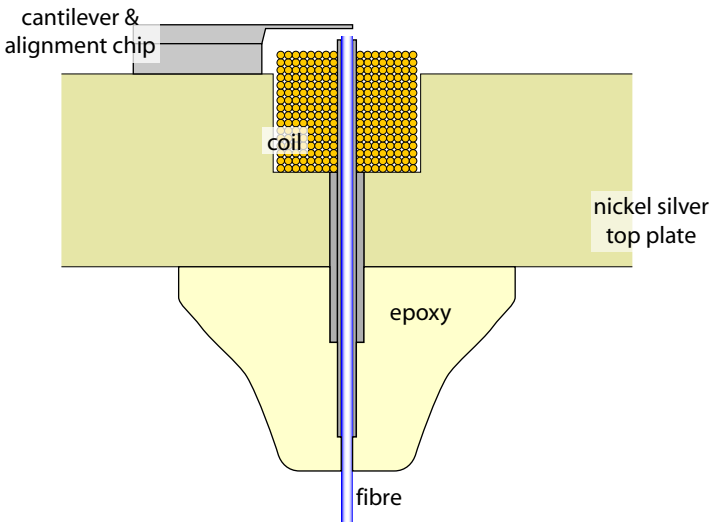

Figure 8.7: Schematic of the arrangement for holding coil and fibre using cantilever mount #3. The diagram is not to scale.

the cantilever mount. As can be seen in figure 8.6, the mount baseplate and main support pillar are the same as for mount #2, but the top piece has a hole in it to take the coil former and the fibre, which pass down through the centre. The baseplate and pillar are again made from copper for its high conductivity, but the upper pillar and top plate are made from nickel silver for its easy machining properties. The notch cut into the top plate near the centre is to allow the extraction of the leads for the coil[3]. To hold the coil in place, a 0.5mm hole was drilled through the centre of the top plate. Inserted into this hole was a piece of stainless steel tube, with an outer diameter of 500μm and an inner diameter of 280μm. This accepted the 250μm former used for the coil, as described in section 8.4. The coil was inserted into the stainless steel guide tube and fixed in place using cryogenic varnish[4]. The varnish is attractive to use as, when diluted with acetone, it may be applied with a small syringe. A cantilever in a Nanosensors cantilever chip was then positioned with its tip above the coil axis, and varnished in place. The mount components were threaded onto the fibre and the cleaved fibre was inserted into the coil former tube. The fibre and the bottom of the coil former were then potted into the upper post of the mount with epoxy adhesive. The slightly lowered ledge in front of the notch for the coil on the top plate provided for the placement of a small printed circuit to allow connections to be made to the

[3]G. M. Smith, private communication
[4]Oxford Instruments, Abingdon, UK

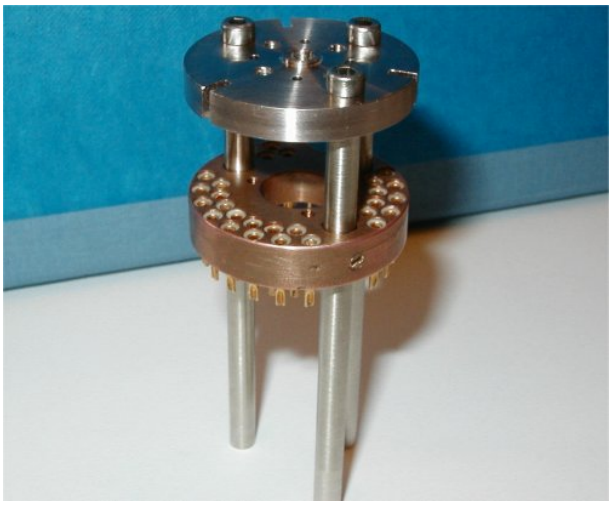

Figure 8.8: Photograph of the waveguide flange adaptor used to enable the use of mounts 2 and 3 with the corrugated pipe and feed-horn as used in chapter 7. The base plate pictured with the adaptor is the original STM probe holder.

fragile wires of the coil.

8.3.1.3 Waveguide flange adaptor

The above deals with the cantilever mount construction. Once they were available it was desirable to use them along with the corrugated waveguide and feed-horn as with mount #1 in chapter 7. To this end, the adaptor shown in figure 8.8 was designed. Made from nickel silver, this device has three legs that allow mounts two and three to attach to it and has holes drilled in the top to mate with the UG/387 flange on the bottom of the feed horn. Using this mount meant, however, that adjusting the sample-cantilever spacing had to be done manually by sliding the baseplate along the legs of the adaptor. This could be amended in the future by adding a second baseplate below the cantilever mount with micrometer drives to push the mount into the required position.

System assembly was a fairly straightforward process. The main concern was the routing of the optical fibre. The loss of the fibre can increase dramatically with tight bends (a radius of around 10mm or less) and there was also evidence that this was worse at low temperatures as described in section 8.3.2. The fibre was installed so as to try and keep the bends in the fibre as shallow as possible. After the fibre emerged from the bottom of the cantilever mount, it was bent back in as large a loop possible

within the confines of the vacuum can (35mm diameter). The fibre then came back up and passed through one of the notches in the bottom plate of the SPM head and was passed under the SXM cover. On emerging at the bottom of the support stick, it was then wound up in a spiral fashion about the stick. It would have been more desirable to take the fibre through the stick with the rest of the wires, but the stick design did not allow for this. A section of 50mm pipe with appropriate flanges was made to house a vacuum pump-out port and a fibre-optic vacuum feed-through as these had been overlooked in the SXM design. The rest of the connections needed for the SPM were accessible via the system's top plate.

8.3.2 Interferometer performance at low temperature

Cooling is an important part of many ESR and FDMR experiments and the highest sensitivities have been obtained by cooling. We were thus keen to conduct low temperature experiments. An interesting trend that has been difficult to explain was a dramatic reduction in the interferometer dc signal when the temperature is lowered. This was noted on all occasions where cantilever experiments were cooled. The dc level, typically several hundred mV, depending on interferometer position, would fall to tens of mV or less. In order to assess whether this was co-incidental, an experiment was conducted in which the interferometer output was recorded as a function of temperature with no cantilever present, i.e. just looking at the reflection from the cleaved fibre end. Although a reduction in the dc level (and hence, in the intensity of the light emerging from the interferometer) was observed, it was only of about 30% of the maximum, compared to the measurements with cantilevers where the reduction was the order of 95%. It is thus difficult to come to a conclusion about the mechanism at work. A possibility is that there is a small temperature dependence of the refractive index in the optical fibre. The fibres were bent sufficiently to observe an increase in their loss, so only a very small change in index would drastically affect the guiding. A second possibility is that air condensing out at low temperatures was lowering the optical quality of the cleaved fibre end, but this would be expected to lead to a noticable effect around the boiling point of air, which was not observed.

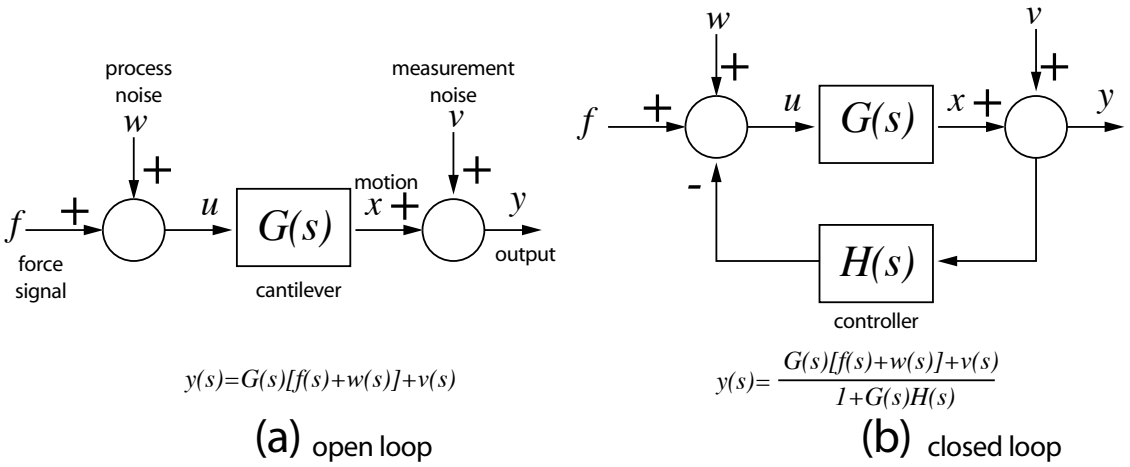

Figure 8.9: (a) Open and (b) closed loop systems with transfer functions as a function of angular frequency $s = j\omega$ where $j = \sqrt{-1}$, taken from [92].

8.4 Cantilever control

As discussed in chapter 3, one of the important contributions to better sensitivity comes from a high cantilever Q. This does also, however, introduce experimental complications itself. The Q of the cantilever is related to the damping time by equation 6.3 so the damping time, τ, may be expressed as

$$\tau = \frac{Q}{\omega} \tag{8.4}$$

Obviously, the larger the Q, the longer the damping time. If we had a cantilever that resonated at 10kHz, say, with a Q of 60,000, then the damping time would be the order of a second. Thus, during an experiment, if the interaction driving the cantilever was changed suddenly, it would take at least this time for the cantilever to respond to the new conditions. This would severely limit the speed that experiments could be carried out at. There is, however, a solution to this problem without degrading the signal to noise ratio, described by Bruland and colleagues [92, 93, 91] which involves applying feedback to the cantilever. This means that one can have the sensitivity benefits of an effective high Q without the longer damping times. Figure 8.9 shows (a) open and (b) closed loop measurement systems [92], where $G(s)$ and $H(s)$ are the transfer functions describing the force response of the cantilever and the response of the controller respectively [93] and the various contributions to the actual and measured signal are shown. $f(t)$ and $w(t)$ describe the actual force signal and process

noise (e.g. thermal and interferometer back-action noise) respectively. The total force on the cantilever is $u(t)$ and the actual response of the cantilever to this is $x(t)$. $v(t)$ accounts for measurement noise (e.g. shot noise at the detector and amplifier noise) and $y(t)$ is the measured output. The expectation values for the mean square of $x(t)$ for the two systems may be expressed as

$$\langle x^2(t)\rangle_{\text{open}} = \frac{1}{2\pi}\int_{-\infty}^{\infty}(S_f + S_w)|G(j\omega)|^2\,\mathrm{d}\omega \tag{8.5}$$

and

$$\langle x^2(t)\rangle_{\text{closed}} = \frac{1}{2\pi}\int_{-\infty}^{\infty}\frac{(S_f + S_w)}{|H(j\omega)|^2} + S_v\,\mathrm{d}\omega \tag{8.6}$$

S_f, S_w and S_v are the power spectral densities of $f(t)$, $w(t)$ and $v(t)$ respectively. The power spectral density S_a of a quantity $a(t)$ is related to the autocorrelation function $R_a = \langle a(t)a(t+\tau)\rangle$ by a Fourier transform:

$$S_a(\omega) = \int_{-\infty}^{\infty} R_a(\tau)e^{-j\omega\tau}\,\mathrm{d}\tau \tag{8.7}$$

and R_a may of course be obtained by an inverse transform of S_a. Note that this is the same process used to recover the SLED coherence from the spectrum as discussed in section 3.3.2. In the two systems above, the signal will be that portion of $y(t)$ due to the force signal $f(t)$ and the noise will be the portions of y due to w and v [92]. If we consider a small bandwidth $d\omega$ at frequency ω then for *both open and closed* systems, the signal to noise ratio will be [92]

$$SNR = \frac{\langle y_f^2(t)\rangle}{\langle y_{\text{noise}}^2(t)\rangle} = \frac{S_f|G(j\omega)|^2\,d\omega}{(S_w|G(j\omega)|^2 + S_v)\,d\omega} = \frac{S_f|G(j\omega)|^2}{S_w|G(j\omega)|^2 + S_v} \tag{8.8}$$

as the denominator in the expression for $\langle y_{\text{closed}}^2(t)\rangle$ will cancel when the ratio is taken. Thus, the feedback introduced does not affect the signal to noise ratio of the system, as described in [92, 93].

As described in section 8.3.1.2 it was decided to attempt controlling the cantilever in force mode, rather than torque mode. The coils used for such a purpose would need to be very small, as in order to ensure that the cantilever chip body did not foul on the coil, the coil radius could not be larger than the cantilever length (in

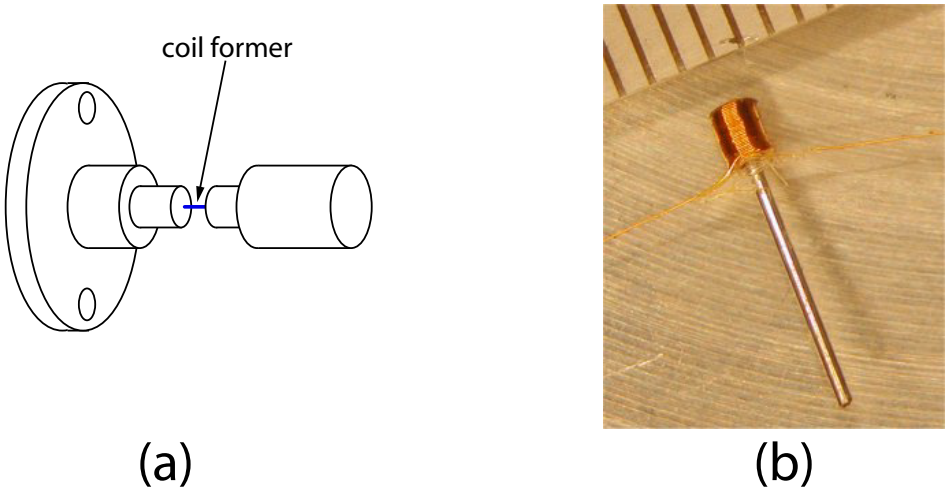

Figure 8.10: (a) A schematic of the PTFE jig used to hold the former for winding miniature coils, and (b) a miniature coil wound on a 250μm stainless steel former. The coil contains 214 turns in 8 layers. The divisions on the ruler are 0.5mm.

this case 450μm). The formers used for the coils were short lengths of miniature stainless steel tube[5] with an inner diameter of 150μm, an outer diameter of 250μm and a 50μm wall thickness. 7mm long pieces of tube were cut by gently sawing with a scalpel blade while taped to a flat aluminium block. Careful cutting was found to be essential. At 125μm, the fibre only has 25μm clearance in the tube and inadvertent scratches rendered the fibre easily broken. A two part PTFE jig was used to hold the former in position on a precision coil winder and to set the end stop points of the coil at 1.05mm long. A former in the jig may be seen along with a finished coil in figure 8.10. The coils were made from 25μm diameter copper wire that had been varnished to a total diameter of 30μm. This wire was extremely fragile, so the coil winder tensioning set-up was critical. Coils were made up of 8 layers of around 30 turns each with diluted varnish applied every second layer. The coil resistance was typically around 13Ω. Once the coil was wound, the excess former was cut as close as possible to one end of the coil and a 100μm drill was used to clean it out. Once the coil was in place on mount #3 and the fibre was installed, a small piece of printed circuit board with two solder pads was used to make connections to external leads. A 4.7kΩ resistor in series with the leads limited the current obtainable with a 15V signal generator to around 3mA to prevent coil damage.

[5]Goodfellow Ltd, Huntingdon, England

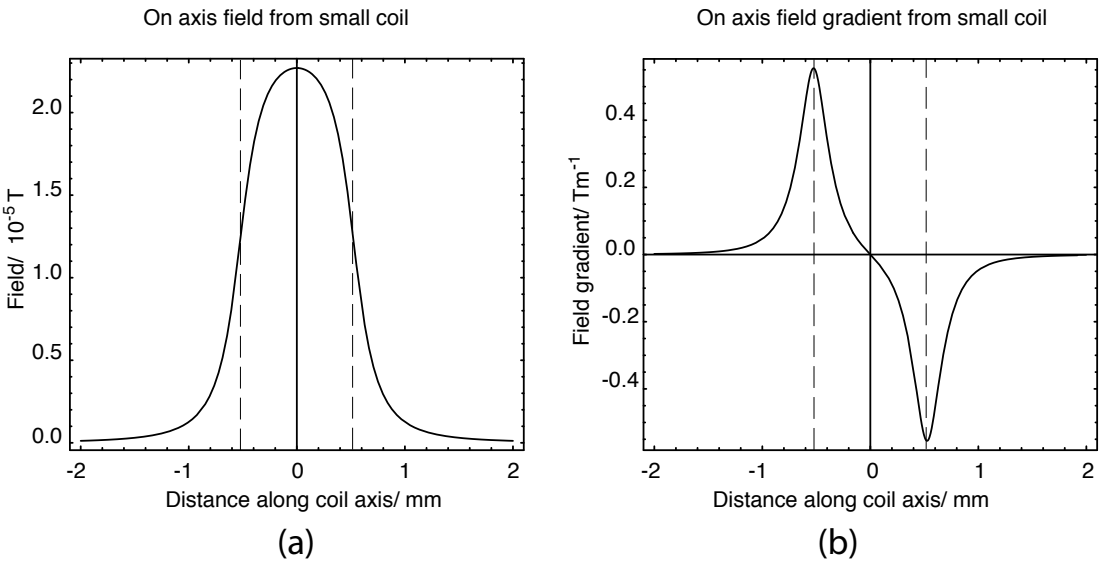

Figure 8.11: (a) The calculated axial field and (b) calculated axial gradient for a coil of the type shown in figure 8.10. For the calculations, the length is 1.05mm, r_1 is 125μm, r_2 is 365μm. There are 2×10^5 turns per metre and the current is 1mA. The dashed vertical lines indicate the position of the ends of the coil.

8.4.1 Field gradient due to the coil

We need to obtain an expression for the field gradient due to the coil in order to know the force that the coil should generate on a given cantilever probe moment. As we are going to be working outside the coil, long solenoid simplifications will not apply. However, we only need to consider the gradient on the coil axis. One may begin with the on axis field due to a finite thin solenoid, given by [78]

$$B = \frac{\mu_0 i N}{4l}\left(\frac{z+l}{\sqrt{(z+l)^2+r^2}} - \frac{z-l}{\sqrt{(z-l)^2+r^2}}\right) \tag{8.9}$$

where r is the radius of the solenoid, z is the on axis distance from the solenoid centre, i is the current, $2l$ is the length and N is the number of turns in the solenoid. Integrating over a range of radii yields an expression for the axial field due to a finite thick solenoid.

$$B = \frac{\mu_0 i n}{2(r_2-r_1)}\left((z+l)\ln\left[\frac{\sqrt{r_2^2+(z+l)^2}+r_2}{\sqrt{r_1^2+(z+l)^2}+r1}\right] - (z-l)\ln\left[\frac{\sqrt{r_2^2+(z-l)^2}+r_2}{\sqrt{r_1^2+(z-l)^2}+r1}\right]\right) \tag{8.10}$$

where n is the number of turns per unit length in the solenoid. In both of the above

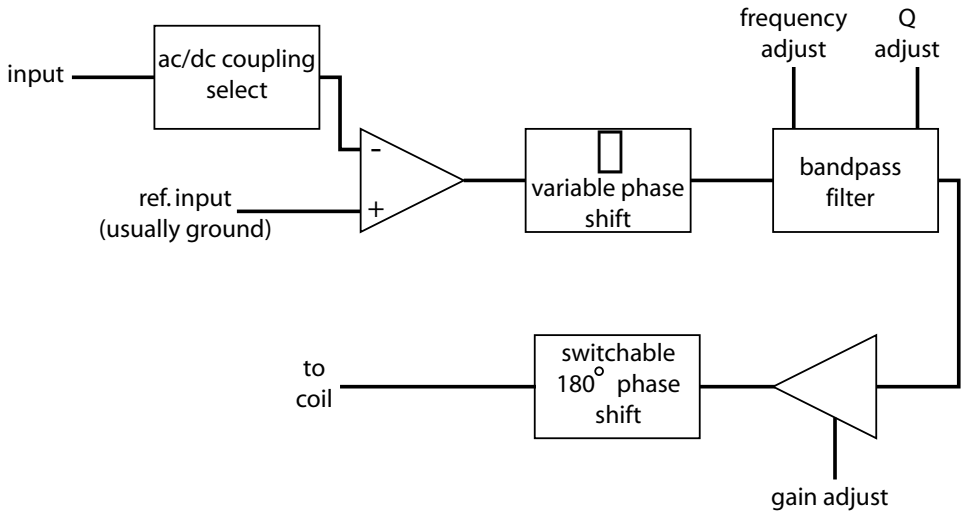

Figure 8.12: Block diagram of the circuit used to provide feedback to the miniature coil with a view to reducing the cantilever Q.

expressions, z is measured from the centre of the solenoid. The function describing the field gradient in the z direction was obtained by differentiating equation 8.10 using the software package Mathematica. The calculated field and gradient for one of these coils are shown in figure 8.11. As can be seen from figure 8.11, the gradient peaks at the end of the coil, so ideally we want the coil to be as close to the cantilever as possible. Sufficient clearance had to be left to ensure that there was no chance of the cantilever fouling on the coil or the end of the fibre. The final distance between the end of the coil and the cantilever was about 170μm, so a 1mA current would give a field of 4.95×10^{-6}T and a gradient of $-0.26\mathrm{Tm}^{-1}$.

8.4.2 Feedback circuit

A feedback circuit was designed[6] to try and apply control to the cantilever through the coil. A block diagram of the circuit is shown in figure 8.12. As can be seen from the figure, the feedback circuit is based around an active filter. The input signal may be ac or dc coupled and the reference input was connected to ground. A capacitor and variable resistor form a variable phase shifter for the input signal. The filter used was a UAF42 and both filter Q and frequency were adjustable. Following the filter was a

[6]G. M. Smith, private communication

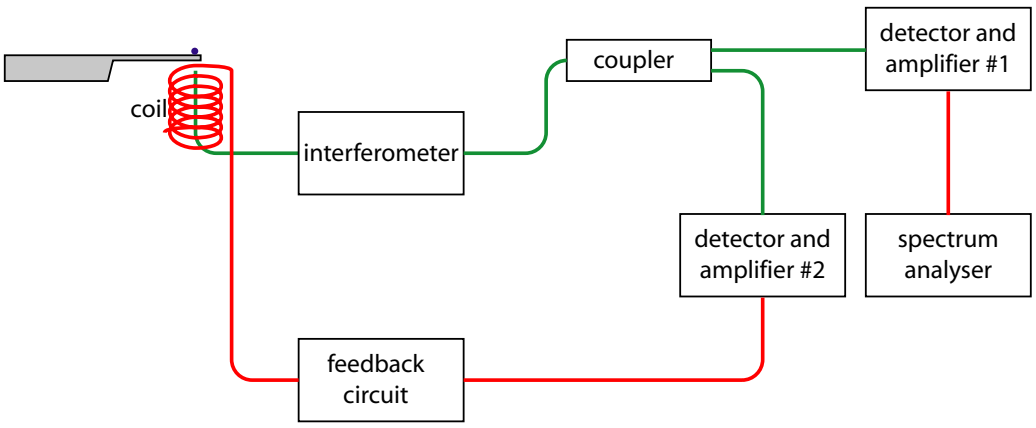

Figure 8.13: Experimental arrangement for trying the feedback system. Red lines indicate electrical connections and green lines indicate optical fibres. Experiments were carried out in air on the bench top as well as in vacuum in the SXM vacuum can.

variable gain amplifier and a circuit to allow the phase of the output to be switched by 180°. The output was connected to the coil through a current limiting resistor. Initial experiments using the coil and circuit with ferrite tipped cantilevers indicated that the feedback circuit interfered with the measurements by the interferometer when the two were connected together, so subsequent measurements used separate detector and amplifier systems: one to provide a signal to the feedback system and a second to allow the cantilever spectra to be measured. A fibre coupler was used to supply optical inputs to both detectors. The experimental arrangement for the measurements may be seen in figure 8.13.

The circuit and coil were found to be very effective in suppressing the thermal noise. The system was prone to oscillation if the output phase was wrong, but this was to be expected and easily remedied using the phase switcher at the output. Figure 8.14 shows two spectra for comparison. The black line shows the thermal noise spectrum of a ferrite tipped cantilever in a vacuum of 4×10^{-2} torr. The blue line shows the spectrum of the same cantilever in the same conditions, but with the feedback operating. The thermal noise signal has been reduced so much that it is no longer visible above the noise floor, a reduction of at least 20dB. Successful results were also obtained in air, but the examples in vacuum are more striking. These results were encouraging and further investigation of this technique could yield large improvements in experiment signal to noise. The integrated coil arrangement used here could also be used for calibration purposes, as discussed in section 6.4. A second coil to excite

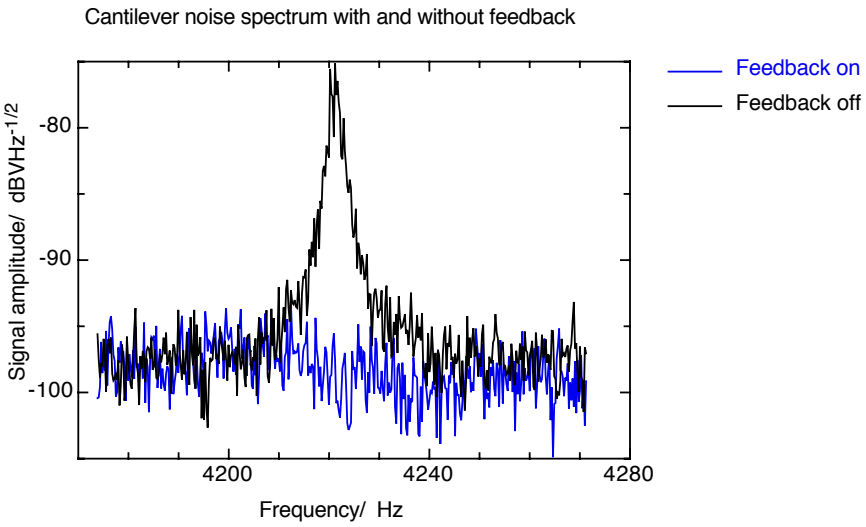

Figure 8.14: Comparison of cantilever thermal noise spectra with and without feedback applied through the coil. The black line shows the thermal noise peak in a vacuum of 4×10^{-1} torr with a Q of about 1600 and the blue line shows the spectrum in the same conditions but with the feedback circuit on and adjusted for the flattest spectrum.

the cantilever while it was subject to feedback would allow measurements to be made on signal to noise ratios.

8.5 Alternative experiment geometries

The experimental geometry for the preliminary experiments with the corrugated pipe involved the probe magnet on a cantilever with the sample nearby and has been described in detail in chapter 7. The same approach was taken in the design for the SXM based experiments but some different arrangements were also investigated. These will be discussed in this section.

8.5.1 Sample on cantilever, probe above sample

This method is similar to that used by other MRFM groups. In our arrangement, however, there was the added complication that we were illuminating with rf from above. Because we wanted the probe moment axis to be parallel with the field axis,

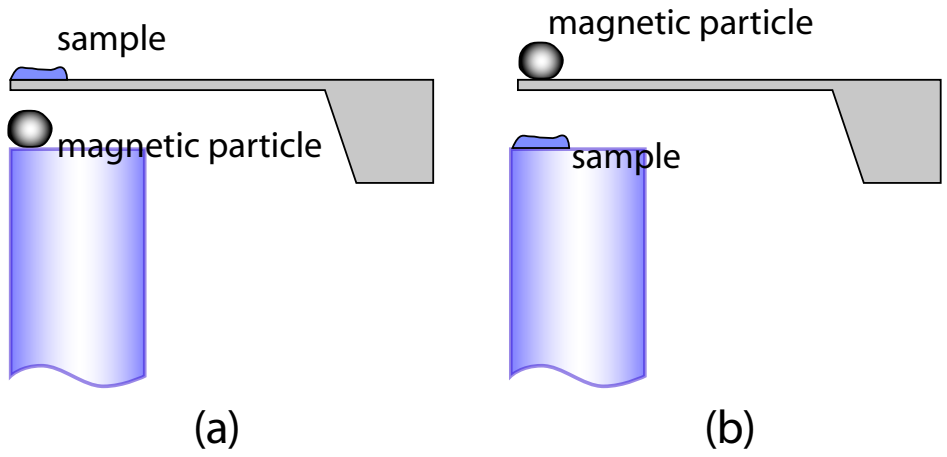

Figure 8.15: Alternative fixed geometries for an FDMR experiment. (a) The sample is on the cantilever and the probe magnet is fixed to the end of the fibre. (b) The probe magnet is mounted on the cantilever, with the sample mounted on the end of the fibre.

the probe magnet has to be above or below the sample. The fibre location precluded the former, so the gradient source would have to be above the sample. Experiments were tried using a piece of ferrite as a probe particle, but were unsuccessful. This could be due to the particle used being too large (the order of 0.5mm) to create a large gradient or to partial shading of the sample from the mm-waves.

8.5.2 Using the fibre to mount sample or probe

These arrangements are similar to that mentioned above, but the end of the fibre itself is used to mount the probe magnet or sample on. This means that the probe will not necessarily obscure the sample from the illumination, however, it obviously does not allow for scanning measurements as the fibre is fixed relative to the cantilever. A schematic of these ideas is shown in figure 8.15.

Figure 8.15 (a) shows the magnet on the fibre and the sample on the cantilever and (b) shows the converse arrangement. Although the available surface area of the end of the fibre is small, because the size of the fibre core is so small (9μm), there is easily sufficient space to mount, say, a 50μm sample or particle. Little glue is needed and the small amounts used were found, with care, to be easily removable with a cotton bud and acetone. This allowed re-use of the same fibre without the

need for re-cleaving, alignment and gluing. When gluing samples or magnets to the end of the fibre, light from a desk lamp was shone into the connectorised end of the fibre, producing a bright spot showing the fibre core at the cleaved end, aiding positioning. Mounting the magnetic particle on the cantilever with the sample on the fibre underneath proved unsuccessful, probably due to shadowing of the millimetre waves, but results with the probe magnetic particle on the fibre were more promising, as discussed in section 8.6.2. The advantage to this technique over that originally intended was that the sample and probe magnet could be more accurately aligned as the cantilever with sample on was placed after the probe magnet was positioned, but only static experiments could be carried out and a certain amount of trial and error was required to get a magnetic particle that would not foul on the cantilever.

8.6 FDMR results with the Cryo SXM

This section presents some representative FDMR signals obtained using the CryoSXM. We took signals with both $(FA)_2PF_6$ as before and DPPH. The experimental details for each will be described as they used slightly different experimental setups.

8.6.1 $(FA)_2PF_6$ signals with SXM

These measurements used SiN cantilevers 200μm long with a nominal force constant of 0.12Nm^{-1}. The probe mounted magnet mounted on the end of the cantilever was a piece of commercial ferrite, with a higher magnetisation than the Ferroxdure used earlier. The sample was mounted on a piece of borosilicate glass attached to the face of the sample puck with Oxford Instruments varnish. Figure 8.16 shows a selection of signals obtained during the same experiment at different SXM scan tube positions. Data set 1 was recorded first, then the sample was retracted from the probe by 200μm for data set 2, before moving forward by 100μm for data set 3. Spurious excitation noise in the form of a baseline offset is visible in all three results. The rms variations of the baseline are all similar as they were all recorded with a one second time constant. Signals one and three both have a peak separation of 10^{-4}T and peak signal to noise ratios of 31dB and 30dB respectively. The difference in the positions of the lines is probably due to drift in the Gunn diode frequency between scans. The experiment was conducted in air.

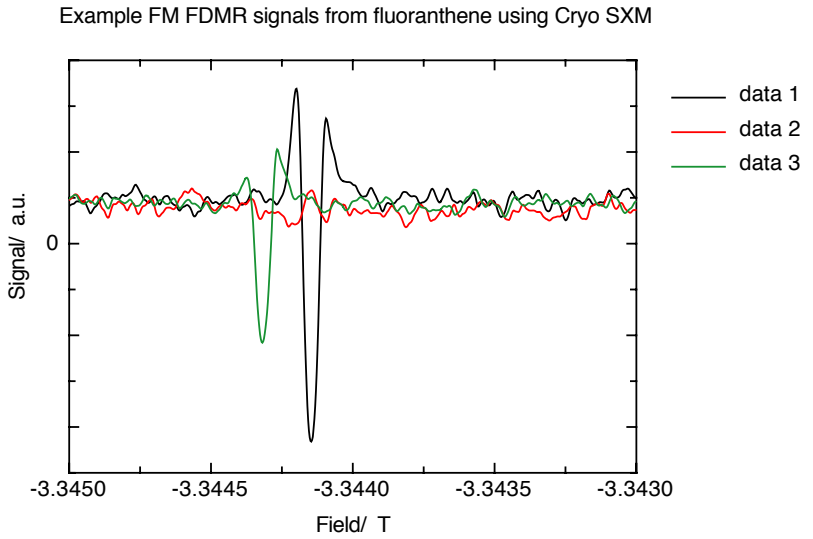

Figure 8.16: Frequency modulated FDMR signals obtained with the Cryo SXM system. The three data sets were taken during the same experiment. Note that the experiments were carried out with the field in the opposite direction compared to others, so the magnitude of the field increases from right to left.

8.6.2 DPPH signals with SXM

Our FDMR experiments have so far used $(FA)_2PF_6$ due to its ease of saturation and the possibility of carrying out experiments at room temperature. However, if MRFM is to be generally useful, it is desirable to conduct experiments at low temperature primarily to manipulate τ_1 and also to reduce the thermal noise. $(FA)_2PF_6$ is not a suitable sample for low temperature experiments, however, due to a phase change at around 160K. We thus opted to use DPPH. For this experiment, we used one of the alternative geometries described in section 8.5.2 and mounted the sample on the cantilever and the probe magnet on the end of the fibre. The arrangement may be seen in figure 8.17.

Because the gradient source was mounted on the fibre rather than the cantilever, it did not matter to the cantilever Q if it was a conductor or an insulator. This allowed the use of an iron particle which, with a saturation magnetisation of $\mu_0 M = 2.1$T offered higher gradients than the ferrite. A DPPH sample about 120μm $\times$ 70μm and 8μm thick was glued to a 170μm SiN cantilever with a nominal force constant of 0.1Nm^{-1}. This cantilever actually had its own integrated magnetic (Co) tip leading to a dependence of frequency on magnetic field but was used because its slightly

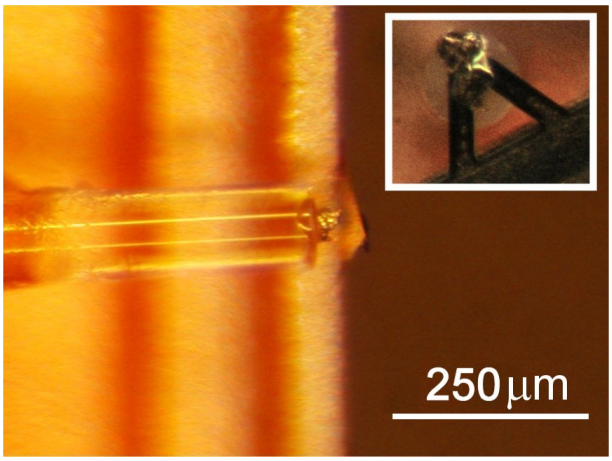

Figure 8.17: Photograph showing an iron particle mounted on the end of the optical fibre, below a SiN cantilever with a piece of DPPH mounted on the end. The inset shows a view of the arrangement from above.

thicker supporting chip allowed greater flexibility in the size of the magnetic particle glued to the fibre. The effect of field on frequency was, however, small.

A typical signal from DPPH taken at a temperature of 5.6K may be seen in figure 8.18. The linewidth is 4×10^{-4}T, compared to 2×10^{-4}T as measured at 90GHz in reference [51]. The spectrum was recorded with a one second time constant and the peak signal to noise ratio is 23dB. The experiment was carried out in helium at a pressure of 0.6Torr. One of the limitations discovered in the use of the flow cryostat system was that in order to allow the SXM itself (as opposed to the flow cryostat) to reach low temperatures it was necessary to introduce helium gas into the SXM vacuum can as the conduction through the copper bottom of the can alone was insufficient to bring the SXM below about 20K, even with the flow cryostat sample space at 5K. The procedure therefore was to pump out the SXM vacuum can before cooling started to remove air and water vapour and once the cryostat reached 10K or so to introduce some helium into the vacuum can. This will have meant that the Q of the cantilever suffered. By pumping sufficiently hard on the cryostat to allow helium liquid into the sample space it was possible to get round this problem, but it was found very difficult to attain a stable temperature. Similarly, closing the helium valve on the flow cryostat system and pumping on the cryostat could lead to temperatures as low as 3K, but again temperature stability was difficult.

As was the case with the measurements in chapter 7, repeatability was found to be

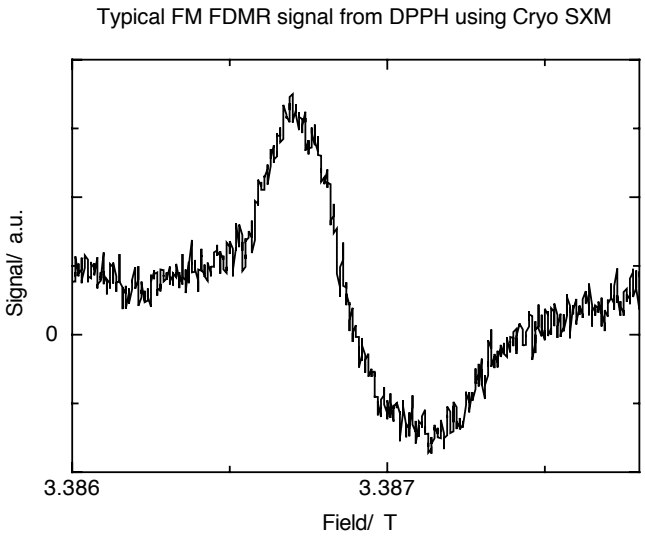

Figure 8.18: Frequency modulated FDMR spectrum of DPPH obtained with the Cryo SXM system.

difficult for both the $(FA)_2PF_6$ and the DPPH cases and the reasons discussed there apply equally here. The positioning of probe relative to sample in the $(FA)_2PF_6$ cases was done with the SXM outside the vacuum can and care had to be taken during insertion not to cause the piezo drives to slip due to knocks.

Chapter 9

Discussion and conclusions

The previous chapters in this thesis have discussed the theory and development of MRFM and have presented work done on the technique at high fields. This final chapter will be a discussion of the issues raised by the experiments, particularly the technical challenges posed and their resolution, and then the sensitivity of our measurements and likelihood of single spin detection are placed into the wider context of the achievements made by other groups as outlined in the review in chapter 1. It will then summarise the thesis and discuss the directions of future work.

9.1 Discussion

9.1.1 Technical challenges

As a technique, FDMR presents significant technical challenges, especially when conducted at high fields. This section will summarise the challenges encountered and discuss their impact and methods used for their solution, where this was possible. Some of these problems will be common to all FDMR/MRFM experiments and others result from the use of higher fields.

A significant problem arising from the higher fields used was that of delivering the millimetre waveB_1 field to the sample. The implementation of this is discussed in chapter 8 but although it was the best solution to the problem, was still not wholly satisfactory. At 10dB, the loss of the nickel silver waveguide is significant. Since we

want to be able to saturate our sample, we want the maximum available microwave power. Delivery of the B_1 field is important in all MRFM experiments, but far easier when one is able to use cables for the purpose. The polarisation properties of the non-corrugated circular waveguide are also very susceptible to distortions caused by any deformation of the waveguide, causing the polarisation to be smeared out. Damage to the guide may obviously be minimised by taking care, but we also developed miniature wire grid polarisers to use in future situations. The polarisation is important when trying to minimise spurious excitations of the cantilever by the RF. These will unfortunately also make angular alignment of the system relative to the input polarisation much more important than at present.

Another necessity for an FDMR experiment is the need to modulate the sample magnetisation. The spurious excitations that this produced, however, were significant, even in the frequency modulated case where there was a small amount of AM associated either with standing waves in the guide or the bias modulation of the Gunn diode. We did still manage, however, to obtain good signals despite this as shown in chapters 7 and 8, because as long as the level of the parasitic excitation is constant then it will be manifested as a constant baseline. However, a mechanism whereby the parasitic excitation may become dependent on the field and thus give rise to false signals is when if the sample is in resonance, its opacity changes sufficiently that the frequency modulation of the millimetre waves leads to a change in its transmission and thus creates an extra amplitude modulation of the microwaves at the cantilever. This larger amplitude modulation would thus stand out from the baseline level attributable to the spurious noise and give a false signal. While this signal is still obviously the direct result of magnetic resonance in the sample, it is not coupled to the cantilever via the magnetic interactions described in chapter 3 so the arguments used in those sections do not apply. Instead, the measurement would be analagous to RF power measurements where the RF heats a device the temperature of which is then measured. Thus, the cantilever would act as a calorimeter. Experiments exploiting this effect have been reported in which thin films of interest were deposited on AFM cantilevers and placed near a microstrip resonator at 9.17 GHz in an applied magnetic field [94]. At the FMR resonance condition, the absorption by the film peaks and the cantilever bends due to a bi-material effect. In the case of our experiments, the SiN cantilevers could exhibit a bimaterial effect due to the thin gold coating used to enhance reflection. The Si cantilevers, however, were uncoated. For amplitude modulated experiments, the change in microwave intensity during the cycle will be

smaller than total AM modulation, so the parasitic excitation level would not change. This parasitic excitation requires further investigation and is likely to be eliminated by the use of SiN cantilevers without a reflective gold layer.

9.1.2 Sensitivity

A major aim in this thesis has been the pursuit of high sensitivity, so it is appropriate to examine what experiment sensitivities we have managed to achieve. One important issue that has probably not received sufficient attention in the literature is the difference between the absolute sensitivity and the concentration sensitivity. The absolute sensitivity is a measure of the smallest magnetic moment that the experiment can detect. The concentration sensitivity on the other hand is a measure of the smallest spin density that may be detected. The distinction is an important one.

We may derive an expression for the necessary concentration sensitivity given the level of noise in the system. To simplify the situation, we assume that the cantilever thermal noise is dominant over the interferometer noise, which the discussion in section 3.4.3 shows is a reasonable assumption. We consider equation 3.40, from which we can see that the noise force in a bandwidth b will be

$$f_{\text{noise}} = \sqrt{\frac{4k_bTkb}{\omega_o Q}} \tag{9.1}$$

where k is the cantilever force constant, ω_0 its resonant frequency and Q its quality factor. In order to measure a force arising in our experiment, it will need to be larger than the above and this sets the limits to the detectable sensitivity. Consider the ideal situation where the sample geometry is such that the field gradient has more or less the same value over the whole sensitive slice of the sample (for example, the angle subtended by the sample with respect to the probe is small). We will look at the case for 100% amplitude modulation and assume that we are saturating the sample, so that the change in magnetisation, δM (see equation 3.3) is equal to M_0. Then the amplitude of the oscillating force generated by the modulation of the B_1 field will be equal to

$$f_{\text{sig}} = M_0 V_{\text{slice}} G_z \tag{9.2}$$

where V_{slice} is the volume of the resonant slice in the sample and G_Z is the field gradient in the z direction. For $s = 1/2$ particles, the magnetisation as a function of

field and temperature is given by equation 3.1. For small values of x, $\tanh x \approx x$ so for higher temperatures (above, say, 10K) we may say:

$$f_{\text{sig}} = \frac{V_{\text{slice}} G_z \mu_s^2 n B}{k_b T} \tag{9.3}$$

and at lower temperatures, the approximation is still reasonable. To obtain an expression for the minimum necessary spin concentration in the sample, n_{min}, to achieve unity signal to noise ratio, we simply set the expressions for f_{sig} and f_{noise} to be equal then solve for n:

$$n_{\text{min}} = \sqrt{\frac{4 k_b^3 T^3 k b}{\omega_0 Q V_{\text{slice}}^2 G_z^2 \mu_s^4 B^2}} \tag{9.4}$$

The minimum detectable number of spins is

$$N_{\text{min}} = \sqrt{\frac{4 k_b^3 T^3 k b}{\omega_0 Q G_z^2 \mu_s^4 B^2}} \tag{9.5}$$

and for a signal with a given signal to noise ratio, the number of spins contributing is

$$N_{\text{contrib}} = \sqrt{SNR} \sqrt{\frac{4 k_b^3 T^3 k b}{\omega_0 Q G_z^2 \mu_s^4 B^2}} \tag{9.6}$$

Note that these expressions both take account of the fact that only a small fraction of the spins are polarised (unless at very low temperature in very high field) whereas some authors report sensitivities in terms of the number of polarised spins. Although the above two equations only differ in that equation 9.4 includes a volume term and equation 9.5 does not, the difference is an important one as two experiments could have the same minimum detectable number of spins but different concentration sensitivities, or vice versa. In principle, the minimum detectable number of spins N_{min} may always be made smaller by increasing the field gradient (e.g. by reducing the probe particle size and bringing it closer to the sample). However, the resonant slice volume will reduce with increasing gradient so one could obtain an arbitrarily small N_{min} but then find that there are insufficient spins in the slice volume. Thus, the field gradient becomes more important for its effects on the imaging resolution than on sensitivity, and the concentration sensitivity is largely probe magnet independent. This is illustrated by considering a narrow cylindrical sample located directly above (or below) the probe magnet, such that the sensitive slice is simply a horizontal cross section of the sample with a finite thickness, Δz and area A_{slice}. Since the slice thick-

ness and sample linewidth are related (see section 3.1.4), the product $V_{\text{slice}}^2 G_z^2$ becomes $A_{\text{slice}}^2 \Delta B^2$ where ΔB is the line-width of the sample. Thus, there is no dependence on the field gradient for the force on the cantilever, but a large dependence on the line-width. Note that this simple argument suggests that a large ΔB is advantageous as it allows for a larger interaction volume. Since a larger linewidth is associated with a shorter τ_2 this would seem to run contrary to the idea that a longer τ_2 is preferable for experiments as mentioned in chapters 7 and 8. There is no contradiction, however, as the argument above assumes that the system has been saturated. The system would be harder to saturate with a short τ_2, but assuming that we could, then the larger line-width would lead to a larger signal.

9.1.3 Signal-to-noise ratios

Now that we have a way of relating the system signal-to-noise, we may see how measured SNRs compare to calculated values. For example, the AM spectrum shown in section 7.4 from the first experiment has a signal to noise ratio of 31dB, with an amplitude ratio of 34. Using a microscope with a graticule and taking the fibre diameter as a guide the magnetic particle size was estimated as 30μm and the separation from the surface of the sample as 80μm. Using the expression presented in section 3.1.6 for the gradient and with $\mu_0 M = 0.3$T for the ferrite, we arrive at a field gradient of 49Tm^{-1}. The volume of the interaction is obviously a non-trivial shape, but for an order of magnitude estimate we can consider the interacting portion of the sample to be a cylindrical slice with area such that it subtends a half angle of 39° (i.e. the angle out to the first zero of the gradient) and a thickness dependent on ΔB as mentioned above. ΔB is taken as 1×10^{-5}T. The resulting slice volume of 2.7×10^{-15}m^3 will contain the order of 2.2×10^{12} contributing electrons (assuming one electron per unit cell[95] of the sample and a unit cell of $6.6 \times 12.6 \times 14.8\mathring{A}$ [96] which yields a spin density of 8.1×10^{26}m^{-3}). At room temperature and 3.3T only about 0.7% of these will contribute to the magnetisation, resulting in a predicted signal to noise ratio of around $43dB$. Note that with the simplifications it assumes, this value is very approximate. It will also obviously be very sensitive to the probe magnet radius and separation from the sample, as it depends on the cube of the former and the fourth power of the latter. Thus although the SNR value measured from the noise in the spectrum in figure 7.12 (a) is $12dB$ below that just calculated, this order of error is very reasonable. This rough estimate assumes that we are saturating the

sample which even with our long τ_2 sample will not be the case with only a few mW of power. The effective large dependence on the line-width adds uncertainty as the spectrometer resolution is limited to about 5×10^{-6}T. Signal to noise ratios are much easier to estimate for the detection of point-like dipole moments, but this physical picture is even further removed from the real situation than the simple model above.

The signal to noise for the AM spectrum is typical of the AM measurements made. It should be noted that if the noise is strongly dominated by thermal noise (typically 20dB above the interferometer noise floor) then the interferometer sensitivity doesn't affect the SNR.

For our FM experiments it would be much harder to predict SNRs as the magnetisation, and hence the oscillating force, doesn't just have two possible values during the modulation cycle as is the case for the AM case (as discussed in section 4.2). The phase of the force signal would also differ for different parts of the sample. The advantage for the AM case is that one can fully modulate the magnetisation between its non-resonant value and zero without broadening the feature.

9.1.4 Towards single spin sensitivity?

One main goal that is often alluded to in the MRFM literature is that of sensitivity to a single spin, for both ESR and NMR based experiments. This section discusses the feasibility of achieving single electron spin sensitivity based on our current set-up (i.e. cantilevers, equipment etc). and also based on state-of-the-art MRFM.

The interaction volume estimated in section 9.1.3 suggests that the AM experiments were sensitive to the order of 6.4×10^{10} total spins in a 1Hz bandwidth or 4.4×10^{8} polarised spins. Thus, in order to be able to detect the moment of just a single polarised spin, we will require a sensitivity increase on the order of 5×10^{8} or 174dB! There are a number of ways in which we may improve the SNR. With a better vacuum and a smaller magnetic tip, then a cantilever Q of 10,000 at 10kHz is not unrealistic, which would give a 27dB times increase in SNR. Reducing the temperature to 4K offers a 46dB increase in SNR, although since our argument presumes that the noise is dominated by cantilever thermal noise this is an upper bound. Tripling the mm-wave frequency to 280 GHz (the highest operating frequency of the spectrometer) offers 10dB and the waveguide will be less lossy at higher frequencies. A reduction in

tip magnet radius from 30μm to, say, 1μm and a scanning distance of 330nm would increase SNR (for a point dipole sample) by 77dB. These changes would give us a total SNR improvement of 160dB and sensitivity to a point magnetic moment of about 22 spins. Single-spin level sensitivity is not a practical goal using our present 0.2Nm^{-1} or 0.02Nm^{-1} cantilevers. It should be stressed that this level of improvement is felt to be realisable with work on our current system but will require considerable experimental finesse, particularly regarding the relative positioning of probe and sample. Signals from 100 net polarised spins have been announced by Stipe and co-workers[29].

More sensitivity could be obtained by moving to much softer cantilevers: devices have been announced with force constants the order of 10^{-5}Nm^{-1} [97] but this type of device is not yet commercially available. The highest sensitivity force measurements [98] used a stiffer cantilever (2.6×10^{-4}Nm^{-1}) and by cooling to 110mK achieved a force sensitivity of 8.2×10^{-19}NHz$^{-1/2}$ but the cooling adds a new level of complexity to the experiment. Such a force sensitivity, however, would be sufficient to detect a point-like single electron spin with a 1μm radius iron probe particle at a distance of 330nm with a signal-to-noise ratio of 23dB in a 1Hz bandwidth. The gradient size and separation of the sample and probe are easily realisable at the moment. Thus, for an optimised experiment, single electron spin detection is possible at the moment and it is only a matter of time until a measurement sensitivity equal to an electron magnetic moment is announced. The issue of measuring an individual electron spin (as opposed to an equivalent level of sensitivity to magnetic moments) is, of course, more complex than this as at the level of individual electrons, the concept of classical bulk magnetisation which has been used in this thesis breaks down and a quantum mechanical treatment would be required.

9.2 Summary and conclusions

This thesis set out to extend the new technique of magnetic resonance force microscopy to high magnetic fields, driven by the pursuit of greater sensitivity and superior spectral resolution. It began with a review of MRFM and FDMR work to date summarising the different approaches used by various groups in ESR, NMR and FMR based experiments. This was followed by an introduction to conventional ESR spectroscopy which discussed sample magnetisation and relaxation using the Bloch equations, before outlining instrumental issues and the motivation for carrying out

ESR at higher fields (3T and above).

Chapter 3 presented the ideas and theory behind force detected magnetic resonance, looking in turn at the magnetic interaction between the sample and the probe, micro-scale scanning probe microscopy cantilevers and their use in experiments of this type, including the methods of detection, and the main noise mechanisms, of which thermal noise dominates. The following chapter illustrated some of the ideas using a simple computer model to look at expected signals and to show the concepts of the sensitive resonant slice within a sample and the resulting point spread function of the probe arrangement for future imaging experiments. This allowed for the explanation of some less intuitive aspects of the FDMR spectra.

The extensive instrumental work on signal detection using fibre optic interferometry and cantilevers was described in chapters 5 and 6 respectively. The optics chapter described our choice of source and interferometer configuration as well as later improvements to sensitivity and tuneability that will benefit future measurements. Chapter 6 focused on the use of cantilevers and the determination of their Q factors, as well as the mounting of magnetic particles and samples on to cantilevers.

Chapter 7 built on the above covering our first FDMR experiments measuring $(FA)_2PF_6$ with a preliminary set-up, describing the design and execution of the experiment in some detail followed by the presentation of representative spectra and their signal-to-noise ratios. Chapter 8 gave an account of the commercial SPM system that was to be used as a basis for our high field MRFM and the design and implementation of the additions made to it, particularly those required for the illumination with millimetre wave radiation. Signals seen with both $(FA)_2PF_6$ and DPPH are presented.

Finally, the first part of this chapter summarises the significant technical issues encountered in this project and discusses the sensitivity of our measurements. This thesis shows that MRFM is a promising technique but its exploitation will require significant further investment in effort. Single electron spin sensitivity is a real and achievable goal (if out of the reach of our own experiments) but the experimental difficulties involved in such experiments should not be understated [57].

9.3 Future work

A project such as this raises as many issues as it examines, so there is obviously huge scope for future developments, as well as some suggestions on a better approach to the problem than has been taken. These are provided in this section. Some are ideas that may be applied immediately and others would be advantageous to the long term pursuit of the technique.

A priority is the further development of the Q reduction via feedback shown in chapter 8, namely calibration to assess the forces that may be exerted on a cantilever and its use in an FDMR experiment. A related avenue for development is the introduction of a phase locked loop (PLL) into the system. A small drive would be applied via the coil and the PLL would adjust the drive frequency to keep the cantilever on resonance. This will allow the more accurate tracking of the cantilever resonant frequency, changes in which can also be used as the signal [99], rather than just the amplitude. Similar systems have been used by other groups [87].

One aspect that has been briefly mentioned in the discussion of modelling (see chapter 4) is that of discriminating between two or more species that may be present in a sample and this is an area that needs experimental work. More work has been done concerning the possible spatial resolution of MRFM systems than the spectral resolution, but for applications where chemical discrimination is important then this will be critical. Obviously the system will only be able to resolve two different species if their lines are still distinct after broadening by the presence of the probe particle, as illustrated by the two species model spectra in chapter 4. Many experiments have illustrated the distinction between two or more spatially distinct samples, but fewer have looked at spectrally distinct samples, a notable exception being in [33]. An experiment well worth doing would be FDMR on an extended sample containing a mix of two different species.

The ultimate goal for our instrument is the acquisition of force maps and images of spin density. This is going to require a solution to some technical problems such as possible interference of the flexible mm-waveguide with the coarse scanning capability of the CryoSXM. A method of determining proximity of the probe to a sample would also greatly aid experiments. A possible and practical solution would be the insertion of another fibre interferometer into the SXM head and the use of fringe counting for distance measurement. It would also be fruitful to examine how similar technical

issues are resolved in commercial AFM systems to avoid great expenditure of effort on problems that have already been solved elsewhere.

An important part of attempting MRFM imaging will be the examination of how to recover information regarding the spatial distribution of the spins in a sample from the force map obtained in the imaging experiment. Data may be obtained in effectively four dimensions: the three cartesian coordinates plus the magnetic field. This is expected to be a non-trivial task, but methods of de-convolution are widely known and implementable using Fourier transforms.

An interesting proposal has been made by Leskowitz et. al. [100] of FDMR *without imposing a field gradient*. This would be accomplished by having the sample of interest positioned between two discs of magnetised material. The central portion of one of these discs would be physically separate from the surrounding material and supported by some sort of flexible membrane allowing it to move. This distinct element would thus be able to move when acted on by the changing field due to the modulated magnetisation of the sample. Since the movable part of the magnet would be the same size as the portion of the magnet it displaces, the field would look the same as if both discs were uniform and intact, so the sample would see no field gradient, allowing all the spins in the sample to be measured rather than just a sensitive slice. This would require a different approach to imaging but would be a method of extending sensitivity for spectroscopy applications as the linewidths would not be broadened by a gradient. Imaging would still be possible because even without a field gradient, the strength of the interaction between sensor and sample will depend on their relative positions, so deconvolution could yield a spin density image. This would represent a slight change of direction from the path pursued in this thesis, but the two ideas would complement each other. The practicalities of delivering the mm-waves to the sample in such an arrangement would present a challenge, but could yield significant improvements in sensitivity.

Appendix A

Program listing for model

This appendix shows the C program used to produce the model spectra and force maps shown in chapter 4. The different situations were all modelled with slightly different programs. These programs, however, were all based on the same set of functions, so only one program is shown here as an example. This is"round.c", the program used to model the AM case for a cylindrical sample. The programming style is not particularly elegant: variable parameters (such as probe moment, etc.) were hardwired in and the program recompiled when changes were required. The simple flow chart in figure A.1 shows the program structure. The program structure

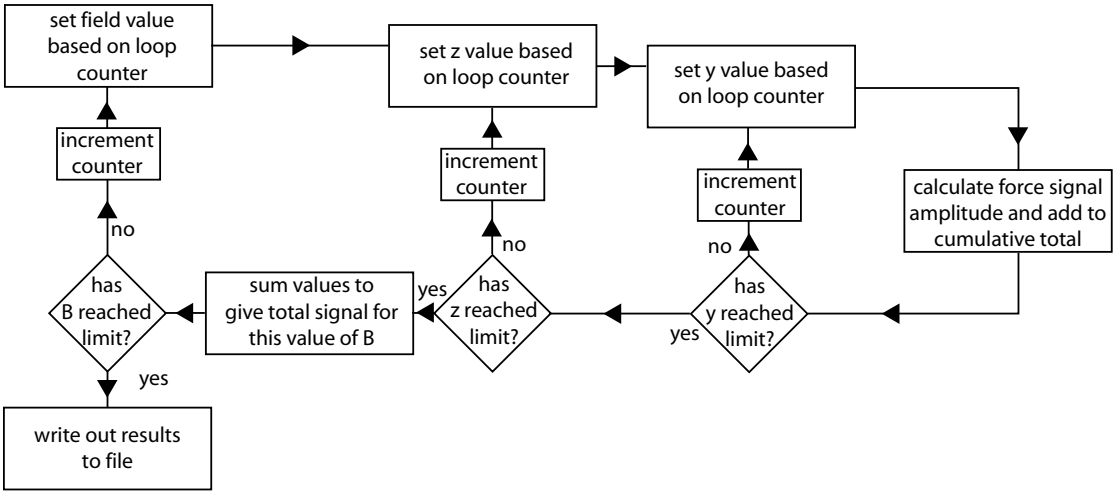

Figure A.1: Flow chart for modelling program "round.c" showing the basic program structure.

was similar for all the programs. The biggest difference was for the programs that produced a model spectrum, the contributions from different regions of the sample were summed for a total signal, whereas to obtain a force map, the contribution from each volume element was stored in a 2D matrix.

The programs begins by initialising the variables and obtaining a filename. It then writes a log file recording the values used for various parameters. The external field parameter is set to its starting value then the value of the sample volume element z position is set. For this value of z, the y position is incremented and at each position, the force signal amplitude is calculated, working in a radial line from the centre of the sample. Once the line of amplitude values have been calculated, the contribution due to the whole surface at that z position is calculated. The z position is then incremented and repeated until the desired maximum value. The signals from the different z value slices are then summed to give the total signal amplitude at that field value. The field parameter is then incremented and so on. After the desired number of field values (400 in the case below, but variable) the result is written to a file. The listing for "round.c" may be seen below.

```
/*
round.c
Paul A. S. Cruickshank, 08/06/03

Include header files
*/
#include <stdio.h>
#include <math.h>
#include <string.h>
#include <stdlib.h>
#include <time.h>

/*
Define some useful constants
*/
#define ElectronMass 9.1093897E-31
#define ElectronCharge 1.60217733E-19
#define HBar 1.055197273E-34
#define BohrMagneton 9.2663E-24
#define BoltzmannConstant 1.380658E-23
#define Pi 3.141592654
#define MuNought 1.25664E-6
```

```
/*
Declare function prototypes
This function calculates the magnetisation of a sample volume element
*/
double InitialMagnetisation(double , double, double, double);

/*
This function calculates magnetisation with an RF field
*/
double FinalMagnetisation(double, double, double, double,
double, double, double);

/*
This function calculates gamma based on g
*/
double GyroMagneticRatio(double);

/*
This function calculates the resonant field from the g factor and mmwave
frequency
*/
double ResonantField(double, double);

/*
This function calculates z field due to probe magnet
*/
double ProbeFieldInZDirection(double *ProbeCoordinate, double
*SampleCoordinate, double ProbeMoment);

/*
Calculates z field gradient due to probe magnet
*/
double ProbeGradientInZDirection(double *ProbeCoordinate, double
*SampleCoordinate, double ProbeMoment);

int main (void)
{
    /* Declare variable for use within main */

    char date[255]={0};
    time_t now;
    struct tm *timer;
```

```
char FileName[20];
char FilePath[40];
char LogFilePath[40];

int NumberOfLayers=10;
int Loopz;
int Loop0;
int Loop1;
int Loop2;
int Loop3;

double SliceSignal;
double ExternalField;
double RFFrequency = 9E10;
double RFField = 1E-6;
double Tau1 = 5e-6;
double Tau2 = 5e-6;
double GyroMagRatio;
double GFactor = 2.0023;
double Temperature = 300;
double TotalField;
double InitialMag;
double FinalMag1;
double YIncrement = 2E-8;
double ZIncrement = 2E-8;
double FieldInc = 0.00001;
double StartingZ =60E-6;
double ProbeMoment=1E-9;
double SamplePosition[3];
double ProbePosition[3];
double ResField;
double totalforce=0;
double ForceArray[20000];
double ResultArray[700][2];
double SliceArray[20000];
double spinspervol=1e24;
int Radius=2000;

FILE *FilePointer;
FILE *LogFilePointer;

ProbePosition[0] = 0;
ProbePosition[1] = 0;
```

```
ProbePosition[2] = 0;

/*
Obtain filename and set filepath
*/
printf("\nInput filename ");
scanf("%s", FileName);
sprintf(FilePath, "Results/");
strcat(FilePath, FileName);
strcpy(LogFilePath, FilePath);
strcat(LogFilePath, "logfile.txt\0");

/*
Obtain time and write it to a string
*/
now=time(NULL);
timer=localtime(&now);
strftime(date, 64, "%d/%m/%y  %H:%M:%S", timer);
printf("\nStarted at %s\n", date);

/*
Calculate gyromagnetic ratio
*/
GyroMagRatio = GyroMagneticRatio(GFactor);

/*
Calculate resonant field
*/
ResField = ResonantField(GyroMagRatio, RFFrequency);

/*
Open log file and write the constants to it
*/
LogFilePointer=fopen(LogFilePath, "w");
fprintf(LogFilePointer, "round.c\n%s\n", date);
fprintf(LogFilePointer, "Hello!!!!\n");
fprintf(LogFilePointer, "tau1 = %e us\ntau2 = %e us\nStarting z = %e m\nz increment =
%e m\n", Tau1, Tau2, StartingZ, ZIncrement);
fprintf(LogFilePointer, "y increment = %e m\nRF frequency = %e Hz\nRF field =
%e T\n", YIncrement, RFFrequency, RFField);
fprintf(LogFilePointer, "temperature = %lf K\ng factor = %lf\nresonant field =
%lf T\nfield increment = %lf T\nspins per unit volume = %e\n", Temperature,
GFactor, ResField, FieldInc, spinspervol);
```

```
fprintf(LogFilePointer, "probe moment = %e\n", ProbeMoment);
fprintf(LogFilePointer, "number of layers of spins = %d\n", NumberOfLayers);
fprintf(LogFilePointer, "Radius= %d points\n", Radius);
fclose(LogFilePointer);

/*
Commence loops. Loop0 increments the magnetic field
*/
for (Loop0=0; Loop0<=399; Loop0++)
{
    totalforce=0;
    /*
    Set the starting value of the polarising field
    */
    ExternalField=ResField - (200*FieldInc) + (Loop0*FieldInc);
    /*
    Loopz increments the z position
    */
    for (Loopz=0; Loopz<(NumberOfLayers); Loopz++)
    {
        SamplePosition[2]=StartingZ+(Loopz*ZIncrement);
            /*
            Loop2 increments the y position
            */
            for (Loop2=0; Loop2<Radius; Loop2++)
            {
                SamplePosition[1]=(Loop2)*YIncrement;
                /*
                Calculate the total field at the position of interest
                */
                TotalField = ExternalField+ProbeFieldInZDirection(ProbePosition,
                 SamplePosition, ProbeMoment);
                /*
                Calculate the initial sample magnetisation at the given position
                based on the field calculated above
                */
                InitialMag = InitialMagnetisation(spinspervol, TotalField, GFactor,
                Temperature);
                /*
                Calculate the final magnetisation
                */
                FinalMag1 = FinalMagnetisation(GyroMagRatio, RFField, Tau1, Tau2,
                 TotalField, RFFrequency, InitialMag);
```

```
                    /*
                    Calculate the force difference
                    */
                    SliceArray[Loop2]=((FinalMag1-InitialMag)*
                    ProbeGradientInZDirection(ProbePosition, SamplePosition, ProbeMoment));
                /*
                About to close Loop2
                */
                }
            for(Loop1=0; Loop1<=Radius-1;Loop1++)
            {
                ForceArray[Loop1]=YIncrement*Loop1*Pi*2*YIncrement*ZIncrement
                *SliceArray[Loop1];
                totalforce=totalforce+ForceArray[Loop1];
            }

        /*
        About to close Loopz
        */
        }
        ResultArray[Loop0][0]=ExternalField;
        ResultArray[Loop0][1]=totalforce;

        printf("%d\n", Loop0);

        /*
        About to close Loop0
        */
    }

    FilePointer=fopen(FilePath, "w");
    for (Loop3=0; Loop3<=399; Loop3++)
    {
        fprintf(FilePointer, "%e\t%e\n", ResultArray[Loop3][0], ResultArray[Loop3][1]);
    }
    fclose(FilePointer);
    printf("\nDone!\n");
    now=time(NULL);
    timer=localtime(&now);
    strftime(date, 64, "%d/%m/%y  %H:%M:%S", timer);
    printf("\nFinished at %s\n", date);
/*
End of function main
```

```
*/
}
/*
This function calculates the magnetisation of a sample with no RF field present.
The function depends on the spin density, gfactor, field and temperature.
*/
double InitialMagnetisation(double SpinsPerUnitVolume, double AppliedField,
 double GFactor, double Temperature)
{
    double SingleSpin;
    double InitialMag;


    SingleSpin = (BohrMagneton*GFactor)/2;
    InitialMag = SingleSpin*SpinsPerUnitVolume*(tanh((SingleSpin*AppliedField)/
    (BoltzmannConstant*Temperature)));

    return(InitialMag);
}

/*
This function calculates the magnetisation with an RF field present.
It uses the result of the above function, as well as the relaxation times,
gamma, and the applied static and RF fields.
*/
double FinalMagnetisation(double GyroMagRatio, double RFField,
 double Tau1, double Tau2, double AppliedField, double RFFrequency, double InitialMag)
{
    double TopLine;
    double BottomLine;
    double FinalMag;

    FinalMag = InitialMag* (1-((pow(GyroMagRatio,2)*pow(RFField,2)
    *Tau1*Tau2)/(1+(((GyroMagRatio*AppliedField)-(RFFrequency*2*Pi))
    *((GyroMagRatio*AppliedField)-(RFFrequency*2*Pi))*pow(Tau2,2))
    +(pow(GyroMagRatio,2)*pow(RFField,2)*Tau1*Tau2))));
    return(FinalMag);
}

/*
This function calculates gamma, based on the supplied gfactor.
*/
double GyroMagneticRatio(double GFactor)
```

```
{
    return((GFactor*BohrMagneton)/HBar);
}

/*
This function calculates the resonant field based on the RF frequency and gamma.
*/
double ResonantField(double GyroMagRatio, double RFFrequency)
{
    return((2*Pi*RFFrequency)/GyroMagRatio);
}

/*
This function calculates the field due to the probe.
*/
double ProbeFieldInZDirection(double *ProbeCoordinate, double
 *SampleCoordinate, double ProbeMoment)
{
    double delta_x;
    double delta_y;
    double delta_z;
    double r;

    delta_x = SampleCoordinate[0]-ProbeCoordinate[0];
    delta_y = SampleCoordinate[1]-ProbeCoordinate[1];
    delta_z = SampleCoordinate[2]-ProbeCoordinate[2];


    r = sqrt(pow(delta_x,2)+pow(delta_y,2)+pow(delta_z,2));
    return((2*pow(delta_z,2) - pow(delta_x,2) - pow(delta_y,2))*
    ((MuNought/(4*Pi))*ProbeMoment)/pow(r,5));
}

/*
This calculates the field gradient due to the probe.
*/
double ProbeGradientInZDirection(double *ProbeCoordinate,
 double *SampleCoordinate, double ProbeMoment)
{
    double delta_x;
    double delta_y;
    double delta_z;
```

```
    double r;
    double result;
    delta_x = SampleCoordinate[0]-ProbeCoordinate[0];
    delta_y = SampleCoordinate[1]-ProbeCoordinate[1];
    delta_z = SampleCoordinate[2]-ProbeCoordinate[2];

    r = sqrt(pow(delta_x,2)+pow(delta_y,2)+pow(delta_z,2));
    return(((9*delta_z)-((15*pow(delta_z,3))/pow(r,2)))*
    ((MuNought/(4*Pi))*ProbeMoment)/pow(r,5));
}
```

Bibliography

[1] J. A. Sidles, Applied Physics Letters **58**, 2854 (1991).

[2] J. A. Sidles, J. L. Garbini, and G. P. Drobny, Review of Scientific Instruments **63**, 3881 (1992).

[3] J. A. Sidles, Physical Review Letters **68**, 1124 (1992).

[4] J. A. Sidles and D. Rugar, Physical Review Letters **70**, 3506 (1993).

[5] D. Rugar, C. S. Yannoni, and J. A. Sidles, Nature **360**, 563 (1992).

[6] D. Rugar et al., Science **264**, 1560 (1994).

[7] Z. Zhang, P. C. Hammel, and P. E. Wigen, Applied Physics Letters **68**, 2005 (1996).

[8] Z. Zhang and P. C. Hammel, IEEE Transactions on Magnetics **33**, 4047 (1997).

[9] Z. Zhang and P. C. Hammel, Solid State Nuclear Magnetic Resonance **11**, 65 (1998).

[10] K. Wago, D. Botkin, C. S. Yannoni, and D. Rugar, Applied Physics Letters **72**, 2757 (1998).

[11] O. Zuger and D. Rugar, Applied Physics Letters **63**, 2496 (1993).

[12] O. Zuger and D. Rugar, Journal of Applied Physics **75**, 6211 (1994).

[13] P. C. Hammel, Z. Zhang, G. J. Moore, and M. L. Roukes, Journal of Low Temperature Physics **101**, 59 (1995).

[14] O. Zuger, S. T. Hoen, C. S. Yannoni, and D. Rugar, Journal of Applied Physics **79**, 1881 (1996).

[15] S. il Park and R. C. Barrett, *Design considerations for an STM system*, pages 31–76, Academic Press, 1993.

[16] G. Binnig and D. P. E. Smith, rsi **57**, 1688 (1986).

[17] W. M. Dougherty et al., Journal of Magnetic Resonance **143**, 106 (2000).

[18] K. Wago et al., Review of Scientific Instruments **68**, 1823 (1997).

[19] K. J. Bruland, J. Krzystek, J. L. Garbini, and J. A. Sidles, Review of Scientific Instruments **66**, 2853 (1995).

[20] W. M. Dougherty, K. J. Bruland, J. L. Garbini, and J. A. Sidles, Measurement Science and Technology **7**, 1733 (1996).

[21] J. A. Marohn, R. Fainchtein, and D. D. Smith, Journal of Applied Physics **86**, 4619 (1999).

[22] D. D. Smith, J. A. Marohn, and L. E. Harrell, Review of Scientific Instruments **72**, 2080 (2001).

[23] G. Alzetta et al., Journal of Magnetic Resonance **141**, 148 (1999).

[24] R. Verhagen et al., Physical Chemistry Chemical Physics **1**, 4025 (1999).

[25] G. P. Berman, G. D. Doolen, P. C. Hammel, and V. I. Tsifrinovich, Physical Review B **61**, 14694 (2000).

[26] G. P. Berman, G. D. Doolen, P. C. Hammel, and V. I. Tsifrinovich, Physical Review Letters **86**, 2894 (2001).

[27] G. P. Berman and V. I. Tsifrinovich, Physical Review B **61**, 3524 (2000).

[28] T. D. Ladd et al., Physical Review Letters **89** (2002), Article no. 017901.

[29] B. C. Stipe et al., Physical Review Letters **87** (2001), Article no. 277602.

[30] J. G. Kempf and J. A. Marohn, Physical Review Letters **90** (2003), Article no. 087601.

[31] H. J. Mamin, R. Budakian, and D. Rugar, Review of Scientific Instruments **74**, 2749 (2003).

[32] K. R. Thurber, L. E. Harrell, and D. D. Smith, Journal of Applied Physics **93**, 4297 (2003).

[33] K. R. Thurber, L. E. Harrell, and D. D. Smith, Journal of Magnetic Resonance **162**, 336 (2003).

[34] Y. Manassen, R. J. Hamers, J. E. Demuth, and J. A. J. Castellano, Physical Review Letters **62**, 2531 (1989).

[35] Y. Manassen, I. Mukhopadhyay, and N. R. Rao, Physical Review B **61**, 16223 (2000).

[36] C. Durkan and M. E. Welland, Applied Physics Letters **80**, 458 (2002).

[37] L. N. Bulaevskii and G. Oritz, Physical Review Letters **90** (2003), Article no. 040401.

[38] C. P. Poole, *Electron Spin Resonance. A Comprehensive Treatise on Experimental Techniques*, Dover, second edition, 1996.

[39] A. Sweiger and G. Jesche, *Principles Of Pulse Electron Paramagnetic Resonance*, Oxford University Press, New York, 2001.

[40] A. P. Guimaraes and I. S. Oliveira, *Introduction to Magnetism and Magnetic Resonance in Solids*, Wiley, New York, 1998.

[41] K. A. McLauchlan, *Magnetic Resonance*, Oxford, London, 1972.

[42] J. A. Weil, J. R. Bolton, and J. E. Wertz, *Electron Paramagnetic Resonance: Elementary Theory and Practical Applications*, John Wiley and Sons, New York, 1994.

[43] N. M. Atherton, *Principles of Electron Spin Resonance*, Ellis Horwood, London, 1993.

[44] C. N. Banwell and E. M. Cash, *Fundamentals of Molecular Spectroscopy*, McGraw Hill, fourth edition, 1994.

[45] J. W. Orton, *Electron Paramagnetic Resonance*, Iliffe, 1968.

[46] B. Bleany and K. W. H. Stevens, Reports on Progress in Physics **16**, 108 (1953).

[47] G. M. Smith and P. C. Riedi, Electron Paramagnetic Resonance **17**, 164 (2000).

[48] Y. S. Lebedev, Electron Spin Resonance **14**, 63 (1994).

[49] J. C. G. Lesurf, *Millimetre-wave Optics, Devices and Systems*, Adam Hilger, Bristol, 1990.

[50] W. B. Lynch, K. A. Earle, and J. H. Freed, Review of Scientific Instruments **59**, 1345 (1988).

[51] G. M. Smith, J. C. G. Lesurf, R. H. Mitchell, and P. C. Riedi, Review of Scientific Instruments **69**, 3924 (1998).

[52] M. R. Fuchs, T. F. Prisner, and K. Mobius, Review of Scientific Instruments **70**, 3681 (1999).

[53] R. Bowley and M. Sanchez, *Introductory Statistical Mechanics*, Oxford, 1996.

[54] P. Lorrain and D. Corson, *Electromagnetic Fields and Waves*, W. H. Freeman and Co., San Fransisco, 1969.

[55] Z.-P. Liang and P. C. Lauterbur, *Principles of Magnetic Resonance Imaging a Signal Processing Perspective*, IEEE Press, New York, 2000.

[56] Nanosensors GmbH and Co KG, Wetzlar-Blankenfeld, Germany, *Nanosensors Product Guide*, 2000.

[57] J. A. Sidles et al., Reviews of Modern Physics **67**, 249 (1995).

[58] P. M. Morse, *Vibration and Sound*, McGraw Hill, New York, 1936, page 119.

[59] M. J. Tudor, M. V. Andres, K. W. H. Foulds, and J. M. Naden, IEE Proceedings D **135**, 364 (1988).

[60] G. Stemme, Journal of Micromechanics and Microengineering **1**, 113 (1991).

[61] F. R. Blom, S. Bouwstra, M. Elwenspoek, and J. H. J. Fluitman, Journal of Vacuum Science and Technology B **10**, 19 (1992).

[62] H. Hosaka, K. Itao, and S. Kuroda, Sensors and Actuators A **49**, 87 (1995).

[63] G. Binnig, C. F. Quate, and C. Gerber, Physical Review Letters **56**, 930 (1986).

[64] Y. Martin, C. C. Williams, and H. K. Wickramasinghe, Journal of Applied Physics **61**, 4723 (1987).

[65] Y. Martin and H. K. Wickramasinghe, Applied Physics Letters **50**, 1455 (1987).

[66] D. Rugar, H. J. Mamin, R. Erlandsson, J. E. Stern, and B. D. Terris, Review of Scientific Instruments **59**, 2337 (1988).

[67] A. D. Drake and D. C. Leiner, Review of Scientific Instruments **55**, 162 (1984).

[68] D. Rugar, H. J. Mamin, and P. Guenther, Applied Physics Letters **50**, 2588 (1989).

[69] F. L. Pedrotti and L. S. Pedrotti, *Introduction to optics*, Prentice Hall, second edition, 1993.

[70] P. Hariharan, *Basics of Interferometry*, Academic Press, San Diego, 1992.

[71] P. Hariharan, Reports on Progress in Physics **54**, 339 (1990).

[72] T. B. Gabrielson, IEEE Transactions on Electron Devices **40**, 903 (1993).

[73] D. P. E. Smith, Review of Scientific Instruments **66**, 3191 (1995).

[74] W. A. Edelstein, J. Hough, J. R. Pugh, and W. Martin, Journal of Physics E: Scientific Instruments **11**, 710 (1978).

[75] W. H. Press, S. A. Teukolsky, W. T. Vetterling, and B. P. Flannery, *Numerical Recipes in C*, Cambridge University Press, second edition, 1992.

[76] K. J. Bruland et al., Review of Scientific Instruments **70**, 3542 (1999).

[77] J. E. Sader, I. Larson, P. Mulvaney, and L. R. White, Review of Scientific Instruments **66**, 3789 (1995).

[78] N. Elejalde-Ochandiano, *Design and development of a microfabricated sensor for biochemical detection*, PhD thesis, University of St Andrews, 2002.

[79] J. P. Cleveland, S. Manne, D. Bocek, and P. K. Hansma, Review of Scientific Instruments **64**, 403 (1993).

[80] B. J. Suh et al., Journal of Vacuum Science and Technology B **16**, 2275 (1998).

[81] G. M. Smith, *Transferred electron oscillators at mm wave frequencies and their characterisation using optical techniques*, PhD thesis, University of St Andrews, 1990.

[82] W. S. Cheung and F. H. Levien, *Microwaves Made Simple*, Artech House, 1985.

[83] D. R. Bolton, Progress in the design and realisation of circuits and cavities for 94GHz and 188GHz EPR spectroscopy, First year PhD report, University of St Andrews, 2003.

[84] P. F. Goldsmith, *Quasioptical Systems*, IEEE Press, New York, 1998.

[85] M. R. Webb, *Millimetre wave quasi-optical signal processing systems*, PhD thesis, University of St Andrews, 1992.

[86] D. Craik, *Magnetism. Principles and Applications*, Wiley, 1995.

[87] J. A. Marohn, R. Fainchtein, and D. D. Smith, Applied Physics Letters **73**, 3778 (1998).

[88] C. W. Miller, U. M. M. andTroy C. Messina, and Y. J. Lee, Journal of Applied Physics **93**, 6572 (2003).

[89] R. E. Collin, *Foundations For Microwave Engineering*, McGraw–Hill, 1992.

[90] J. Mertz, O. Marti, and J. Mlynek, Applied Physics Letters **62**, 2344 (1993).

[91] K. J. Bruland, J. L. Garbini, W. M. dougherty, and J. A. Sidles, Journal of Applied Physics **83**, 3972 (1998).

[92] J. L. Garbini, K. J. Bruland, W. M. Dougherty, and J. A. Sidles, Journal of Applied Physics **80**, 1951 (1996).

[93] K. J. Bruland, J. L. Garbini, W. M. Dougherty, and J. A. Sidles, Journal of Applied Physics **80**, 1959 (1996).

[94] J. Moreland, M. Lohndorf, P. Kabos, and R. D. McMichael, Review of Scientific Instruments **71**, 3099 (2000).

[95] G. Sachs, E. Dormann, and M. Schwoerer, Solid State Communications **53**, 73 (1985).

[96] V. Enkelmann, B. S. Morra, C. Krohnke, G. Wegner, and J. Heinze, Chemical Physics **66**, 303 (1982).

[97] T. D. Stowe et al., Applied Physics Letters **71**, 288 (1997).

[98] H. J. Mamin and D. Rugar, Applied Physics Letters **79**, 3358 (2001).

[99] T. R. Albrecht, P. Grutter, D. Horne, and D. Rugar, Journal of Applied Physics **69**, 668 (1991).

[100] G. M. Leskowitz, L. A. Madsen, and D. P. Weitekamp, Solid State Nuclear Magnetic Resonance **11**, 73 (1998).